



INTEGRATED MASTER IN ENVIRONMENTAL ENGINEERING 2017/2018

**SYNTHESIS OF THREE-DIMENSIONAL HEMATITE
PHOTOELECTRODES FOR PHOTOELECTROCHEMICAL CELLS**

FILIFE MOISÉS DA MOTA FRANCISCO

Dissertation submitted for the degree of

MASTER ON ENVIRONMENTAL ENGINEERING

President of the jury:

Cidália Maria de Sousa Botelho
Assistant Professor in the Chemical Engineering Department at FEUP

Supervisors at the University:

João Carlos Almeida Monteiro Azevedo
Postdoctoral researcher in the Chemical Engineering Department at FEUP

Paula Manuela Monteiro Pereira Costa Dias
Postdoctoral researcher in the Chemical Engineering Department at FEUP

Adélio Miguel Magalhães Mendes
Full Professor in the Chemical Engineering Department at FEUP

July 2018

To my grandparents...

“São os espíritos superficiais que mais crêem nos êxitos retumbantes, nas fórmulas fáceis para vencer, pois isso lhes lisonjeia a incapacidade e a fraqueza de vontade. Os lances engenhosos, em que se torce a moral para obter um mais rápido efeito, conseguem grande público. Mas a vida, cujas leis são infinitamente mais sóbrias, mais puras que as dos homens, não as aceita.”

Agustina Bessa-Luís, *in* A Sibila

Acknowledgment

This work was partially supported by the Project "SunStorage - Harvesting and storage of solar energy", funded by European Regional Development Fund (ERDF), through COMPETE 2020 - Operational Programme for Competitiveness and Internationalization (OPCI), and by national funds, through FCT - Portuguese Foundation for Science and Technology I.P.; and by the Projects POCI-01-0145-FEDER-006939 - Laboratory for Process Engineering, Environment, Biotechnology and Energy - LEPABE and NORTE-01-0145-FEDER-000005 - LEPABE-2-ECO-INNOVATION, funded by FEDER funds through COMPETE2020 - OPCI and Operational Programme for North Region (NORTE2020) and by national funds through FCT.

The arrival at this stage of my academic journey has, in addition to me, many protagonists who have assumed a crucial role in my personal growth and in the knowledge that I have acquired. None of my achievements would have been possible alone. And that's why I want to leave a few words of appreciation here.

I begin by thanking my parents because, without them and without the bet they made on me every day during these years, it would not be possible to arrive at the end of this journey. The sum of my successes is for them a dream came true and one that I intend to keep providing them.

I am also grateful to Professor Adélio Mendes, my co-supervisor, for giving me the opportunity to develop the dissertation in his laboratory. It was an honor for me to have him as a Professor and to have known up close the quality of the scientific work he carries out in the service of society and the citizens. Thank you, Professor, also for the nice way you received me at the times we met and for the constructive and intelligent way you encouraged me to improve my work even more.

I would also like to thank Dr. João Azevedo and Dr. Paula Dias, my supervisors, two very special people for me in this working group. It is indescribable the excellent quality of the orientation that I had and the accompaniment that they gave me. At no point did I feel helpless or unsure what to do because both were always able to hear me and discuss with me the solutions to follow to get around the problems that were emerging. I would like to emphasize their patience, friendship and cooperation capacity in all the work they carry out as meritorious qualities and which will surely bring them the successes they deserve.

Thank you also to all members of the Solar Group for all the friendliness and the good environment with which they work. Despite my shyness, they have always welcomed me and have always been helpful to me. I would like to highlight in this acknowledgment the teachings and the readiness of Fátima Santos, which helped me in the preparation of the SiO₂

films, the wise advice and the availability of the Dmitri Ivanov and Jeffrey Capitão that were crucial to get around the problems that have arisen throughout the work, to Isabel Mesquita for teaching me how to use the spin coater, to Cecília Mateos by the helpful way which she taught me the basic principles of BET and to Tiago Lagarteira with whom I have often had to share the use of equipment and who have always been ready to cooperate in this regard.

No less important is the acknowledgment to all those I have met over the last 5 years. In it I highlight Professor Fernando Pereira, my course director, and Professor Cidália Botelho, with whom I actively worked on the Monitoring Committee of the Integrated Master in Environmental Engineering, both as my year's representative and as an elected member. The availability, sympathy and openness to the dialogue of both are something that I will remember as important in this institutional work of monitoring and constant improvement of the Integrated Master in Environmental Engineering. No less important was the contribution of other teachers who also marked me on this journey. I will not name everyone but I leave this recognition. Thanks also for the vote of confidence I have always had from all my graduation colleagues and from another course years. It was a great pleasure to represent you and I hope I have always done my work in the best way for all, both in the Monitoring Committee and in the Pedagogic Council of FEUP.

I also highlight the friends I have made over these years, most notably Catarina Castro, Catarina Santos, Carmen, Cátia, Helena, João and Patrícia. I met everyone at FEUP and at the MIEA, with them I lived some of the best moments of the academic world and I hope to preserve through life the connection that we have created here. And I express a special thanks to Cristina, André and Joana Lopes, my lunch hour friends. I only met them this year but they were incredible people whose friendship I hope to preserve. I emphasize the sweetness and genuine instinct of Cristina, always very dear with me and ready to support in the most difficult moments of the work.

And last but not least, it is the gratefulness to the family and friends with whom I have grown and who believed in me throughout my life. I address especially to António Moisés, Carina, Célia, Beatriz, Bruno, Flávia Neves, Joana Marques, João Tiago, Lurdes, Maria and Tânia because I know they are happy with my success and because it is with them that I share the sum of all achievements I had. And of these, I emphasize my gratefulness to Joana Marques, Maria and João Tiago with whom I have so often shared my daily moments. To have you all in my life is a pleasure that I always want to preserve!

Abstract

Global warnings for the preservation of the environment and its resources are increasingly a constant that comes through the various means of communication. What, until just over 10 years ago, was a simple matter of raising awareness is today a request for immediate action. One of the problems that emerge within these concerns is the change in the global climate scenario, caused by the emission of greenhouse gases.

International agencies reports have shown that the energy sector, relying mostly on fossil fuels, which account for *ca.* 90 % of the global energy needs, is one of the biggest obstacles for a sustainable environment. Investment in solar technologies, which is expected to grow further, is bringing some hope but, the intermittent nature of the Sun contrasts with the permanent need to have electricity, which creates a technological challenge to overcome. Scientific researches in this sector have shown that one way to overcome this problem is by storing energy from the Sun in chemical fuels of high energy density, produced with clean and low-cost techniques. Among available chemical fuels, hydrogen, generated by solar powered water electrolysis in a photoelectrochemical (PEC) cell offers a promising route for solar energy storage.

PEC research efforts rely on designing abundant, efficient and stable semiconductors that can reach the target of 10 % solar-to-hydrogen efficiency, needed for commercialization. In this sense, the main goal of this work aimed at optimizing hematite photoelectrodes performance, the most stable metal-oxide semiconductor reported to date, that suffers from extremely low mobility of charges and high electron-hole recombination as the main limitations.

To suppress hematite's limitations, two strategies were used: a nanostructuring approach to provide a high surface area for good light harvesting while allowing higher charge extraction efficiencies, and the surface coating with efficient and stable co-catalysts for improving the slow water oxidation kinetics. The first motivation and challenge of this thesis was the optimization of a mesoporous structure with SiO₂ nanoparticles deposited by spin coating, showing a thickness of *ca.* 193 nm. The SiO₂ nanostructured template was coated with an atomic layer deposition (ALD) TiO₂ conductive thin layer and then with a hematite thin film. The most suitable techniques for homogeneous thin film depositions are spray pyrolysis and ALD. The hematite semiconductor was deposited by spray pyrolysis and an optimization was performed to study the effect of film thickness on the SiO₂ nanostructured template coated with a TiO₂ layer.

In the present study, the use of a conductive underlayer of TiO₂ allowed to obtain a higher performance compared with the TEOS (tetraethyl orthosilicate) pretreatment, mainly because it acts as a Ti doping source. For the optimized hematite thin film of *ca.* 30.6 nm (obtained by depositing 30 mL of the iron precursor) on top of the SiO₂ mesoporous template coated with the TiO₂ underlayer, a photocurrent improvement of more than 17 % was obtained compared to a hematite thin film with a TiO₂ underlayer. After the deposition of an abundant and cheap co-catalyst of FeNiOOH, a high photocurrent density of *ca.* 0.98 mA·cm⁻² at 1.45 V_{RHE} was obtained. The water oxidation efficiency was enhanced with values above 90 % for potentials higher than 1.00 V_{RHE} due to faster charge transfer and reduced electron-hole recombination at FeNiOOH coated hematite nanostructured photoelectrode. Therefore, electrochemical impedance spectroscopy proved to be a useful technique to understand the charge transfer processes occurring within the semiconductor bulk and at the semiconductor/electrolyte interface.

Keywords: Global warming, solar water splitting, photoelectrochemical cells, mesoporous SiO₂ template, hematite photoelectrodes

Resumo

Os alertas globais para a preservação do meio ambiente e seus recursos são cada vez mais uma constante que nos surge através dos vários meios de comunicação. O que, até há pouco mais de 10 anos atrás, era uma questão simples de sensibilização é hoje um pedido de ação imediata. Um dos problemas que emerge dentro dessas preocupações é a mudança do panorama climático global, causada pela emissão de gases de efeito estufa.

Relatórios realizados por agências internacionais têm demonstrado que o setor energético depende majoritariamente de combustíveis fósseis, responsáveis por cerca de 90 % das necessidades energéticas globais, sendo um dos maiores obstáculos para um ambiente sustentável. O investimento nas tecnologias solares como fontes renováveis de energia, que se prevê crescer ainda mais, traz alguma esperança, mas a natureza intermitente do Sol contrasta com a necessidade permanente de ter eletricidade, o que cria um desafio tecnológico a ser superado. As investigações desenvolvidas neste setor têm demonstrado que uma forma de ultrapassar este problema é através do armazenamento da energia proveniente do Sol em combustíveis químicos de elevada densidade energética, produzidos com técnicas limpas e de baixo custo. Entre os combustíveis químicos disponíveis, o hidrogénio, gerado pela eletrólise da água a energia solar em uma célula fotoeletroquímica (do inglês “photoelectrochemical” - PEC), oferece uma rota promissora para o armazenamento de energia solar.

Os esforços de investigação na área das células PEC focam-se na procura de semicondutores abundantes, eficientes e estáveis que alcancem 10 % de eficiência de conversão de energia solar em hidrogénio, necessária para a comercialização. Nesse sentido, o principal objetivo deste trabalho concentrou-se na otimização do desempenho de fotoelétrodos de hematite, o óxido metálico mais estável reportado até à data, que tem uma baixa mobilidade de cargas e elevada recombinação de elétron-lacuna como principais limitações.

Para contornar as limitações da hematite, foram adotadas duas estratégias: a nanoestruturação de forma a conferir uma alta área superficial e uma boa absorção de luz, para aumentar a eficiência de extração de cargas e o revestimento da superfície com co-catalisadores eficientes e estáveis para melhorar a cinética da reação de oxidação da água. A primeira motivação e desafio desta tese passaram pela otimização de uma estrutura mesoporosa de nanopartículas de SiO₂ depositadas por revestimento por rotação (do inglês “spin coating”), tendo-se obtido uma espessura ótima de cerca de 193 nm. O filme nanoestruturado de SiO₂ foi revestido com uma camada condutora de TiO₂ através da técnica de deposição em camada atômica (do inglês “atomic layer deposition” - ALD), onde depois foi

depositado um filme fino de hematite. As técnicas mais adequadas para deposição de filmes finos homogêneos são o “spray pyrolysis” e o ALD. O semicondutor de hematite foi depositado por “spray pyrolysis” e a otimização foi realizada para estudar o efeito da espessura deste filme sobre a matriz nanoestruturada de SiO₂ revestida com TiO₂.

No presente estudo, o uso de uma subcamada condutora de TiO₂ permitiu obter um melhor desempenho em comparação ao pré-tratamento com TEOS (tetraetil ortosilicato), principalmente por atuar como fonte de dopagem de Ti. Para o filme fino de hematite otimizado com cerca de 30.6 nm (obtido pela deposição de 30 mL de precursor de ferro) na superfície do filme mesoporoso de SiO₂ revestido com uma camada de TiO₂, foi obtida uma melhoria da fotocorrente superior a 17 % em comparação com um filme fino de hematite com uma camada inferior de TiO₂. Após a deposição de um co-catalisador abundante e barato de FeNiOOH, foi obtida uma alta densidade de fotocorrente de cerca de 0.98 mA·cm⁻² a 1.45 V_{RHE}. A eficiência de oxidação da água foi aumentada com valores acima de 90 % para potenciais superiores a 1.00 V_{RHE} devido à transferência de carga mais rápida e à recombinação reduzida de elétrons no fotoelétrodo nanoestruturado de hematite revestido com FeNiOOH. Portanto, a espectroscopia de impedância eletroquímica provou ser uma técnica útil para entender os processos de transferência de carga ocorrendo no interior do semicondutor e na interface semicondutor/eletrólito.

Palavras-chave: Aquecimento global, hidrólise solar da água, células fotoeletroquímicas, matrizes mesoporosas de SiO₂, fotoelétrodos de hematite.

Declaration

I hereby declare, on my word of honour, that this work is original and that all non-original contributions were properly referenced with source identification.

Filipe Moisés da Mota Francisco

Porto, 25 de Junho de 2018

Index

1	Introduction.....	1
1.1	Motivation	1
1.2	Presentation of the laboratory	4
1.3	Scientific contributions of the work.....	5
1.4	Organization of the thesis.....	6
2	Context and state of the art	9
2.1	Photoelectrochemical cells: basic principles of operation.....	9
2.2	Hematite as a promising semiconductor material	11
2.3	Strategies for improving α -Fe ₂ O ₃ performance.....	12
3	Materials and methods	21
3.1	Glass substrate preparation	21
3.2	SiO ₂ nanostructured film	22
3.3	Atomic Layer Deposition (ALD) technique	24
3.4	Spray pyrolysis technique	26
3.4.1	Spray pyrolysis setup and hematite deposition conditions	26
3.4.2	Electrodeposition of FeNiOOH co-catalyst.....	28
3.5	Samples characterization.....	28
3.5.1	Photoelectrochemical characterization	28
3.5.2	Morphology and films thickness characterization	30
4	Results and Discussion	31
4.1	SiO ₂ film optimization.....	31
4.1.1	Preliminary tests	31
4.1.2	Film optimization	35
4.2	Hematite thin films preparation	38
4.2.1	Deposition of hematite by ALD	38
4.2.2	Deposition of hematite by spray pyrolysis.....	40
4.2.3	TEOS pre-treatment vs. TiO ₂ conductive underlayer	41

4.2.4	Hematite film optimization	42
4.2.5	EIS analysis	46
5	Conclusion.....	55
6	Assessment of the work done	57
6.1	Objectives Achieved.....	57
6.2	Limitations and Future Work	57
6.3	Final Assessment	57
Appendix A - Brunauer-Emmet-Teller (BET) method (basic principles of A_s (BET) calculation)		65
Appendix B - Atomic Layer Deposition operation		67
B.1	TiO ₂ deposition (operating conditions)	69
B.2	Hematite deposition (operating conditions)	70
Appendix C - Hematite film thickness calculation.....		73

List of Figures

<i>Figure 1-1: Primary energy global production by fuel, in 2016.[3]</i>	1
<i>Figure 1-2: CO₂ emissions by fuel in 2015.[7]</i>	2
<i>Figure 1-3: Renewable electricity capacity growth by technology (based on [11]).</i>	3
<i>Figure 1-4: Scheme of prepared three-dimensional photoelectrode.</i>	6
<i>Figure 2-1: Photoelectrochemical cell with corresponding energy diagram (based on [5]).</i>	9
<i>Figure 2-2: Band edge positions of semiconductors in contact with the aqueous electrolyte at pH = 0 relative to NHE and the vacuum level (based on [21]). Hematite is marked in orange.</i>	11
<i>Figure 2-3: Strategies to obtain an ideal hematite photoanode (based on [15]).</i>	13
<i>Figure 2-4: SEM images and representative schemes of hematite nanostructures prepared using different deposition techniques (adapted from [20]).</i>	17
<i>Figure 3-1: Devices used on the FTO-glass substrates preparation (A: glass cutter; B: printer to mark glass; C: ultrasonically washing glass; D: plasma treatment).</i>	21
<i>Figure 3-2: SiO₂ paste preparation (A: stirring plate and ultrasonic stirring system to dissolve silicon oxide particles; B: stirring plate for mixing ethyl cellulose and ethanol).</i>	23
<i>Figure 3-3: Ethanol vaporization on the SiO₂ paste preparation (A: mechanical stirrer used to help ethanol evaporation process; B: heating bath).</i>	23
<i>Figure 3-4: SiO₂ paste deposition and sintering (A: spin coater used for paste deposition; B: oven used for sintering the deposited SiO₂ paste on top of FTO-glass substrates).</i>	24
<i>Figure 3-5: ALD general reaction mechanism.</i>	25
<i>Figure 3-6: Scheme of the spray pyrolysis system.</i>	27
<i>Figure 3-7: Electrochemical characterization setup (A: “Cappuccino” cell used in the samples characterization; B: setup assembled with three electrodes configuration).</i>	28
<i>Figure 3-8: Devices used for PEC characterization (A: source power of the class B solar simulator; B: ZENNIUM workstation; C: solar simulator).</i>	29
<i>Figure 4-1: Sample with film deposited using evaporated paste (A: surface photograph; B: surface view using SEM, 300 x; C: Cross-section view, 890 x).</i>	32
<i>Figure 4-2: SiO₂ mesoporous film thickness variation as a function of the spin coating deposition time (at 5000 rpm speed) according different dilutions of terpineol: 3 mL (○) and 4 mL (○). Lines represented are just a guide to the eye.</i>	33
<i>Figure 4-3: SiO₂ mesoporous film thickness variation as a function of the spin coating deposition speed (at 90 s deposition time) according different dilutions of terpineol: 3 mL (○) and 4 mL (○). Lines represented are just a guide to the eye.</i>	33

Figure 4-4: SiO₂ mesoporous film thickness variation as a function of the deposition time under additional preliminary tests conditions (at 6000 rpm spin coating speed) for non-evaporated (●) and evaporated (○) pastes. Lines represented are just a guide to the eye. 34

Figure 4-5: SEM images of the SiO₂ mesoporous films prepared using non-evaporated paste (A: surface view using SEM, 300 x; B: Cross-section view, 2900 x) and evaporated diluted paste (C: surface view using SEM, 300 x; D: Cross-section view, 8500 x). 35

Figure 4-6: SiO₂ mesoporous film thickness variation as a function of the deposition time (at 6000 rpm spin coating speed). A: particles A, non-evaporated paste diluted with 4 mL (▪), 8 mL (▫) and 16 mL (◊); B: particles A evaporated paste diluted with 4 mL (□), 8 mL (◻) and 16 mL (◼); C: particles B, non-evaporated paste diluted with 4 mL (●), 8 mL (◐) and 16 mL (◑); D: particles B evaporated paste diluted with 4 mL (○), 8 mL (◒) and 16 mL (◓). 36

Figure 4-7: SiO₂ mesoporous film thickness variation as a function of the terpeneol volume used in the paste dilutions (at 6000 rpm spin coating speed and at 240 s deposition time) for the evaporated paste with particles A (□); non-evaporated paste with particles A (▪); evaporated paste with particles B (○); and non-evaporated paste with particles B (●). 37

Figure 4-8: Cross-section SEM image (75000 x) of the SiO₂ mesoporous film prepared with particles B and deposited using the optimized conditions mentioned above. 38

Figure 4-9: Glass substrates after hematite film deposition using ALD technique. 38

Figure 4-10: J-V characteristic curves for the hematite photoelectrodes deposited on top of TiO₂ (TiO₂-H) and TEOS (TEOS-H) underlayers, in the dark (dashed lines) and under simulated solar illumination conditions (solid lines). 41

Figure 4-11: J-V characteristic curves for the samples with SiO₂ mesoporous film coated with a TiO₂ conductive layer for 42 mL Fe(AcAc)₃ volume deposited, in the dark (dashed lines) and under simulated solar illumination conditions (solid lines). 42

Figure 4-12: J-V characteristic curves for the hematite samples deposited on top of SiO₂ mesoporous film coated with a TiO₂ conductive layer (3DSiO₂-TiO₂-H) for different Fe(AcAc)₃ volumes deposited (15 mL, 30 mL, 42 mL and 60 mL). 43

Figure 4-13: Current density values obtained at 1.45 V_{RHE} as a function of deposited volume for hematite samples deposited on top of SiO₂ mesoporous template coated with TiO₂ underlayer. 44

Figure 4-14: Optimal sample (A: SEM surface image; B: SEM image amplification with hematite film growth; C: EDS analysis). 45

Figure 4-15: J-V characteristic curves for the samples with SiO₂ mesoporous film coated with a TiO₂ conductive layer for different Fe(AcAc)₃ volumes deposited - 30 mL with catalyst (H30 mL-FeNiOOH) and 30 mL without catalyst (H30 mL). 46

Figure 4-16: A: Nyquist plots obtained in the dark at 1.20 V_{RHE} for the prepared samples; and B: electrical circuit analogue used to fit the impedance data under dark conditions (extracted from [47]). 47

Figure 4-17: Mott-Schottky analysis of the hematite thin film deposited on top of: a TEOS underlayer (TEOS-H, ●), a TiO_2 underlayer (TiO2-H, ■), a nanostructured SiO_2 template and a TiO_2 underlayer (3DSiO2-TiO2-H, ◆), and a nanostructured SiO_2 template and a TiO_2 underlayer and followed by a FeNiOOH co-catalyst coating (3DSiO2-TiO2-H-FeNiOOH, ▲). 48

Figure 4-18: A: Nyquist plots obtained in the light at 1.20 V_{RHE} for the prepared samples; B and C: electrical circuit analogue used to fit the impedance data under light conditions (extracted from [47]). 50

Figure 4-19: Impedance parameters obtained from fitting the EIS data under illumination for the hematite thin film deposited. 50

Figure 4-20: A: Charge transfer rate constants, k_{CT} ; B: recombination rate constants, k_{rec} ; and C: water oxidation efficiencies, η_{OER} , for the hematite thin film deposited. 53

Figure A-1: Physisorption curves (A: particles A; B: particles B). 65

Figure B-1: ALD installation and operation (schematic picture). 68

Figure C-1: Behavior of radiation incident on a hematite photoelectrode. 73

List of Tables

<i>Table 2-1: Bibliographic revision about hematite deposition methods and their PEC performance (ordered by the generated photocurrent density, J_{photo}, in each type of nanostructure), showing the progress in morphology for solar water splitting.....</i>	<i>14</i>
<i>Table 3-1: SiO₂ nanoparticles properties and paste recipe composition.</i>	<i>22</i>
<i>Table 4-1: Preliminary tests (volume of terpineol added and deposition conditions).</i>	<i>32</i>
<i>Table 4-2: Additional preliminary tests conditions.</i>	<i>34</i>
<i>Table 4-3: Tests for SiO₂ mesoporous film optimization.</i>	<i>36</i>
<i>Table 4-4: Flatband potential (E_{fb}) and donor density concentration (N_D) values obtained from Mott-Schottky measurements in the dark for the photoelectrodes under study.</i>	<i>49</i>
<i>Table B-1: Acronym devices description from ALD scheme.</i>	<i>69</i>
<i>Table B-2: ALD process conditions for TiO₂ deposition.</i>	<i>70</i>
<i>Table B-3: ALD process conditions for hematite deposition.</i>	<i>71</i>

Notation and Glossary

Variable	Definition	Unit
A	Active área	cm^2
Abs	Absorbance	%
$A_{illuminated}$	Illuminated área	cm^2
A_S (BET)	BET specific area of the adsorbent (of mass m)	$\text{m}^2 \cdot \text{g}^{-1}$
C	Constant related to the monolayer adsorption energy	
$C_{ss,cat}$	Surface states capacitance for co-catalyst layer	F
C_{bulk}	Bulk capacitance	F
C_{ss}	Surface states capacitance	F
E	Applied potential	V
E_F	Fermi level at equilibrium	eV
E_{fb}	Flatband potential	V_{RHE}
E_{ox}^o	Oxidation standard potential	V_{NHE}
E_{red}^o	Reduction standard potential	V_{NHE}
E_T	Energy of the electron trap	eV
h	Planck's constant, 6.626×10^{-34}	J·s
$I_{measured}$	Measured current	mA
J_{photo}	Photocurrent	$\text{mA} \cdot \text{cm}^{-2}$
k	Boltzmann constant, 1.346×10^{-23}	$\text{J} \cdot \text{K}^{-1}$
k_{bulk}	Bulk electron trapping rate constant	s^{-1}
k_{CT}	Rate constant	s^{-1}
k_{rec}	Electron-hole recombination rate	s^{-1}
L	Avogadro's number, 6.022×10^{23}	mol^{-1}
l	Hematite film thickness	nm
N_D	Donor density	cm^{-3}
n_m	Specific monolayer capacity	mol
$n_{N_2,abs}$	Specific nitrogen amount adsorbed at the relative pressure p/p^o	mol
p	Nitrogen pressure injected in the BET device	mbar
p^o	BET measurement reference pressure	mbar
R_{Bulk}	Bulk charge transport resistance	Ω
R_C	Resistor-capacitor elemento	Ω
R_{CT}	Resistance of the semiconductor/electrolyte charge transfer	Ω
$R_{CT,cat}$	Surface states resistance from the co-catalyst/electrolyte charge transfer	Ω

$R_{CT,ss}$	Surface states resistance from the semiconductor/electrolyte charge transfer	Ω
R_{series}	Series resistance	Ω
T	Absolute temperature	K
$V_{Ag/AgCl}$	Potential provided by potentiostat to working electrode	V
$V_{Ag/AgCl}^{\circ}$	Potential of the Ag/AgCl reference electrode	V_{SHE}
V_{NHE}	Potential of the normal hydrogen electrode	V_{NHE}
V_{SHE}	Potential of the standard hydrogen electrode	V_{SHE}
V_{RHE}	Potential of the reversible hydrogen electrode	V_{RHE}
Z'	Real parte of impedance	Ω
Z''	Real parte of impedance	Ω
ΔE°	Standard electric reversible potential	V
ΔG°	Standard Gibbs free energy	$\text{kJ}\cdot\text{mol}^{-1}$

Greek symbols	Definition	Unit
α	hematite absorbance coefficient, 1/44	nm^{-1}
ϵ_0	Permissivity of the vacuum, 8.85×10^{-12}	$\text{C}\cdot\text{V}^{-1}\cdot\text{m}^{-1}$
ϵ_r	Dielectric constant of the semiconductor, 80	
η_{OER}	Water oxidation efficiency	%
ν	Photon's frequency	s^{-1}
σ_m	Molecular cross-sectional área	m^2
τ_{CT}	Time constant of charge transfer	s

Superscript	Definition
o	Standard conditions

Subscript	Definition
CB	Conduction Band
cat	Co-catalyst
CT	Charge transfer
NHE	Normal hydrogen electrode

ox	Oxidation Reaction
red	Reduction reaction
RHE	Reversible hydrogen electrode
SHE	Standard hydrogen electrode
SS	Surface states
VB	Valence Band

Abbreviation	Definition
ALD	Atomic Layer Deposition
AM	Air mass
APCVD	Atmospheric pressure chemical vapor deposition
BET	Brunauer-Emmett-Teller analysis
CE	Counter-electrode
CEMUP	Materials Center of the University of Porto
DV-BH1	Bubbler valve for hot source 1 (first precursor)
DV-BHA1	Carrier/purge gas valve for hot source 1 (first precursor)
DV-BL1	Bubbler tube valve for liquid source
DV-NP1	Vacuum pump gas ballast valve
DV-NV1	Vacuum chamber flow valve for process
DV-NV2	Vacuum chamber fast flow valve for venting
DV-PH1	Pulsing valve for hot source (first precursor)
DV-PL1	Pulsing valve for liquid source
DV-SN1	N ₂ inlet main valve
DV-VP1	Vacuum pump main valve
DV-VP2	Vacuum pump soft start valve
e ⁻	Electron
ED	Electrochemical deposition
EDS	Energy-dispersive X-ray spectrometer
EIS	Electrochemical impedance spectroscopy
FEUP	University of Porto, Faculty of Engineering

FTO	Fluorine tin-doped oxide
h^+	Hole
J-V	Characteristic curves (current density in function of potential)
LD	Hole diffusion length
LEPABE	Laboratory for Process Engineering, Environment, Biotechnology and Energy
PEC	Photoelectrochemical
PT-A1	Pressure transducer for hot source N ₂ tube monitoring
PT-A2	Pressure transducer for liquid source feeding tube monitoring
PT-C	Pressure transducer for vacuum chamber intermediate volume monitoring
PT-P1	Pressure transducer for pump line (reactor) pressure monitoring
PV	Photovoltaic
PVD	Physical vapor deposition
RC	Resistor-capacitor element
RE	Reference electrode
SEM	Scanning electron microscopy
SP	Spray pyrolysis
STH	Solar-to-hydrogen
TC-R	Sensor for reaction chamber temperature control and monitoring
TC-S1	Sensor for hot source 1 (first precursor) container temperature control and monitoring
TEOS	Tetraethyl orthosilicate
TI-S2	Sensor for liquid source 2 (second precursor) container temperature control
UPTEC	Science and Technology Park of the University of Porto
USP	Ultrasonic spray pyrolysis
WE	Working electrode

1 Introduction

Energy is a cornerstone of the global economy and modern lifestyle. Since fossil fuels were discovered, first coal and later oil and natural gas, and used to produce electricity, it was possible to develop a comfortable life style for humanity. However, fossil fuel reserves are limited and unevenly distributed across countries. In addition, fossil fuels emit greenhouse gases, notably CO₂, which is one of the current environmental challenges that has given rise to international concern.[1] International agreements to minimize greenhouse gas emissions and increase the sustainability of energy production were created and raised the need to promote alternative sources of energy, *i.e.* renewable and environmentally friendly resources. The development of energy harvesting and storage technologies from renewable sources is therefore necessary and is ruling, where renewable electricity is now cheaper than fossil fuel electricity and the price should further decline. However, most harvesting technologies produce no dispatchable electricity. Storage becomes then Achilles heel of energy from renewable sources.[2]

1.1 Motivation

Energy consumption reached record values, due to population increase and heavy industrialization, promoting it to one of the present main challenges to overcome. The global primary energy consumption in 2016, was *ca.* 17.6 TW, for a population of *ca.* 7 x 10⁹. Almost 90 % of the total energy was produced from fossil fuels (oil, coal and natural gas) and only 10 % originated from hydroelectricity and other renewable sources (wind, solar, geothermal, bioenergy), as shown in Figure 1-1. Moreover, an energy consumption expansion by 28 % in 2040, for a population of *ca.* 9 x 10⁹ people, is foreseen.[3-5]

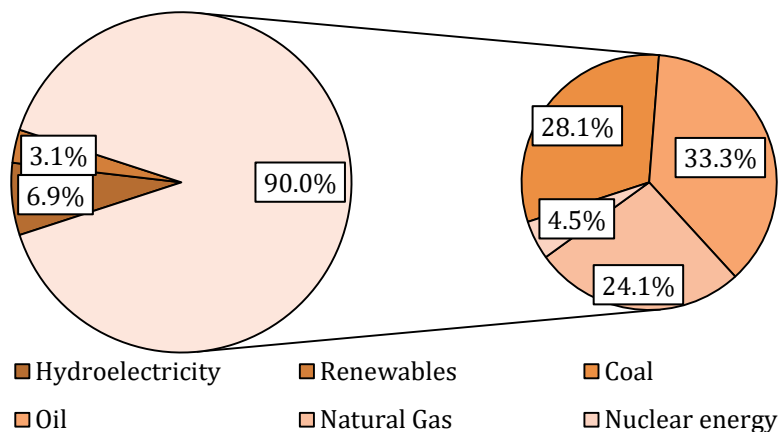


Figure 1-1: Primary energy global production by fuel, in 2016.[3]

Due to the current energy production dependence on fossil fuels, there are negative impacts both on the economy and environmental health of our planet that cannot be ignored. Fossil fuels stocks are limited and their price is, therefore, increasing considerably and it is expected to continue rising to prohibitive levels. Also, the emission of greenhouse gases from the oxidation of carbon in fuels during combustion is a far more serious concern with the detrimental effect on the carbon footprint and on climate change.[6]

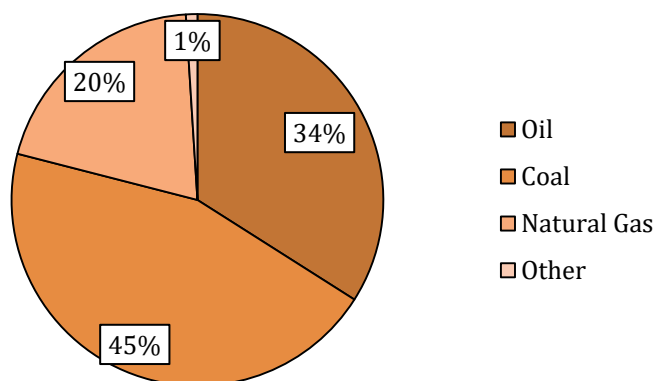


Figure 1-2: CO₂ emissions by fuel in 2015.[7]

In 2015, the global CO₂ emissions from fuel combustion reached 32.3 Gt of CO₂ whereof 45 % is allotted to coal and *ca.* 34 % to oil (Figure 1-2).[7] The CO₂ emissions continue to increase over the years, showing in 2016 *ca.* 3.5 % increase compared to 2015.[3] This scenario represents a serious problem that is already affecting our everyday lives and ecosystems. Reports about extreme weather phenomena are a constant in the media: *e.g.* on March 15th 2018, Euronews reported that “Earth experienced extreme heat and cold in February”, noting that in “some parts of the Arctic, daily temperatures were 30 degrees [30 °C] above the average over a week”. [8] Recently, Hughes *et al.* [9] also reported that in 2016, after record-breaking marine heatwave on the Great Barrier Reef, corals began to die on reefs due to accumulated heat exposure above the critical limit, where temperature increases can be 3 - 4 °C per week. As a result, after 8 months, 29 % of the 3863 reefs, which make up the largest coral reef system in the world, suffered a never-before-seen transformation of the three-dimensionality and ecological functioning.

But not all hope is lost as several international agreements were made to increase the global warming awareness, such as the Paris Agreement that has the main goal of limiting the average global temperature increase to 1.5 °C, above pre-industrial levels, through minimization of greenhouse gas emissions.[2] According to “CO₂ emissions from fuel combustion - highlights 2017”, a report of the International Energy Agency, coal is responsible for 42 % of global CO₂ emissions in the electricity and heat worldwide generation. However,

this trend is changing and in the last years a progressive switch from coal to natural gas is being observed. As an impact, 2015 was the first year in which global emission from coal combustion decreased significantly since the post-crisis rebound.[7] Decarbonization of our energy supply routes plays a very central role in future energy policies making it a major concern for an environmental engineering. Therefore, the exploitation of efficient and clean energy technological solutions becomes imperative in the new policies scenario. In Europe, renewable energy production needs to account for more than 50 % of total energy production by 2030.[10]

Renewable sources accounted for two-thirds of new power added to the electrical grid in 2016, with solar power as the fastest growing technology in the last five years, as shown in Figure 1-3. The Paris-based International Energy Agency, in the Renewables 2017 report, predicted that solar energy would dominate future growth, *i.e.* solar photovoltaics (PV) would surpass wind and hydro energy forms with a capacity for growth of *ca.* 438 GW from 2017 to 2022.[11] Indeed, the sun is the biggest renewable energy resource available in our planet, with the power to supply all the world energy needs. In fact, harvesting even a fraction (less than 0.1 %) of this clean renewable energy would be enough but it is still a big endeavor. Solar PV can produce electricity with the needed scalability; only 0.16 % of the Earth's surface area needs to be covered with 10 % efficient solar cells to fulfill the humankind energy consumption of *ca.* 20 TW.[5, 12] In spite of being a challenge, current developments in technology and societal/political changes are bringing this dream closer to reality than ever before.

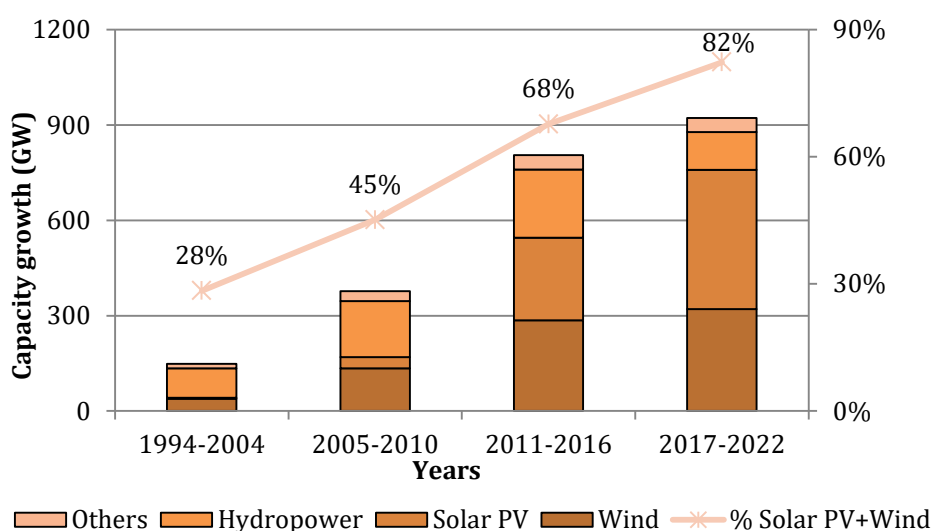


Figure 1-3: Renewable electricity capacity growth by technology (based on [11]).

Being sunlight nature intermittent, solar electricity is only produced during daytime and with favorable atmospheric factors, such as clouds that can induce instability in the electrical grid. The solution is to create storage technologies to serve as an intermediate between the

first phase of solar energy harvesting and electricity production and a second phase of energy consumption.[12, 13] Research developments indicate that capture of sunlight in the form of chemical fuels is one of the most practical ways for a large-scale solar driven economy.[14, 15] Besides energy storage, solar fuels have two more essential advantages: high energy storage densities and easy transportation to the final consumer, assuming a crucial role to replace high energy density fossil fuels.[16] Methane, methanol and hydrogen are good examples of chemical fuels, but hydrogen has become increasingly important because it does not require a source of carbon. Moreover, hydrogen (H_2) is easy to store and transport, has a high energy density of $143 \text{ MJ}\cdot\text{kg}^{-1}$ and is environmental friendly when generated from renewable sources.[5]

One of the most attractive ways to produce hydrogen from solar energy (solar water splitting) is through photoelectrochemical (PEC) devices. PEC devices offer the promise of direct solar fuels production through artificial photosynthesis with potential higher efficiencies and lower costs than standard PV-electrolyzers. Briefly, PEC cells combine light absorption and electrolysis in a single process, photoelectrolysis, unlike PV-electrolysis that needs two separate devices.[17] In addition, Pinaud *et al.*[18] estimated a cost of $10.40 \text{ USD}\cdot\text{kg}^{-1}$ of H_2 , assuming a solar-to- H_2 (STH) efficiency of 10 % and a lifetime of 10 years and a panel cost of $153 \text{ USD}\cdot\text{m}^{-2}$. Considering the same STH efficiency, Shaner *et al.*[19] reported that an electrolyzer stack and a PV module have a cost of $161 \text{ USD}\cdot\text{m}^{-2}$. However, STH efficiencies on PEC devices are still low, making new ways to improve their efficiencies necessary for pushing this technology into the market.[5, 20]

Over the last few years, PEC technology has improved significantly in many ways, but the development of an efficient, stable and low-cost semiconductor is still elusive. This thesis aims to contribute to the scientific effort of developing such material that could bring PEC solar water splitting closer to commercialization. Hematite ($\alpha\text{-Fe}_2\text{O}_3$) was selected for its promising features, such as stability and cost. The main goal of this work is to increase its efficiency by a novel host-guest nanostructuring approach that allows preserving a very thin layer of $\alpha\text{-Fe}_2\text{O}_3$ to minimize recombination whilst highly increasing surface area and light absorption.

1.2 Presentation of the laboratory

The Laboratory for Process Engineering, Environment, Biotechnology and Energy (LEPABE), as an interdisciplinary group, is today the largest research unit operating within Faculty of Engineering of the University of Porto (FEUP) in the fields of Chemical, Environmental and Biological Engineering. LEPABE is classified as “Excellent” by the various international evaluation panels appointed by the Science and Technology Foundation (FCT).

“From Science to Innovation” is the LEPABE’s slogan that has been enforced by the combination of basic science with applied engineering and innovation investing in scientific research and technological development, as well as in advanced training, technology transfer and stimulating the establishment of new technology-based companies. LEPABE’s scientific architecture comprises three main areas: 1) Environment and Health; 2) Energy, Processes and Products; 3) Biotechnology and Interfaces. The present work aims at the area (2) led by Professor Adélio Mendes, who directs research laboratories at the Chemical Engineering Department of FEUP and at Science and Technology Park of the University of Porto (UPTEC).

This research unit actually has UPTEC as a fundamental ally to support knowledge transfer between the university and the market. UPTEC has a strong interaction with the Chemical Engineering Department, aiming at the promotion and validation of business-oriented projects, based on the knowledge and skills generated within the University of Porto. At present, it includes 37 companies and innovation center that work on technological areas as vast as biotechnology, chemical engineering, energy, polymers and composite materials.

1.3 Scientific contributions of the work

Iron (III) oxide, also known as hematite, is a promising semiconductor material for PEC devices, mainly due to its favorable combination of availability, low cost, excellent stability and reasonably small bandgap (*ca.* 2.2 eV). However, α -Fe₂O₃ suffers from two major drawbacks: i) relation between long visible light absorption depth and an extremely low mobility of minority carriers (holes) and ii) fast electron-hole recombination kinetics. To overcome these limitations, it is possible to create high surface area materials by nanostructuring for good light absorption, with a small thickness to decrease charge recombination. This thesis proposes a new nanostructure based on an extremely high surface area silicon dioxide (SiO₂) template coated with a thin, conformal and dense layer of α -Fe₂O₃.

A thin mesoporous SiO₂ template (*ca.* 193 nm) was synthesized and optimized for this purpose, using particles with a surface area of *ca.* 141.6 m²·g⁻¹. An intermediate layer of titanium dioxide (TiO₂) was selected to act as conductive charge collector and was homogeneously deposited onto the template by atomic layer deposition (ALD). Finally, α -Fe₂O₃ was deposited by spray pyrolysis on the prepared host structure achieving onset potential of 1.00 V_{RHE} and photocurrent of 0.81 mA·cm⁻² at 1.45 V_{RHE}. Figure 1-4 shows a scheme of the prepared three-dimensional photoelectrode.

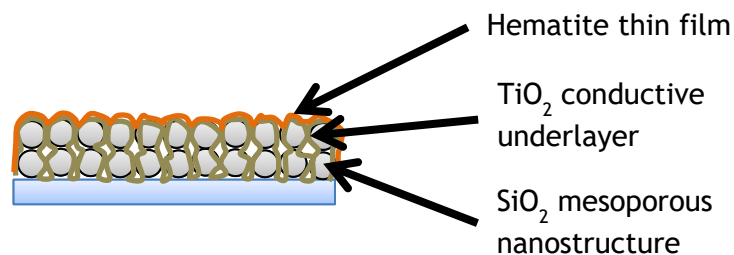


Figure 1-4: Scheme of prepared three-dimensional photoelectrode.

Current density could still be improved by 17 % through the use of FeNiOOH as a catalyst, and a value of *ca.* $0.98 \text{ mA}\cdot\text{cm}^{-2}$ at $1.45 \text{ V}_{\text{RHE}}$, with an onset potential of *ca.* $0.70 \text{ V}_{\text{RHE}}$ was achieved. This strategy already revealed performance improvement over thin films by reducing the electron-hole recombination and increasing the charge transfer within the bulk and interface of hematite, which proved to be a valid strategy for further improvements.

1.4 Organization of the thesis

Chapter 1 - Introduction

In this chapter, a brief introduction to the global energetic scenario and the relationship between current environmental challenges and the role of energy production was made. In this sense, it was justified the importance to invest in the renewable energy sources, particularly on solar technologies that allow storage and transport energy, like photoelectrochemical water splitting devices. The main goal of the present work, as well as its scientific contributions and the laboratory where it was developed, were also presented.

Chapter 2 - Context and state of the art

In this section, the working principles of a photoelectrochemical cell for water splitting were overviewed, emphasizing the role of the semiconductors in its operation. Hematite was selected as a promising semiconductor, and its advantages and challenges were summarized. It was also presented the deposition techniques that most influence the hematite performance, accompanied by a bibliographical review of the record-breaking performances obtained. Nanostructuring approaches applied to an electron conductive host scaffold coated by a thin layer of hematite guest absorber were advanced as the strategy to use within this work.

Chapter 3 - Materials and methods

A description of the procedures and techniques used to develop this work was presented in detail, namely for the washing and preparation of the glass substrates, paste preparation and deposition of the mesoporous SiO₂ film, the atomic layer deposition (ALD) of TiO₂

conductive underlayer, the deposition of the hematite by ALD and spray pyrolysis, and finally the characterization of the prepared photoelectrodes.

Chapter 4 - Results and discussion

In this section, the main results obtained throughout this thesis were presented and a detailed discussion was made. Not only were the achieved findings highlighted but also the obstacles that prevented better results, pointing out causes and possible future strategies.

Chapter 5 - Conclusions

This chapter summarizes the work developed during this thesis, relating the main conclusions and the performance improvements achieved.

Chapter 6 - Assessment of the work done

In this chapter, a reflection was made on the work developed, and suggestions for future work in the domain of the theme developed in the present master thesis were presented.

2 Context and state of the art

Photoelectrochemical cells for solar water splitting are the main focus of this dissertation, with special emphasis on the optimization of hematite nanostructured photoelectrodes. In this way, it is important to understand how these devices work and what is the role of hematite in their performance, mainly understanding hematite's advantages, limitations and scientific advances achieved so far, as will be detailed below.

2.1 Photoelectrochemical cells: basic principles of operation

A PEC cell is a device composed of two externally connected electrodes, with at least one of them being a photoelectrode, immersed in an electrolyte solution that allows the transport of ionic species.[21] In a PEC cell, the semiconductor is the component that converts incident photons to electron-hole (e^-/h^+) pairs. These pairs, provided with enough energy, can promote the necessary redox reactions to create chemical fuels. Depending on the major charge carriers (electrons or holes), two types of semiconductors, n-type and p-type respectively, can be used to form a semiconductor-liquid junction. When the junction is formed, electric current flows until electronic equilibrium is established. The transfer of electric charges creates a region in the electrolyte vicinity, where the distribution of charges differs in relation to the bulk material, being this known by space-charge layer. For an n-type semiconductor, when electrons are depleted from solid to the electrolyte solution, a depletion layer of negative charges will be obtained, *i.e.*, a positive excess charge, that creates a favorable field for electron injection into the semiconductor. For p-type semiconductors, the scenario is inverted, *i.e.*, the depletion layer of accumulated positive charges, facilitating electron injection into the electrolyte.[22] This semiconductor/electrolyte junction is the base of operation for a PEC cell.

A typical PEC system is illustrated in the Figure 2-1, with an energy diagram of an n-type semiconductor, working as photoanode, and a metallic cathode, working as counter-electrode.[5]

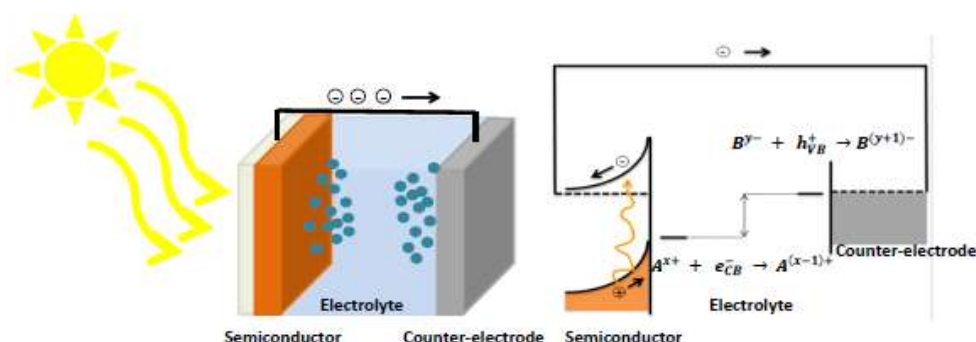
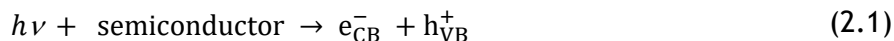


Figure 2-1: Photoelectrochemical cell with corresponding energy diagram (based on [5]).

When a photon, with energy ($h\nu$) equal to or higher than the semiconductor's bandgap, is absorbed by the semiconductor, an electron-hole pair is generated. Then, excited electrons jump to the conduction band (CB) leaving holes in the valence band (VB), as shown in the equation 2.1:[21]



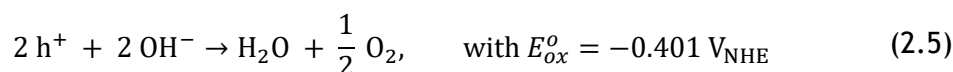
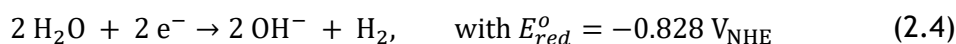
The photopotential generated by the subsequent separation of the photogenerated charges can directly drive an electrochemical solar-fuel-production reaction, provided a good energy alignment with the redox couples in solution. The excited electrons are transported to the counter electrode, via the external circuit, where they promote a reduction reaction, according to the generic formula of Equation 2.2:



On the other hand, in the valence band, holes migrate to the photoanode's surface, promoting an oxidation reaction, according to the generic formula of Equation 2.3:



In the case of a PEC water splitting cell for hydrogen generation composed by an n-type semiconductor, the holes exhibit oxidation potential while the electrons are transferred to the counter-electrode to promote water reduction into hydrogen gas. In an alkaline media, Equations 2.2 and 2.3 can become respectively:[21, 23]



where, NHE stands for normal hydrogen electrode. The minimum thermodynamic potential needed for driving the water electrolysis is the electric reversible potential of $\Delta E^o = -1.23 \text{ V}$, with a Gibbs free energy change of $\Delta G^o = 237 \text{ kJ}\cdot\text{mol}^{-1}$ (at standard conditions: 298 K, 1 M and 1 bar).[24]

The semiconductor assumes a key role in the overall PEC cell performance, therefore it has to fulfil several requirements for an efficient solar fuel production:[23, 25]

- ✓ suitable bandgap size that allows for broad visible light absorption (absorb light with sufficient energy to promote the required electrochemical reactions and compensate thermodynamic losses existent over the entire system - optimal bandgap range of 1.9 eV and 2.4 eV[23, 26]);
- ✓ high chemical stability (particularly, against photo-corrosion where photo-generated holes are able to oxidize the semiconductor and/or electrons can reduce it);

- ✓ suitable band-edge position to enable reduction and oxidation reaction (e.g. if it is considered NHE scale, conduction potential should be more positive than reduction potential and valence potential should be more negative than oxidation potential, otherwise a bias potential can be added to induce reactions, making this criterion less strict);
- ✓ low kinetic overpotentials for the reduction/oxidation reaction;
- ✓ efficient charge transport within the semiconductor (which is conditioned by electron and hole mobility);
- ✓ Earth-abundant and cost-effective.

Due to the previously mentioned stringent requirements, identifying a single semiconductor that fulfils all of them is a challenge. In 1970's, Fujishima and Honda were pioneers in research studies about PEC water splitting, having used a single crystalline TiO_2 photoanode and a platinum cathode, under ultraviolet irradiation and applying an external bias. Since that time, other metal oxide photoelectrode materials have been studied, such as tungsten trioxide (WO_3), $\alpha\text{-Fe}_2\text{O}_3$, bismuth vanadate (BiVO_4), cuprous oxide (Cu_2O) or tantalum nitride (Ta_3N_5). Figure 2-2 shows the band-edge positions of various semiconductors, along with the reduction and oxidation potentials of water. [20]

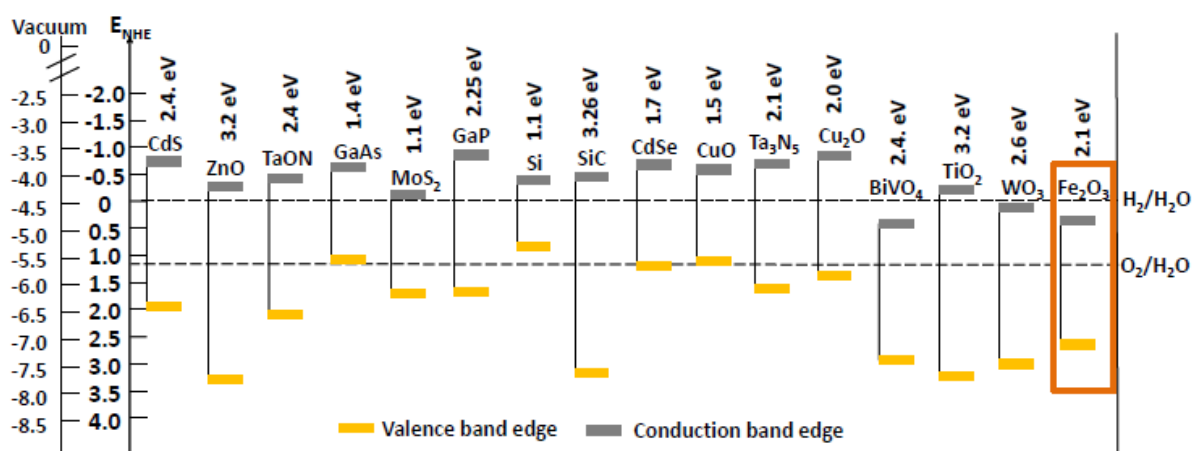


Figure 2-2: Band edge positions of semiconductors in contact with the aqueous electrolyte at $\text{pH} = 0$ relative to NHE and the vacuum level (based on [21]). Hematite is marked in orange.

2.2 Hematite as a promising semiconductor material

Hematite emerged as one of the most studied and promising photoelectrodes in the PEC water splitting field. It has a well-aligned valence band maximum for oxidation reaction (Figure 2-2) and fulfills almost all of the above-mentioned criteria for a suitable semiconductor. Iron represents 6.3 % by weight in the earth's crust and can be considered as one of the most available elements. Because of the ease of being oxidized by air to the

ferrous (+2) and ferric (+3) states, iron oxides are highly Earth-abundant and nontoxic. From all the iron oxide phases available in nature, $\alpha\text{-Fe}_2\text{O}_3$ is the most abundant and thermodynamically stable form of iron oxide under ambient conditions.[27] In addition, hematite is also probably the cheapest semiconductor that absorbs a substantial fraction of visible light, namely due to its bandgap energy between 1.9 and 2.2 eV corresponding to a wavelength from 650 to 560 nm.[20, 28, 29] With an average bandgap of 2.1 eV, $\alpha\text{-Fe}_2\text{O}_3$ has a maximum theoretical STH conversion efficiency of *ca.* 15 %, corresponding to a photocurrent density of *ca.* $12.5 \text{ mA}\cdot\text{cm}^{-2}$.[30]

The first study on the hematite ability for water photolysis was performed in 1976 by Hardee and Bard[20, 31] that found it to be stable in neutral and alkaline electrolyte solutions. Very recently, Dias *et al.*[31] reported a bare hematite thin film (*ca.* 19 nm) that showed a record-breaking stability over 1000 h of PEC operation under 1-sun AM 1.5 G illumination, with no evidence of film degradation or of photocurrent density losses.

Despite having a small bandgap, long-term stability and a theoretical efficiency that exceeds the STH benchmark of 10 % required for practical applications, the highest STH efficiency achieved so far with hematite was only 3.1 %.[32] Therefore, the hematite performance is mainly limited by the following characteristics:[27]

- i. large overpotential for water oxidation reactions;
- ii. low majority carrier conductivity, requiring high doping levels to increase ionized donor concentration and respective electrical conduction;
- iii. need for greater depths for photons penetration with thicker films (400-500 nm) in order to overcome the characteristic low coefficient of absorption;
- iv. short hole diffusion length ($L_D = 2 - 4 \text{ nm}$) and extremely low mobility of minority carriers;
- v. slow water oxidation reaction step (up to 3 s) in contrast with a very fast electron-hole recombination (3-10 ps).[33, 34]

For obtaining lower recombination effects and then higher photocurrents, the hematite photoelectrodes should combine good light absorption while simultaneously providing a short pathway for holes to reach the electrolyte.

2.3 Strategies for improving $\alpha\text{-Fe}_2\text{O}_3$ performance

Past research efforts with $\alpha\text{-Fe}_2\text{O}_3$ photoelectrodes aimed at: i) improving the generated photocurrent density through the optimization of morphology (*e.g.* nanowires[35], nanocones[36], nanotubes[37], nanoflowers[38]) and the introduction of dopant elements (*e.g.* Si[39], Ti[40], Sn[41], Pt[42] and Zn[43]) and ii) reducing the required overpotential by employing various surface treatments (*e.g.* through co-catalysts of Co-Pi[44], $\text{Ni}_x\text{Fe}_{1-x}\text{O}_y$ [45],

Ni(OH)₂/IrO₂[46], RuO₂/IrO₂[47] and Ti-FeOOH[48]), which also enhances the generated photovoltage and decreases the electron/hole recombination. To reach the performance of an ideal hematite photoanode, these two strategies should be combined - Figure 2-3.[15]

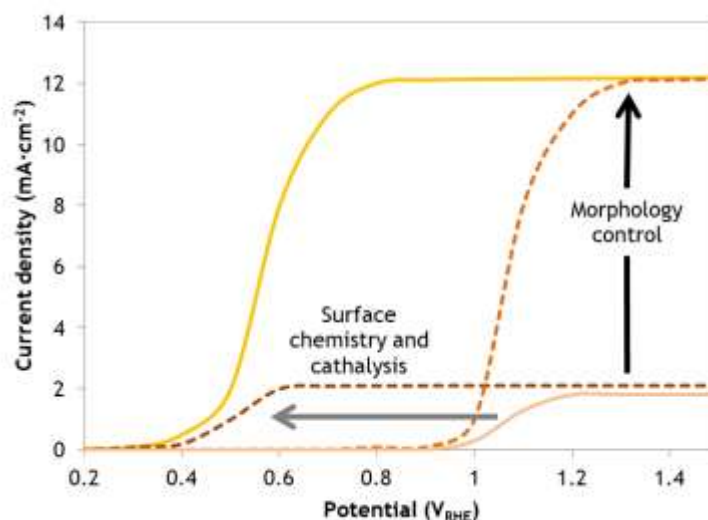
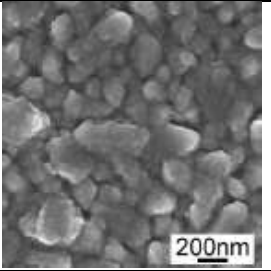
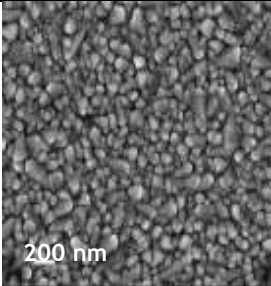
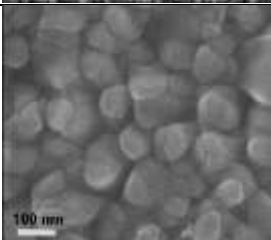
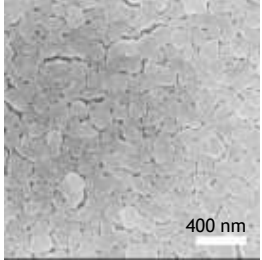
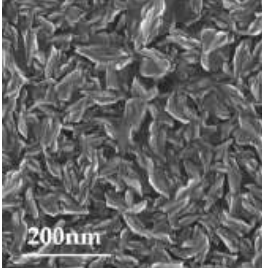
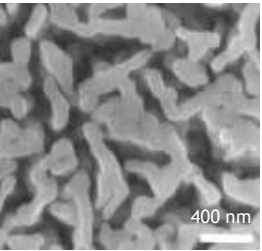
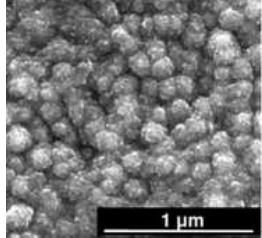


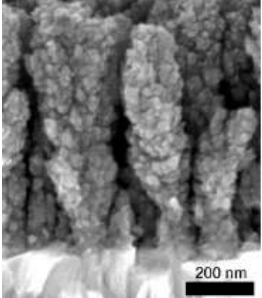
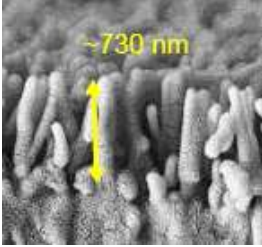
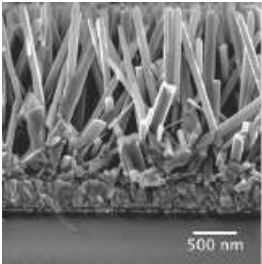
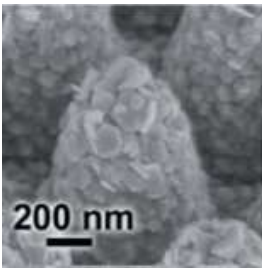
Figure 2-3: Strategies to obtain an ideal hematite photoanode (based on [15]).

The present work aims at controlling the morphology of hematite photoelectrodes to optimize the feature size/film thickness at nanometer length scale whilst creating an extremely high surface area. The morphology of hematite structure, which influence its performance, is strongly related to the synthesis methods. Table 2-1 summarizes the major advances in the morphological evolution of hematite photoelectrodes prepared using different techniques for PEC water splitting applications.

Table 2-1: Bibliographic revision about hematite deposition methods and their PEC performance (ordered by the generated photocurrent density, J_{photo} , in each type of nanostructure), showing the progress in morphology for solar water splitting.

Type of nanostructure	SEM Image/ Schematic Picture	Technique	Thickness	Dopant/ Treatment	PEC conditions	PEC performance (J_{photo} at 1.23 V_{RHE} ; onset potential; stability)	Ref.
Hematite nanostructure applied on top of typical FTO-glass substrate							
Bulk		Sputtering Deposition	27 nm	None/ None	1 M KOH/ 40 $mW \cdot cm^{-2}$	0.2 $mA \cdot cm^{-2}$; 1.1 V_{RHE}	[49]/ 2015
Bulk		Pulsed Layer Deposition (PLD)	30 nm	<i>n-i-p</i> : Ti (<i>n</i> -type) - Zn (<i>p</i> -type)/ None	1 M NaOH/ 100 $mW \cdot cm^{-2}$	0.5 $mA \cdot cm^{-2}$; 1.1 V_{RHE}	[50]/ 2016
Bulk		Atomic Layer Deposition (ALD)	20 nm	Ti-doped/ Annealing at 800 °C and Co-Pi co-catalyst	1 M KOH/ 100 $mW \cdot cm^{-2}$	0.7 $mA \cdot cm^{-2}$; 0.6 V_{RHE} ; stable over 60 min	[51]/ 2014

Bulk		Electrodeposition (ED)	59 nm	None/ Annealing at 800 °C and Co-Pi co-catalyst	1 M KOH/ 100 mW·cm ⁻²	0.8 mA·cm ⁻² ; 0.9 V _{RHE}	[52]/ 2016
Bulk		Ultrasonic Spray Pyrolysis (USP)	100 nm	None/ None	1 M NaOH/ 130 mW·cm ⁻²	1.1 mA·cm ⁻² ; 0.9 V _{RHE}	[53]/ 2005
Nano-platelets		Electrodeposition (ED)	59 nm	None/ Annealing at 800 °C and Co-Pi co-catalyst	1 M KOH/ 100 mW·cm ⁻²	1.1 mA·cm ⁻² ; 0.9 V _{RHE}	[52]/ 2016
Bulk		Spray Pyrolysis (SP)	19 nm	None/ Annealing at 800 °C and RuO ₂ /IrO ₂ co-catalysts	1 M NaOH/ 100 mW·cm ⁻²	1.5 mA·cm ⁻² ; 0.5 V _{RHE} ; stable over 72 h	[47]/ 2017

Nanoflowers		Atmospheric Pressure Chemical Vapour Deposition (APCVD)	700 nm	Si-doped (TEOS)/ IrO ₂ co-catalyst	1 M NaOH/ 100 mW·cm ⁻²	3.0 mA·cm ⁻² ; 0.9 V _{RHE} ; stable over 200 s	[54]/ 2010
Nanowires		Solution-based Colloidal	750 nm	None/ H ₂ treatment and Co-Pi co-catalyst	1 M KOH/ 100 mW·cm ⁻²	6.0 mA·cm ⁻² ; 0.6 V _{RHE} ; stable over 100 h	[55]/ 2017
Hematite guest absorber coated on top of an electron conductive host scaffold							
Nanowires		Atomic Layer Deposition (ALD)	10 nm	TiO ₂ nanowires scaffold/ Ni(OH) ₂ co-catalyst	1 M NaOH/ 100 mW·cm ⁻²	0.3 mA·cm ⁻² ; 0.8 V _{RHE}	[56]/ 2015
Nanocones		Ultrasonic Spray Pyrolysis (USP)	90-100 nm	Ti-doped/ Co-Pi co-catalyst	1 M NaOH/ 100 mW·cm ⁻²	2.4 mA·cm ⁻² ; 1.0 V _{RHE}	[57]/ 2014

For preparing dense films with a planar bulk structure, the main deposition techniques used are spray pyrolysis (SP) or ultrasonic spray pyrolysis (USP), electrochemical deposition (ED), and atomic layer deposition (ALD), which allow to obtain a large range of films thicknesses, *e.g.* according to the time of deposition. In the case of thicker planar $\alpha\text{-Fe}_2\text{O}_3$ films, the majority charge carriers (holes) need to travel bigger distances to be collected or to react, increasing the recombination and, consequently, producing a negligible photocurrent.[20] Another problem with the thick films is that there is a high mechanical stress between the hematite film and the substrate, which causes defects, also promoting recombination phenomena. Therefore, thin films are considered more suitable for PEC applications, but they absorb a smaller fraction of light (depending on their absorption coefficient) and present a small surface area, which decreases the photoelectrode efficiency. The highest performance achieved with a hematite thin film, intrinsically Sn-doped and coated with $\text{RuO}_2/\text{IrO}_2$ co-catalysts, was $1.52 \text{ mA}\cdot\text{cm}^{-2}$ at $1.23 \text{ V}_{\text{RHE}}$, reported by Dias *et al.*[47]. Nanostructured hematite photoelectrode design can solve the above-mentioned problems, also offering a large interfacial area between the co-catalyst and the electrolyte, which should result in higher photocurrents and better charge extraction efficiencies.[20, 58] Atmospheric pressure chemical vapor deposition (APCVD)[54], physical vapor deposition (PVD)[59], and solution-based colloidal[60] methods allow to obtain different types of hematite nanostructures, such as nanoparticles, nanoflowers, nanowires, nanotubes and nanocones - Figure 2-4.[20, 58, 61, 62]

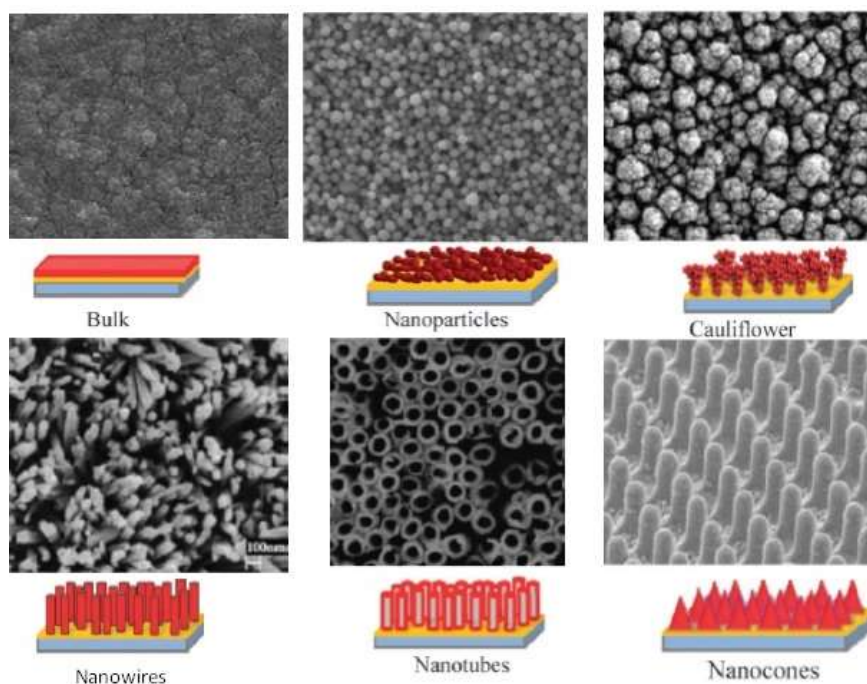


Figure 2-4: SEM images and representative schemes of hematite nanostructures prepared using different deposition techniques (adapted from [20]).

The problems associated with nanoparticled hematite films are the high probability for recombination and poor transport across grain boundaries between particles.[63] Nanoflower, also known as cauliflower, is another nanostructured design that have shown good results in combination with improved doping and surface modification with more efficient oxygen evolution catalysts.[64] Tilley *et al.*[54] reported Si-doped α -Fe₂O₃ cauliflower nanostructured photoelectrodes prepared by APCVD and catalysed with IrO₂ nanoparticles, displaying a photocurrent density of *ca.* 3.3 mA·cm⁻² at 1.23 V_{RHE}. Nanowires and nanotubes with high aspect ratios and large surface areas are more advantageous, since they improve charge carrier collection and decrease recombination losses. Furthermore, if nanostructures with smaller diameters are used, the distance between holes and electrolyte-semiconductor interface is reduced, avoiding the poor charge transport limitation. Very recently, Jeon *et al.*[55] achieved a new record of *ca.* 6 mA·cm⁻² at 1.23 V_{RHE} stable over 100 h using hematite nanorod arrays, prepared by a solution-based colloidal method and modified by a hydrogen treatment, and coated with a TiO₂ overlayer and a Co-Pi co-catalyst.

Despite the recent improvements on hematite nanostructures, the charge transport limitations force the design towards thin films deposited on high surface area nanostructured conductive scaffolds. In such a nanostructured approach, recombination losses within the thin absorber material can be minimized while light absorption is adaptable by the adjustment of the nanostructure thickness. A good example is presented in Figure 2-4 for nanocone structures. In this photoelectrode configuration, a hematite film is deposited by USP on top of a nanocone template that is chemically stable. These structures display simultaneously a big surface area and enhanced light absorption, which allow obtaining a photocurrent density of *ca.* 3.4 mA·cm⁻² at 1.23 V_{RHE}. [57] Recently, Steier *et al.*[56] reported a similar approach, combining TiO₂ nanowires host scaffold and a hematite guest layer deposited by ALD and activated with a Ni(OH)₂ co-catalyst. Using hematite ultrathin films of *ca.* 10 nm, it was obtained *ca.* 0.3 mA·cm⁻² at 1.23 V_{RHE}, with an onset potential of *ca.* 0.9 V_{RHE}. ALD is a powerful technique to deposit conformal films onto high aspect ratio nanostructures, being also widely used for the fabrication of a large variety of thin films onto any substrate, such as oxides, nitrides and metals.[65] Though ALD was recently introduced to the PEC field, it has already enhanced research progress quite rapidly due to its precise control of the films thickness, homogeneity and conformity with low deposition rates and by dependence on the nature of precursor.[66] This makes it a valuable and powerful deposition technique for innovative research.

The motivation and challenge for the work presented in this master thesis is the design of a nanostructured conductive host-guest approach based on SiO₂ nanoparticles host scaffold supporting a thin guest layer of hematite. ALD and spray pyrolysis are suitable techniques for

allowing the deposition of uniform, homogenous and reproducible thin films of hematite on top of this mesoporous structure. With this arrangement it is expected to obtain higher photocurrents and better charge extraction efficiencies.

3 Materials and methods

The work developed follows a sequence of tasks and methods that will be detailed hereafter, from glass cutting and washing, to the preparation and deposition of the SiO₂ mesoporous template and deposition and characterization of hematite photoelectrodes.

3.1 Glass substrate preparation

Substrates were prepared using 2.2 nm thick TEC-7 ($7 \Omega \cdot \text{cm}^{-2}$, Solaronix[®]) FTO (fluorine tin-doped oxide) glass. Using a glass cutter (Figure 3-1A), $1.2 \times 3 \text{ cm}^2$ substrates were hand cut from glass plates, and then they were laser marked on the non-conductive side, using a VersaLaser[®] printer, to identify each one of them (Figure 3-1B). After marking, glass substrates were ultrasonically washed using a Amsonic[®] equipment (Figure 3-1C), firstly immersed in a cleaning solution (Alconox[®], VWR) for 10 minutes, secondly for 10 minutes in distilled water and finally for 5 minutes in a KOH (2 M in 70 % ethanol). After this, glass samples were washed for 10 minutes in distilled water and, at the end, dried with hot hair. To remove any remaining contamination of the surface, the substrates were treated in an argon plasma for 8 min (70 kW at 0.2 - 0.3 mbar; Diener electronic[®] Plasma Surface Technology - Figure 3-1D).

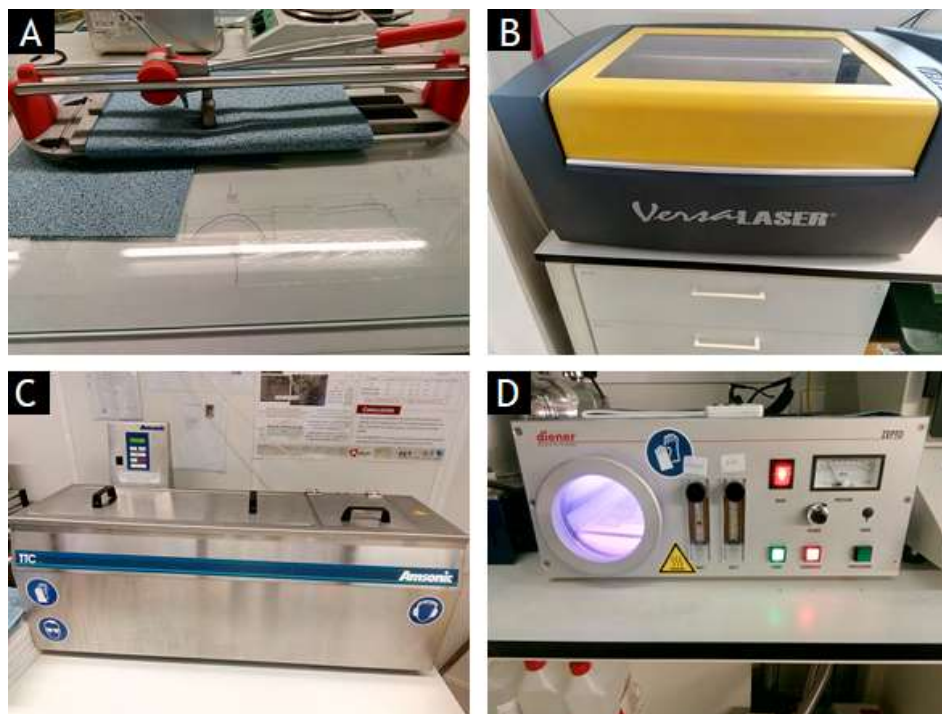


Figure 3-1: Devices used on the FTO-glass substrates preparation (A: glass cutter; B: printer to mark glass; C: ultrasonically washing glass; D: plasma treatment).

3.2 SiO₂ nanostructured film

To create a mesoporous film, first a liquid paste containing SiO₂ particles needs to be prepared and then applied onto a substrate by spin coating. Two different SiO₂ nanoparticles (Alfa Aesar®) were tested: A and B; their specific surface area was determined by BET (Brunauer, Emmett and Teller) analysis and is presented in Table 3-1. A brief explanation of the BET method and the parameters used are detailed in Appendix A.

Table 3-1: SiO₂ nanoparticles properties and paste recipe composition.

SiO ₂ particles	Paste recipe composition (wt. %)						
	A _s (m ² ·g ⁻¹)	SiO ₂	Ethyl cellulose	Ethanol (99%)	Acetic acid	Distilled water	Terpineol
A	87.8	5.6	2.1	76.7	0.7	0.7	14.1
B	141.6	4.4	1.7	81.8	0.6	0.6	11.0

The formulation of SiO₂ paste used to prepare a nanostructured film followed a previous study made in LEPABE, which was based on Ito *et al.*[67] work on TiO₂ paste optimization. Therefore, to prepare the SiO₂ paste, 100 mL or 150 mL of ethanol 99 % in the case of A or B nanoparticles, respectively (due to particle agglomerations), 1 mL of distilled water and 1 mL of acetic acid (CH₃COOH) were added to a glass bottle (Bottle A). This bottle was placed into a stirring plate with an ultrasound system (Figure 3-2A), and small portions of SiO₂ were added in time slots of 30 min, approximately, until a total of 8 g. At the end, 20 g of terpineol (Sigma-Aldrich® ref. W304506) were added, stirring for an additional hour. Simultaneously, 30 g of ethanol 99 % was gradually added to stir ethylcellulose (Sigma-Aldrich® ref. 46080), until a total 3 g, in another glass bottle (Bottle B) - Figure 3-2B. After, Bottle B content was poured into Bottle A, stirring for more 1 h. Paste viscosity, porosity and mechanical stability were conferred by ethyl cellulose. Ethanol 99 % and terpineol were used as solvents, allowing to control the viscosity. Acetic acid was used to avoid the formation of SiO₂ aggregates. Paste recipe composition is detailed on Table 3-1.

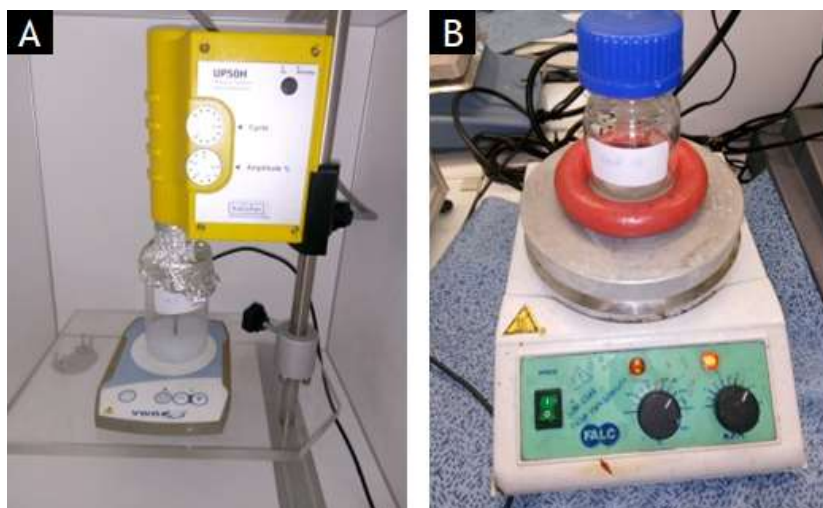


Figure 3-2: SiO_2 paste preparation (A: stirring plate and ultrasonic stirring system to dissolve silicon oxide particles; B: stirring plate for mixing ethyl cellulose and ethanol).

At the end, ethanol was evaporated, at a constant temperature of $75\text{ }^\circ\text{C}$, using a heating water bath (Julabo[®]) and an overhead mechanical torque stirrer (Heidolph[®]) with a stir of 300 rpm, as shown in Figure 3-3.

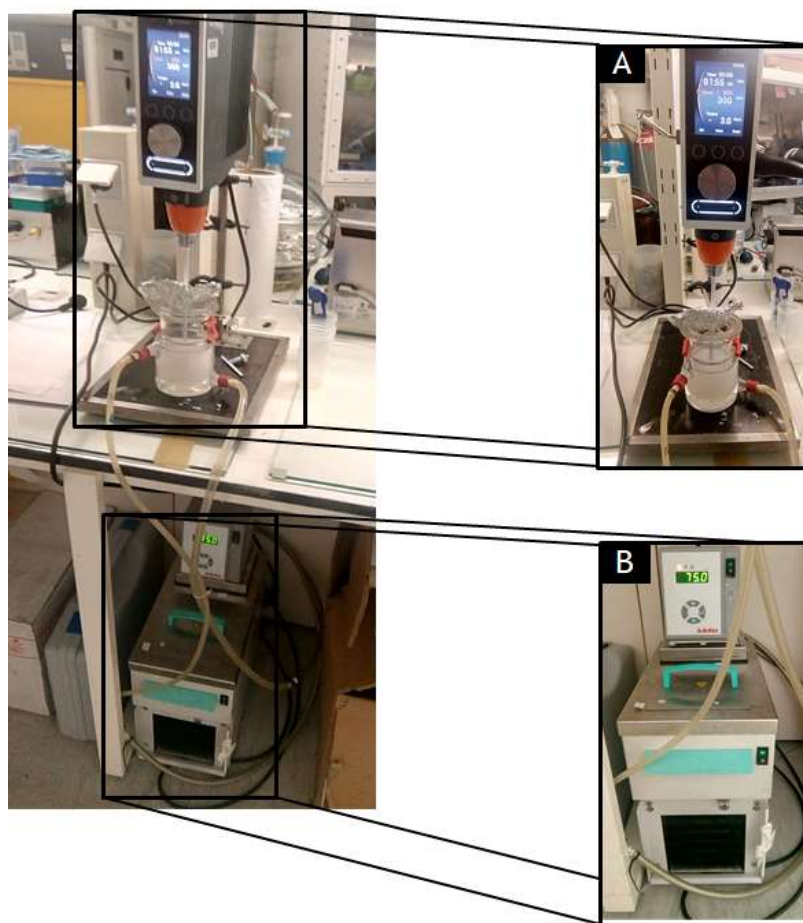


Figure 3-3: Ethanol vaporization on the SiO_2 paste preparation (A: mechanical stirrer used to help ethanol evaporation process; B: heating bath).

Two levels of ethanol evaporation were considered in the optimization of the SiO_2 pastes: i) ethanol evaporation until a suitable viscosity is reached, basically when the paste reached *ca.* 70 mL of solution in the evaporation bottle that corresponds to *ca.* 50 % of evaporation, hereafter called as evaporated paste and ii) without ethanol evaporation, hereafter non-evaporated paste.

The SiO_2 mesoporous film was applied by spin coating (Laurell[®] Technologies Corporation, Model WS-650HZB-23NPPB/UD3 - Figure 3-4A) onto $3 \times 1.2 \text{ cm}^2$ areas, over previously cleaned FTO glass samples. All depositions were performed at a $300 \text{ rpm}\cdot\text{s}^{-1}$ deposition acceleration. Deposited samples were then placed in an infrared oven (Termolab[®] Fornos Eléctricos, see Figure 3-4B) at $450 \text{ }^\circ\text{C}$ over 1 h to remove the solvent and promote better adhesion between the SiO_2 particles and the FTO glass surface.

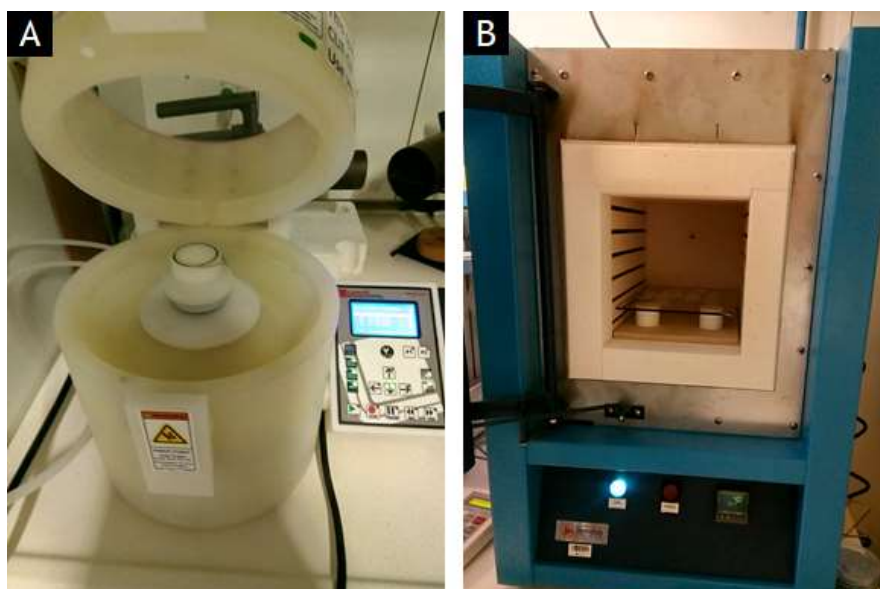


Figure 3-4: SiO_2 paste deposition and sintering (A: spin coater used for paste deposition; B: oven used for sintering the deposited SiO_2 paste on top of FTO-glass substrates).

3.3 Atomic Layer Deposition (ALD) technique

ALD is a technique to deposit thin films from gas phase precursors through saturated surface reactions. As described in Appendix B, alternated gas pulses into a heated reactor, separated by purging steps, constitute ALD operation principle. Each set of these four steps (first pulse of the precursor, purge, second pulse of oxidant reagent and final purge) corresponds to one cycle. In an ALD, cycles are continuously repeated until the desired film thickness. An inert carrier gas is also necessary to transport the first precursor vapors into the reaction chamber and to help purging it. Nitrogen is most often used for this purpose.[68] The general reaction mechanism is outlined in Figure 3-5.

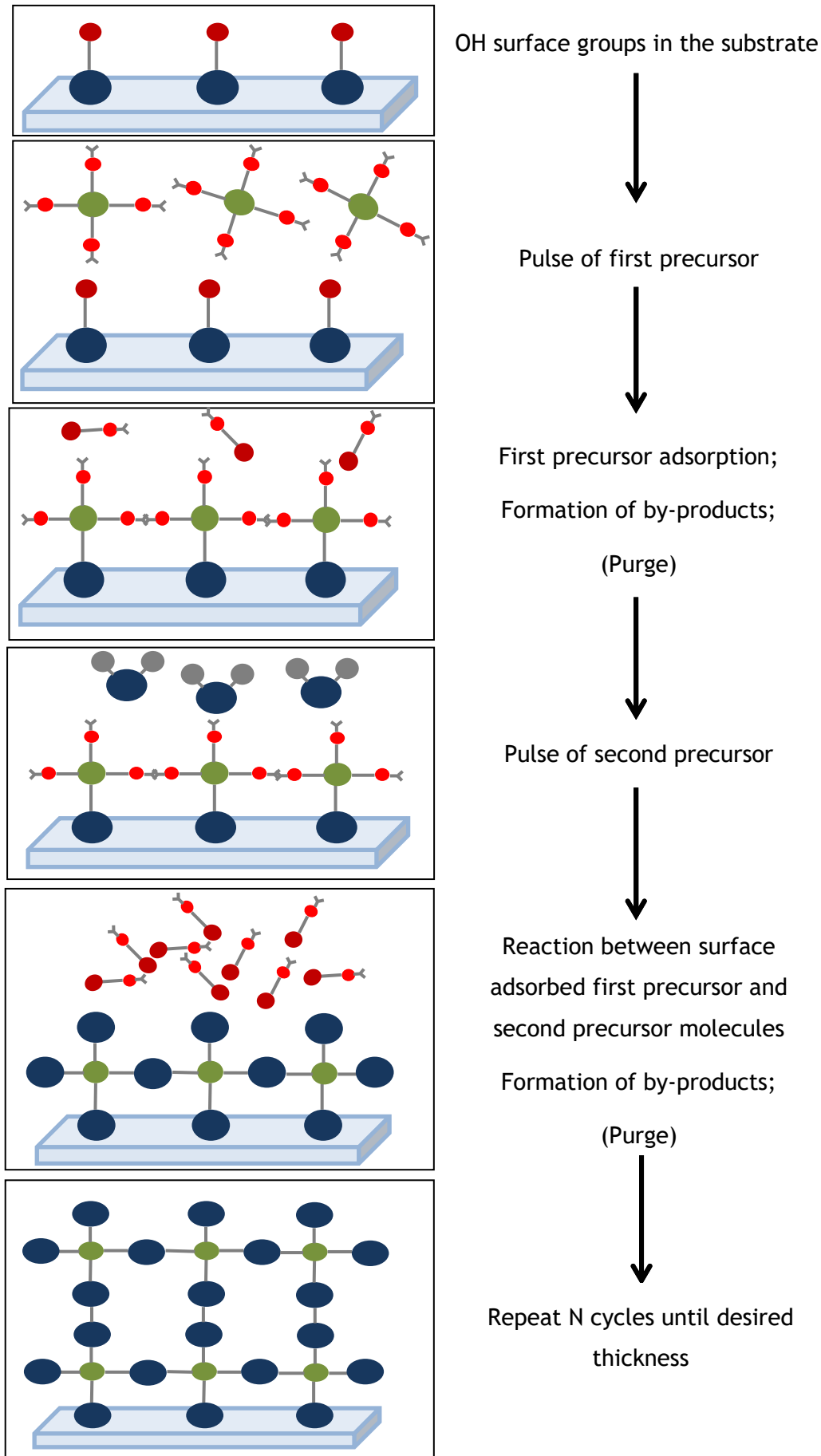


Figure 3-5: ALD general reaction mechanism.

Volatility, thermal stability, high chemisorbability and fast reaction time with surface groups are some characteristics that precursors must have to reach rapidly saturation point and promote a reasonable deposition rate.[69] High film thickness precision and homogeneity control, large area and batch capability, possibility to prepare multilayer structures and high reproducibility are some of the advantages of this deposition method. Each deposition process has a variable duration depending on the pulse times.[68]

In this work, ALD was used to deposit TiO_2 as a conductive thin film underlayer for the mesoporous host scaffold and hematite as an active photoelectrode. For this, a Beneq Oy thin film system equipped with a TFS 200 reactor was used. In TiO_2 film deposition, titanium (IV) isopropoxide ($\text{C}_{12}\text{H}_{28}\text{O}_4\text{Ti} \geq 97\%$, Sigma Aldrich®) was used as the first precursor and distilled water as an oxidant agent. The reaction mechanism was concretized by pulses, whose operation process and respective variables are presented in Appendix B. In hematite deposition, ferrocene ($\text{Fe}(\text{Cp})_2$ 99.5 %, Alfa Aesar®) was used as the first precursor and ozone (O_3) as an oxidant reagent. This gas must be produced on site because it cannot be stored or transported for long times and distances, due to high instability. Operation process variables and pulse times used are also detailed in Appendix B.

3.4 Spray pyrolysis technique

Spray pyrolysis is a technique applied to deposit a large variety of thin films and has been used most often in the glass industry and in solar cells fabrication. Many research works focused on solar energy use this technique, namely studies about hematite photoelectrodes.[70] This technique is cheap and allows to prepare reproducible films, that easily scalable, achieving a reasonable photoactivity.[27, 47] Spray pyrolysis involves spraying a metal salt solution over a substrate, where formed droplets at the surface undergo thermal decomposition. For this, temperature, precursor solution and existence of a pre-treatment or an underlayer strongly influences the final hematite film grown on FTO glasses.[70]

3.4.1 Spray pyrolysis setup and hematite deposition conditions

In the present work, the hematite films were prepared by an in-house assembled spray pyrolysis setup, which is equipped according to the scheme of Figure 3-6.[31] Dias *et al.*[31] optimized the deposition parameters that mostly contribute to obtain higher photocurrent of hematite thin films on top of TEOS (tetraethyl orthosilicate) pre-treated FTO glasses: i) sprayed volume of solution (v); ii) temperature of the glass substrate during the deposition (T); and iii) time gap between sprays (t). In this work, the conditions that allow to obtain an optimized hematite thin film of *ca.* 19 nm were: $v = 42$ mL, $T = 425$ °C and $t = 35$ s.[31] The operating principle of the system consists in injecting, through the spray nozzle (8), a solution of 10 mM of iron (III) acetylacetonate, $\text{Fe}(\text{AcAc})_3$, with the aid of a plastic syringe (2). The

injection is controlled by an automatic system (1) (Cronus programmable Sigma 2000 C, SMI-Labhut Ltd., UK). Compressed air (7) was also passed through the vaporization extremity (at *ca.* 2 bar) so that each jet of solution is sprayed in the form of aerosols. Each jet vaporizes 1 mL of solution at a flow rate of $12 \text{ mL}\cdot\text{min}^{-1}$, over a vaporization time of 5 s.

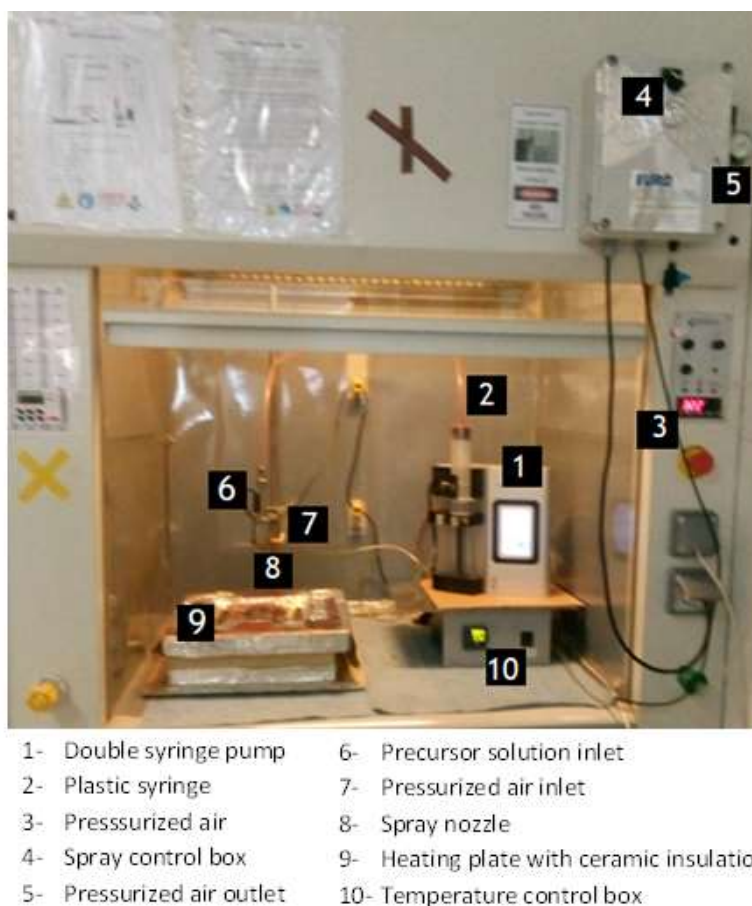


Figure 3-6: Scheme of the spray pyrolysis system.

Before deposition, the FTO glass samples are placed on the heating plate (9) and heated to the desired temperature of $425 \text{ }^\circ\text{C}$. After the spray deposition, the hematite samples were air-annealed at $550 \text{ }^\circ\text{C}$ for 30 min, and the heating plate was then cooled to room temperature.

A TEOS pre-treatment of FTO glasses was also performed to compare with the TiO_2 ALD underlayer, because TEOS underlayer is widely used in spray pyrolysis depositions allowing better $\alpha\text{-Fe}_2\text{O}_3$ film growth, reducing the interfacial strain between the FTO layer and the hematite crystals.[31] The FTO-glass substrates were heated at $450 \text{ }^\circ\text{C}$ and *ca.* 1.5 mL of a diluted TEOS solution (10 % volume in ethanol 99 %) were hand-sprayed with a glass atomizer onto the heated substrates. These samples were air-annealed over 1 h and then cooled to $425 \text{ }^\circ\text{C}$ to deposit the hematite film.[31] For each set of parameters tested, three samples were prepared to assess the reproducibility.

3.4.2 Electrodeposition of FeNiOOH co-catalyst

The FeNiOOH co-catalyst was deposited on hematite photoanodes by an anodic photoelectrochemical deposition method under 1 sun simulated illumination ($100 \text{ mW}\cdot\text{cm}^{-2}$). The solution composition for the deposition process was 16 mM nickel(II) acetate, 5 mM iron (III) sulfate hydrate and 0.1 M sodium sulfate in deionized water, as described elsewhere.[71] After an optimization process according to Tsyganok *et al.* the applied current density after the optimization process was chosen as $150 \mu\text{A}\cdot\text{cm}^{-2}$ and the deposition time was 20 min.

3.5 Samples characterization

3.5.1 Photoelectrochemical characterization

The photoelectrochemical characterization of the prepared photoelectrodes was performed using a PEC device known as “Cappuccino” cell (Figure 3-7A); this cell is made of polyetheretherketone (Erta PEEK®). For this purpose, the cell was filled with an electrolyte solution of 1 M KOH (25 °C, pH = 13.6), in which the photoelectrode was immersed. The surface area illuminated was *ca.* 0.528 cm^2 defined by an external mask. In this type of characterization, a standard three electrode configuration (Figure 3-7B) was used: i) the working electrode (WE) corresponding to the prepared hematite photoelectrodes, ii) a reference electrode (RE) of Ag/AgCl Sat. KCl (Metrohm, Switzerland), and iii) a counter-electrode (CE) of a 99.9 % pure platinum wire (Alfa Aesar®, Germany).

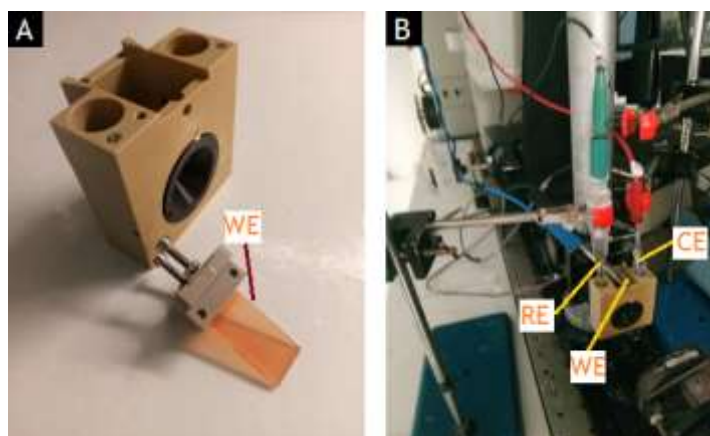


Figure 3-7: Electrochemical characterization setup (A: “Cappuccino” cell used in the samples characterization; B: setup assembled with three electrodes configuration).

The photocurrent-voltage (J - V) characteristic curves were obtained applying an external potential bias to the cell and measuring the generated photocurrent using a ZENNIUM device (Zahner Elektrik, Germany, see Figure 3-8B) controlled by Thales software (Thales Z 2.0). The measurements were performed at room temperature in dark and under 1-sun simulated sunlight, at a scan rate of $10 \text{ mV}\cdot\text{s}^{-1}$. A source power of the class B solar simulator (Figure 3-8A) equipped with a 150 W Xenon lamp (Oriel, Newport, USA) and an AM 1.5 G filter

with a lighting power of $100 \text{ mW}\cdot\text{cm}^{-2}$ was used (Figure 3-8C). The distance between “Cappuccino” cell and simulator was calibrated for these conditions using a c-Si photodiode.

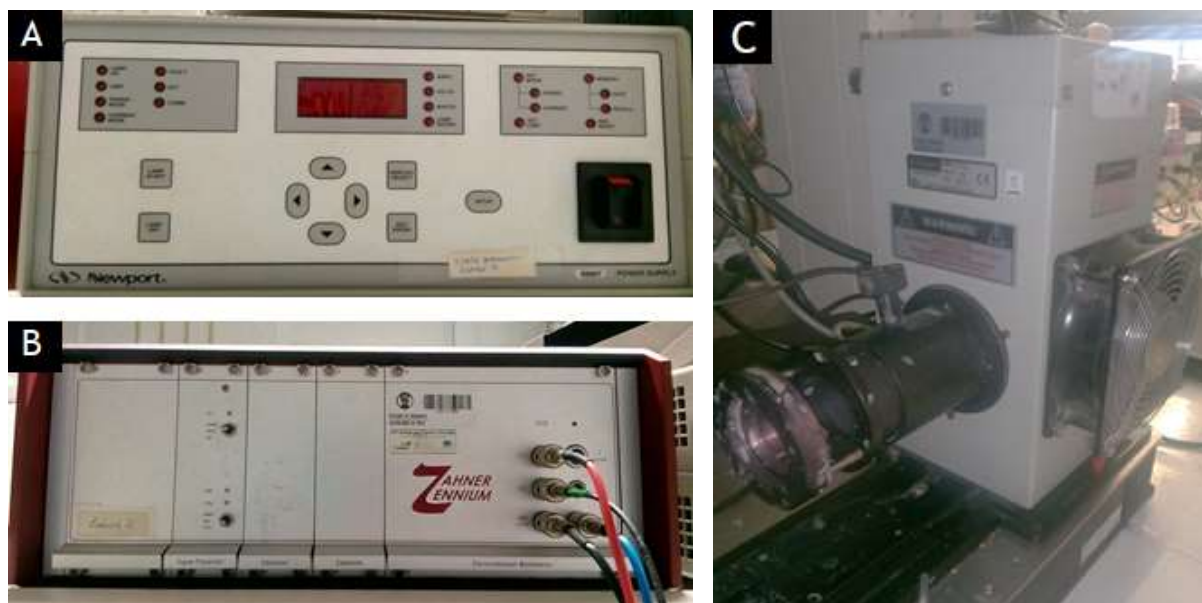


Figure 3-8: Devices used for PEC characterization (A: source power of the class B solar simulator; B: ZENNIUM workstation; C: solar simulator).

The applied potential bias was reported as a function of reversible hydrogen electrode (RHE), V_{RHE} , and the measured photocurrent (I_{measured}) were corrected for the photoelectrode effective illuminated area ($A_{\text{illuminated}}$), i.e. for photocurrent density (J_{photo}) according to equations 3.1 and 3.2, respectively.[5]

$$V_{\text{RHE}} = V_{\text{Ag/AgCl}} + V_{\text{Ag/AgCl vs SHE}}^0 + 0.059 \times \text{pH} \quad (3.1)$$

$$J_{\text{photo}} = \frac{I_{\text{measured}}}{A_{\text{illuminated}}} \quad (3.2)$$

$V_{\text{Ag/AgCl}}$ is the potential provided by ZENNIUM device to working electrode, $V_{\text{Ag/AgCl vs SHE}}^0$ is the potential of the Ag/AgCl reference electrode based on standard hydrogen potential (SHE), which corresponds to *ca.* 0.1976 V.[5]

Electrochemical impedance spectroscopy (EIS) analyses were performed for the frequency range of 0.1 Hz - 100 kHz and the amplitude 10 mV. The measurements were carried out in the dark and under 1-sun AM 1.5 G illumination conditions and the range of the applied potential was equal to that of the photocurrent measurements with a step of 50 mV. An appropriate electrical analog was then fitted to the EIS spectra using the ZView[®] software (Scribner Associates Inc.).

3.5.2 Morphology and films thickness characterization

The morphology of the prepared samples was characterized by a Phenom XL (PHENOM WORLD®) scanning electron microscope (SEM), equipped with an energy-dispersive X-ray spectrometer (EDS). To assess mesoporous template defects/cracks and overall homogeneity with varying synthesis parameters, top images were taken of all SiO₂ prepared samples. At least three different places of each sample were analysed.

Given the small thickness of the prepared films, SEM was also used to observe cross sections of the samples. Given that the SiO₂ templates are not conductive, low pressure conditions were used, which avoided charge accumulation effects but decrease overall image quality. To assess the morphology of the coated mesoporous films (with TiO₂ and α-Fe₂O₃) surface images were also taken. In some particular cases, which had very fine structures, a high-resolution SEM (FEQ Quanta ESEM 400FEG / EDAX Genesis X4M) was used at the Materials Center of the University of Porto (CEMUP). The acceleration voltage was 15 keV while an in-lens detector was employed with a working distance of about 10 mm. EDS measurements were made to qualitatively evaluate the composition of the samples. Thickness measurements were performed using ImageJ® software in three different SEM images, being considered the average thickness between there and respective measurements standard-deviation.

4 Results and Discussion

This chapter presents the results obtained in the developed work, from the optimization of the SiO₂ nanostructured film to the hematite semiconductor deposition and the electrochemical and morphological characterization of the prepared photoelectrodes.

4.1 SiO₂ film optimization

The main goal of SiO₂ film optimization was to obtain a mesoporous film with a thickness around 400 - 500 nm, which is the suitable hematite thickness for complete light absorption.[27] This was an ambitious task as mesoporous SiO₂ templates are typically thicker (> 3 μm) to avoid cracking. To obtain homogeneous and thin templates, the procedure needed to be optimized.

The optimization of SiO₂ templates was performed in two stages. The first was a stage of preliminary tests, where it was possible to understand the possible paste deposition conditions and the results that could be obtained. This step was crucial to understand which factors could be varied and could have influence on the film quality obtained on the FTO glass substrate as well as its thickness. Knowing the range of conditions to be used in the optimization of the film, a second stage was started in which the films were deposited with variable conditions, allowing to choose the optimal SiO₂ template.

4.1.1 Preliminary tests

For the deposition of the mesoporous SiO₂ template on the substrates using the spin coater, it was necessary to place a small portion of the paste on the substrate and spreading it as evenly as possible. Provided the high viscosity of the evaporated paste, Pasteur pipettes, cut at the extremity to have a larger opening, were used to spread the evaporated paste homogeneously on the substrate, prior to spin coating. Initial tests were done with particles B, due to stock limitations. Deposition speeds between 1000 rpm and 5000 rpm, at 60 s, were used in the initial tests. In these conditions, the results were unfavorable: SEM analysis revealed a cracked surface and very poor adhesion of the SiO₂ template to the FTO glass (Figure 4-1 A and B). Given the low mechanical stability of the template, confident cross section views were not possible although thickness was as large as 31.4 μm - Figure 4-1 C.

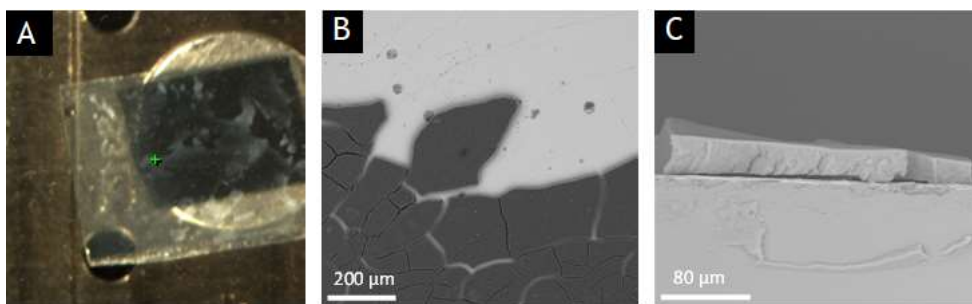


Figure 4-1: Sample with film deposited using evaporated paste (A: surface photograph; B: surface view using SEM, 300 x; C: Cross-section view, 890 x).

Provided that the initial spreading of the paste on the FTO glass was not as regular as desired, dilution of the paste with terpineol was one of the ways found to promote a better suction of the paste with the Pasteur pipette and to improve its spread before deposition. This dilution yielded better results in terms of achieved homogeneity in the film's surface after deposition and sintering. Table 4-1 presents different volumes of terpineol added, deposition speeds and deposition times programmed in the spin coater during the preliminary deposition tests. From cleaning glass substrates to SEM/EDS characterization, the spent time on each sample was over *ca.* 6 days; therefore, for each condition, only one sample was made but several places on each sample were analyzed. For an intermediate condition (5000 rpm of deposition speed, at 60, 90 and 120 s), three samples were prepared to assess the reproducibility.

Table 4-1: Preliminary tests (volume of terpineol added and deposition conditions).

Volume of terpineol added to evaporated paste	Deposition acceleration	Deposition speeds	Deposition times	
(mL)	(rpm/s)	(rpm)	(s)	
3 and 4	300	4000	90	
			60	
		5000	90	
			120	
		6000	90	

The influence of deposition time was tested and the resulting thicknesses of deposited films are presented in Figure 4-2, for paste type B at 5000 rpm. A decreasing thickness trend is observed with increasing deposition time, as expected. The thickness variation is not significant with deposition time and the dilution factor is clearly more determinant in the

final thickness of the film. An exception was observed at 120 s for 3 mL added terpineol, which is justified as an experimental error. Given the preliminary nature of these tests, this particular experiment was not repeated.

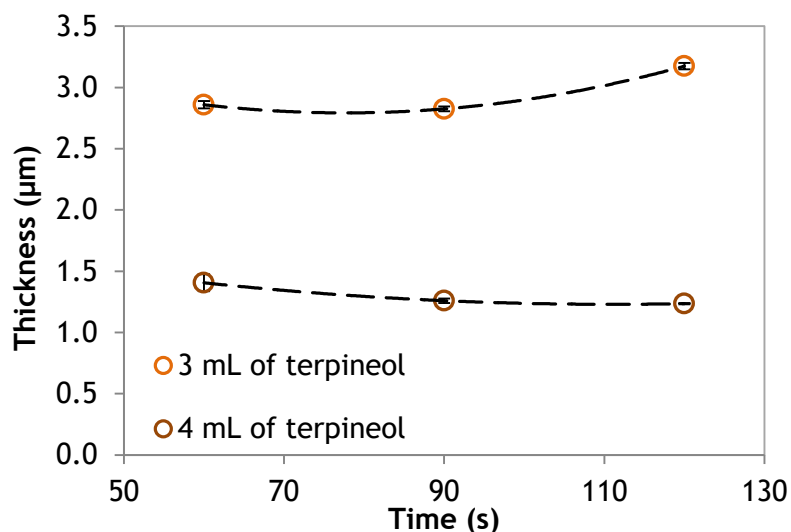


Figure 4-2: SiO₂ mesoporous film thickness variation as a function of the spin coating deposition time (at 5000 rpm speed) according different dilutions of terpineol: 3 mL (○) and 4 mL (○). Lines represented are just a guide to the eye.

The influence of the deposition speed (rpm) was studied by fixing the deposition time at 90 s - Figure 4-3. Once again, the dilution with terpineol has a major effect on the final thickness. In both dilutions, a well-defined film thickness decreasing trend occurs as the deposition speeds increase.

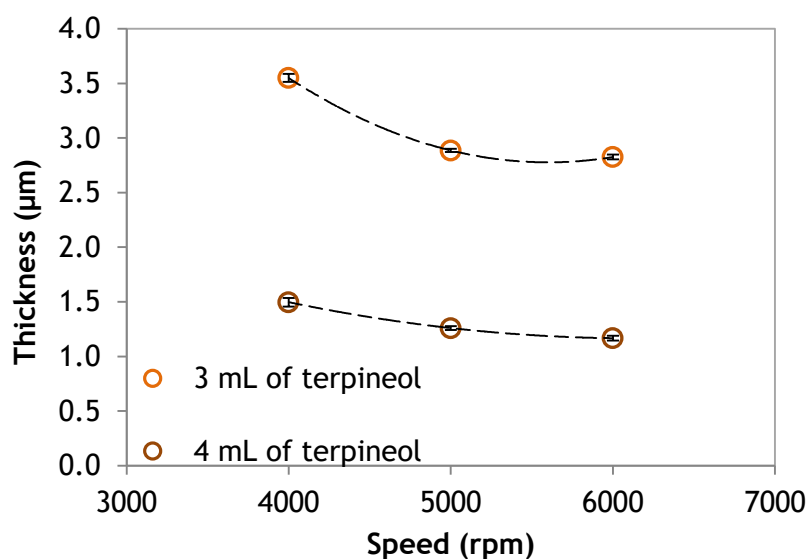


Figure 4-3: SiO₂ mesoporous film thickness variation as a function of the spin coating deposition speed (at 90 s deposition time) according different dilutions of terpineol: 3 mL (○) and 4 mL (○). Lines represented are just a guide to the eye.

Combining Figure 4-2 and 4-3, it appears that with a higher dilution (in this case adding 4 mL of terpineol) the spin coater parameters do not change significantly the final thickness of the film, although it is clear that higher speeds and longer times tend to decrease it. Since it was of interest preliminary tests were conducted to identify the best range of conditions for this purpose. The deposition speed was limited by the equipment requirement of 6000 rpm, thus only the deposition times were varied to study how these influence the film thickness. Given the clear importance of the paste dilution, two additional conditions were tested: a) a diluted paste with terpineol, prepared as described in experimental section (evaporated paste); and b) an undiluted paste, prepared without ethanol evaporation (non-evaporated paste). These conditions are presented in Table 4-2. Figure 4-4 shows a slightly film thickness decrease with the increase of deposition time to double, *i.e.*, the thickness tends to stabilize from 120 s of deposition onwards.

Table 4-2: Additional preliminary tests conditions.

Paste conditions	Deposition speed	Deposition times
	(rpm)	(s)
Non-evaporated and evaporated pastes diluted with 4 mL of terpineol	6000	90
		120
		180
		240

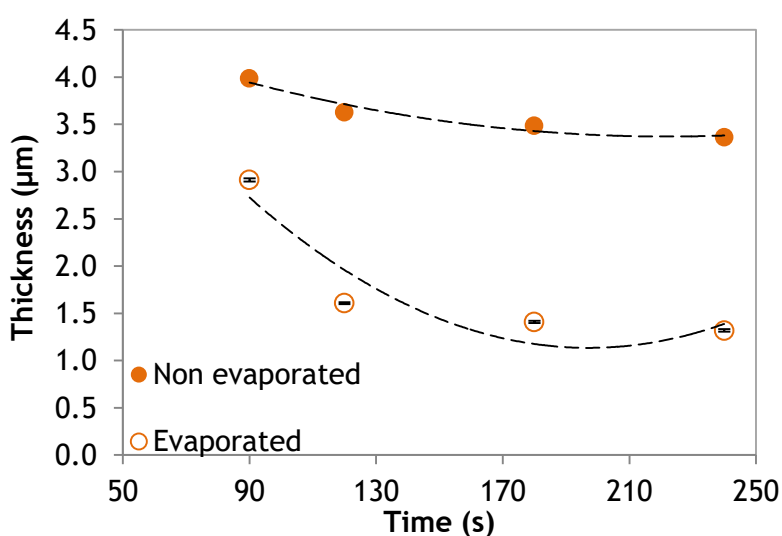


Figure 4-4: SiO_2 mesoporous film thickness variation as a function of the deposition time under additional preliminary tests conditions (at 6000 rpm spin coating speed) for non-evaporated (●) and evaporated (○) pastes. Lines represented are just a guide to the eye.

Another relevant aspect, which was verified by the graph in Figure 4-4, is the fact that the film prepared with the non-evaporated paste has higher thickness values than the film prepared with the evaporated paste diluted with terpineol. The lowest thickness values were obtained with a deposition time of 240 s in both cases, showing a homogeneous film throughout the surface, although the evaporated paste shows a smoother surface with fewer defects, as can be seen in the Figure 4-5.

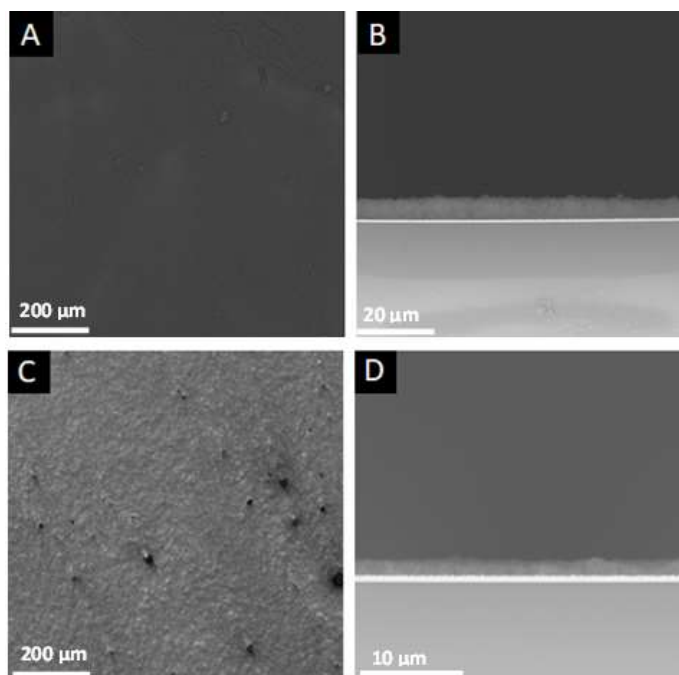


Figure 4-5: SEM images of the SiO_2 mesoporous films prepared using non-evaporated paste (A: surface view using SEM, 300 x; B: Cross-section view, 2900 x) and evaporated diluted paste (C: surface view using SEM, 300 x; D: Cross-section view, 8500 x).

After completing this set of preliminary tests, it was possible to conclude that the dilution of paste with terpineol allows to effectively reduce the thickness of the mesoporous SiO_2 film. Taking this into account, paste dilution with terpineol was a factor varied in the following optimization step, for finding a film thickness lower than 500 nm and as homogeneous as possible.

4.1.2 Film optimization

Based on the considerations obtained in the preliminary tests, several conditions were studied to optimize the mesoporous SiO_2 film, but now using both the particles A and B. Two different pastes, with a specific surface area (measured by BET method, Appendix A) of $87.8 \text{ m}^2 \cdot \text{g}^{-1}$ and $141.6 \text{ m}^2 \cdot \text{g}^{-1}$, were prepared; both pastes were collected with different phases of ethanol evaporation to obtain different viscosities, as described in experimental section. The two pastes were diluted with different volumes of terpineol and the films were deposited at different times (90 s, 180 s and 240 s), with deposition speed fixed at 6000 rpm, as

presented in Table 4-3. The film thickness variation as a function of time was studied for all dilutions - Figure 4-6.

Table 4-3: Tests for SiO₂ mesoporous film optimization.

Type of particles	Paste conditions used	Deposition speed	Paste dilutions with terpineol	Deposition times
		(rpm)	(mL)	(s)
A and B	Non-evaporated and Evaporated	6000	4, 8 and 16	90
				180
				240

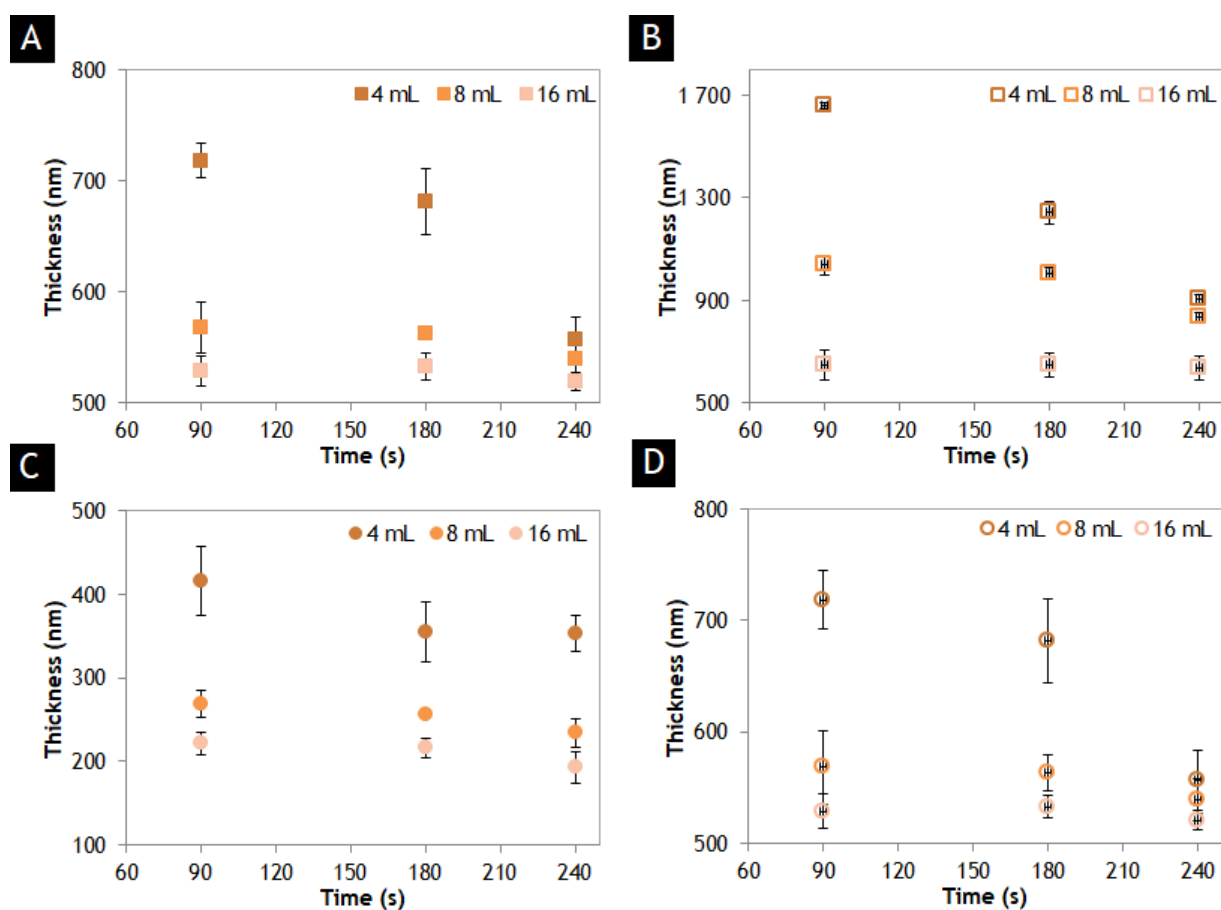


Figure 4-6: SiO₂ mesoporous film thickness variation as a function of the deposition time (at 6000 rpm spin coating speed). A: particles A, non-evaporated paste diluted with 4 mL (▪), 8 mL (▪) and 16 mL (▪); B: particles A evaporated paste diluted with 4 mL (□), 8 mL (□) and 16 mL (□); C: particles B, non-evaporated paste diluted with 4 mL (●), 8 mL (●) and 16 mL (●); D: particles B evaporated paste diluted with 4 mL (○), 8 mL (○) and 16 mL (○).

Figure 4-6 shows similar conclusions to the ones obtained in the preliminary tests, *i.e.* a decrease in the thickness of the mesoporous film with the deposition time was observed. It should be noted that the films deposited with the particles B presented smaller thicknesses compared to the films deposited with the particles A. The film thickness of the non-evaporated paste of the particles A (Figure 4-6A) shows a range of 520 nm and 718 nm while the film with the particles B presents thicknesses between 193 nm and 416 nm (Figure 4-6B). The same scenario happens for the films prepared with evaporated paste: in the particles A the lower thickness reached was 636 nm (Figure 4-6C) while in the particles B the lower thickness obtained was 243 nm (Figure 4-6D).

In both cases it is found that films prepared with non-evaporated paste have lower thicknesses than those prepared with the evaporated paste; the deposition time of 240 s allows to obtain the lowest thicknesses for all dilutions. Moreover, it was noticed that the volume of terpineol used in the dilutions is the parameter that most influenced the decrease of film thickness. Figure 4-7 displays the relationship between the film thickness and the volume of terpineol used in each of the dilutions, fixing deposition time at 240 s and speed at 6000 rpm.

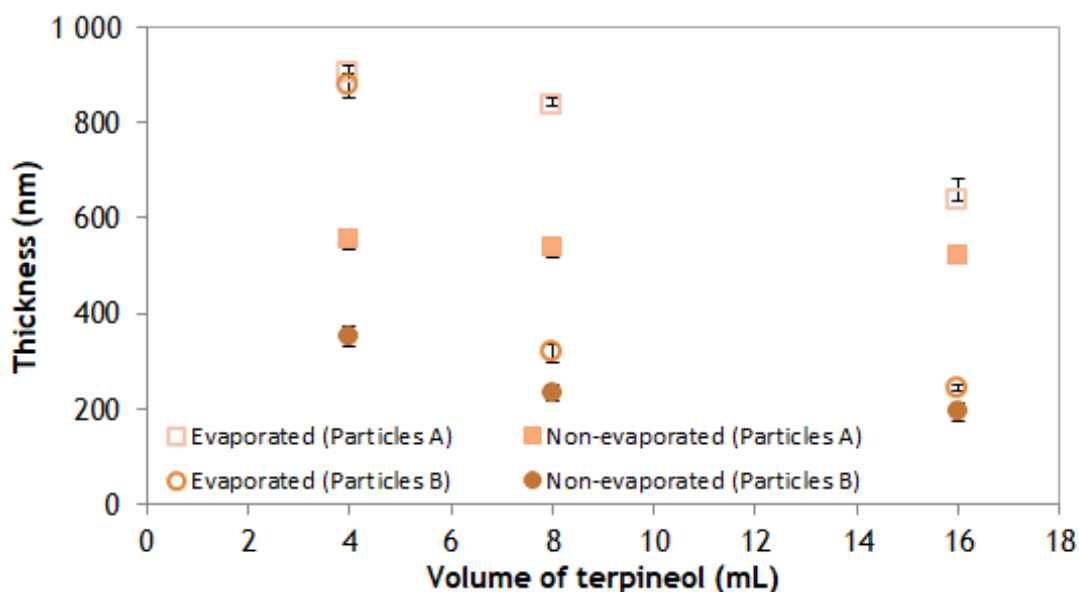


Figure 4-7: SiO_2 mesoporous film thickness variation as a function of the terpineol volume used in the paste dilutions (at 6000 rpm spin coating speed and at 240 s deposition time) for the evaporated paste with particles A (\square); non-evaporated paste with particles A (\blacksquare); evaporated paste with particles B (\circ); and non-evaporated paste with particles B (\bullet).

The non-evaporated paste with particles B and diluted with 16 mL of terpineol presented the lowest value of the thickness of around 193 ± 19 nm. Figure 4-8 shows a cross-section SEM image of this optimized SiO_2 mesoporous film deposited over the FTO glass substrate, showing a good homogeneity and uniformity.

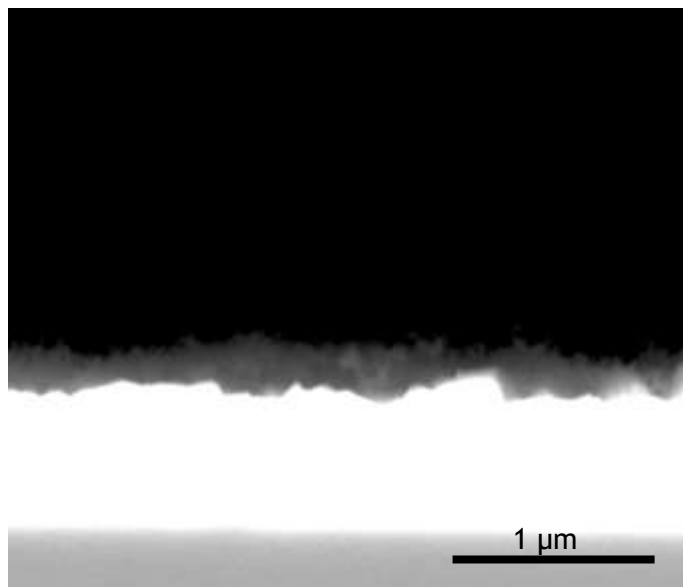


Figure 4-8: Cross-section SEM image (75000 x) of the SiO_2 mesoporous film prepared with particles B and deposited using the optimized conditions mentioned above.

4.2 Hematite thin films preparation

4.2.1 Deposition of hematite by ALD

The main goal of this work was to perform the deposition of hematite by ALD over the mesoporous SiO_2 film coated with a TiO_2 sublayer. Firstly, deposition attempts were performed following the procedure indicated in Appendix B (preliminary tests), as reported elsewhere.[72] This procedure used ferrocene as the first precursor and ozone as the second precursor. However, all depositions tested were not suitable for the intended purposes, e.g. in some depositions it was not possible to see the hematite film on the glass substrates and in other cases the film was very thin and not homogeneous over the FTO glass substrates, as shown in Figure 4-9.



Figure 4-9: Glass substrates after hematite film deposition using ALD technique.

After several depositions, the poor quality of the hematite films deposited led to believe that there were problems in the reactive process that could be related to the procedure. Essentially, two variables could change during the deposition and could influence the behaviour of the precursors in the reactive process: the pulse time and temperature.

Pulse time has a clear influence on the deposition process and, particularly, on the growth form of the film.[68] The procedure followed was optimized for a different ALD equipment, thus it was considered that possibly the pulse times could not be suitable for the ALD available at LEPABE laboratory. In addition, in the present work, hematite depositions were made over a mesoporous SiO₂ film, whereby a longer deposition time may be required to improve film impregnation. Thus, it was decided to test a new deposition in which the pulse time variable was increased in both precursors (second test values, Appendix B). By increasing this variable, a longer contact time between the precursor and the layer in which it will be adsorbed is provided, thus increasing the possibility of forming the film more homogeneously throughout the surface. However, the alternative followed did not result in improvements in the deposition process.

Still related to the pulse times and according to literature, it was considered that the deposition of hematite with micropulses could be the suitable solution to the problem. The use of this strategy has two advantages comparing to single pulse technique. One of them is related to ferrocene pressure: when micropulses are applied, the precursor is maintained at high pressure for a longer time, allowing to increase chemisorption, whereas in a normal process pressure drops quickly after the pulse. This could be the possible impediment for the reaction process occurring properly. The second cause is related to the fact that the precursor enters the reaction chamber with some disturbance, travelling the surface of the samples in the form of a periodic wave.[73] In a deposition of this nature, this effect may interfere with the reaction process. However, it is possible to attenuate it using a micropulse deposition. An ALD deposition by micropulses has exactly the same principle as a normal deposition, except that the pulse (in this case of the first precursor, ferrocene) would be done in shorter times but repeatedly. This technique was already used and reported in the literature, also using a Beneq ALD device. With this technique, the precursor temperature variation was also tested; as mentioned in detail in Appendix B, precursor temperature influences the deposition process. One of the problems that could be occurring in the process would be the existence of a high thermal gradient in the container of the hot precursor. Sometimes the temperature sensor detects that the container wall is at the desired temperature in the process, however, inside the tank the temperature may be lower. This type of phenomena is largely dependent on the nature of the precursor, which may present more or less resistance to heat transfer. Having these concerns in consideration, a new

deposition was tested (third test values, Appendix B) where both alternatives were combined but, again, culminated in failure. Also taking into account the temperature problem, the use of small glass beads inserted in the ferrocene was also tested with the function of improving the heat transfer to the container innermost part, allowing to homogenize the temperature throughout the precursor. This is a solution that appears in the literature for problems of high thermal gradients in reactors.[74] Precursor and glass beads were then placed in the container in alternating layers (fourth test values, Appendix B). In this trial, intermediate pulse times were used in relation to the initially established parameters. Despite the attempt, the result failed again.

At this point in the work, it was concluded that a technical expertise intervention is mandatory for the equipment that could clarify if there is actually a leak or a problem of another nature that could be affecting the hematite deposition processes. Considering the time constraints to perform the present work, it was decided to use other technique for depositing hematite thin films on top of the prepared SiO_2 nanostructured template.

4.2.2 Deposition of hematite by spray pyrolysis

Spray pyrolysis was the alternative technique to ALD available in the laboratory for depositing hematite photoelectrodes that is suitable for the objective of the proposed work. The proposed nanostructure involves the deposition of a thin layer of TiO_2 on top of the SiO_2 mesoporous film to promote a better collection of the generated electrons from hematite film to the FTO. Since there is no ideas about the diffusion capacity of the TiO_2 underlayer in the synthesized SiO_2 mesoporous film, it was decided to use the lowest film thickness (193 nm) than the literature proposal (between 400 and 500 nm) in order to facilitate impregnation up to the interface between the mesoporous film and the FTO. Also, using spray pyrolysis, it is expected that most of the material will be deposited on the surface and less inside the pores, making the charge transfer path longer. This was the second reason why a smaller thickness was selected for testing.

To test the compatibility of this underlayer, flat and thin hematite (without mesoporous template) films were made. Then, the hematite thin film was deposited using the spray pyrolysis technique; the research group where the present work was performed assembled and optimized a spray pyrolysis setup for depositing hematite films. This optimization was made for hematite films deposited on top of TEOS pre-treated FTO glasses, which allows the deposition of a very thin layer of SiO_x . [31] Herein, the deposition conditions were also optimized for the prepared SiO_2 mesoporous film coated with the TiO_2 thin layer, namely evaluating the dependence of thickness as a function of the volume deposited and the performance obtained by J - V curves.

4.2.3 TEOS pre-treatment vs. TiO₂ conductive underlayer

The first step in the preparation of the hematite photoelectrodes started with the performance comparison between the use of a TEOS monolayer (TEOS-H) and the use of a TiO₂ thin underlayer (TiO₂-H), both deposited directly on the FTO layer; these samples were coded as TEOS-H and TiO₂-H, respectively. For the TEOS deposition a 5 mL diluted TEOS solution was hand sprayed using a glass atomizer on the FTO glass substrates at a temperature of 450 °C, whereas the TiO₂ layer of ca. 3 nm was deposited by ALD; both recipes were described in detail in Chapter 3. The TEOS and TiO₂ thin underlayers were then sintered at 450 °C for 1h before hematite deposition. Figure 4-10 shows the *J-V* characteristic curves, obtained in the dark and under 1-sun AM 1.5G illumination, for the two cases under study.

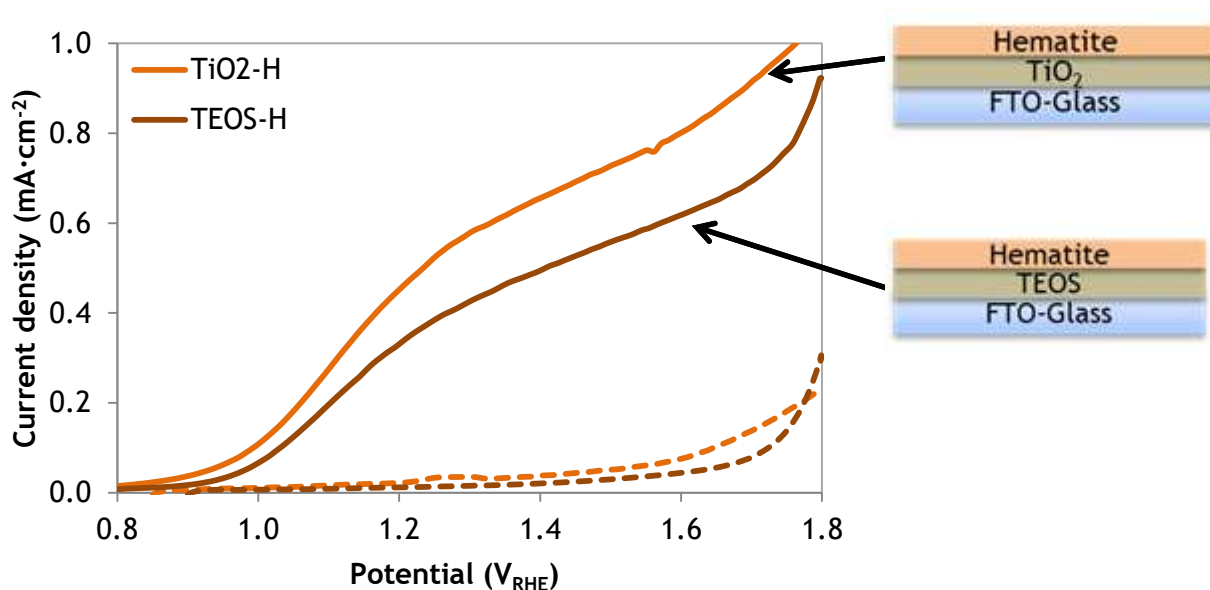


Figure 4-10: *J-V* characteristic curves for the hematite photoelectrodes deposited on top of TiO₂ (TiO₂-H) and TEOS (TEOS-H) underlayers, in the dark (dashed lines) and under simulated solar illumination conditions (solid lines).

For both TEOS-H and TiO₂-H samples under dark conditions, the current density rises steeply for a potential higher than 1.60 V_{RHE}, the so-called dark current that indicates the electrochemical water oxidation onset potential - Figure 4-10. Under sunlight conditions, the use of a TiO₂ conductive underlayer showed an earlier photocurrent onset potential (which is the point where the current density rises steeply under light conditions) at ca. 0.95 V_{RHE} compared to 0.90 V_{RHE} for the TEOS-H sample. TiO₂-H also exhibited higher photocurrent densities than TEOS-H, *i.e.* 0.69 mA·cm⁻² and 0.53 mA·cm⁻² at an applied bias potential of 1.45 V_{RHE}, respectively. In fact, the conductive properties of the TiO₂ underlayer are more effective in improving the performance of a hematite photoelectrode than the TEOS underlayer. This can be explained because TiO₂ underlayer can play two roles in hematite films acting as a Ti doping source and as a functional blocking layer, whereas TEOS underlayer

mainly influences the hematite film growth, reducing the interfacial tension between FTO and hematite. A recent report showed this bifunctional role of TiO_2 resulting in improved charge transfer and separation efficiency in hematite films.[31, 75]

To understand how hematite films grow on top of different underlayers, their thickness was estimated by the UV-Vis spectrophotometric method. The method used to estimate the thickness is detailed in Appendix C. The hematite film thicknesses obtained were 43.3 nm for the TEOS-H sample and 38.3 nm for the TiO_2 -H sample. The film growth on top of TEOS originated a thicker film. Provided that TiO_2 performance was higher than TEOS, and that it is possible to conformably coat a mesoporous template with TiO_2 using ALD, this layer was selected as conductive underlayer for the remaining studies.

4.2.4 Hematite film optimization

As a starting point, hematite films were prepared by spraying 42 mL volume of $\text{Fe}(\text{AcAc})_3$ precursor solution, a condition optimized elsewhere.[31] The semiconductor deposition was performed on top of the optimized SiO_2 mesoporous film, with *ca.* 193 nm thickness templates coated with a thin layer of TiO_2 , following the operating conditions of Chapter 3. Figure 4-11 shows the characteristic curves (dark and light response) obtained under these conditions.

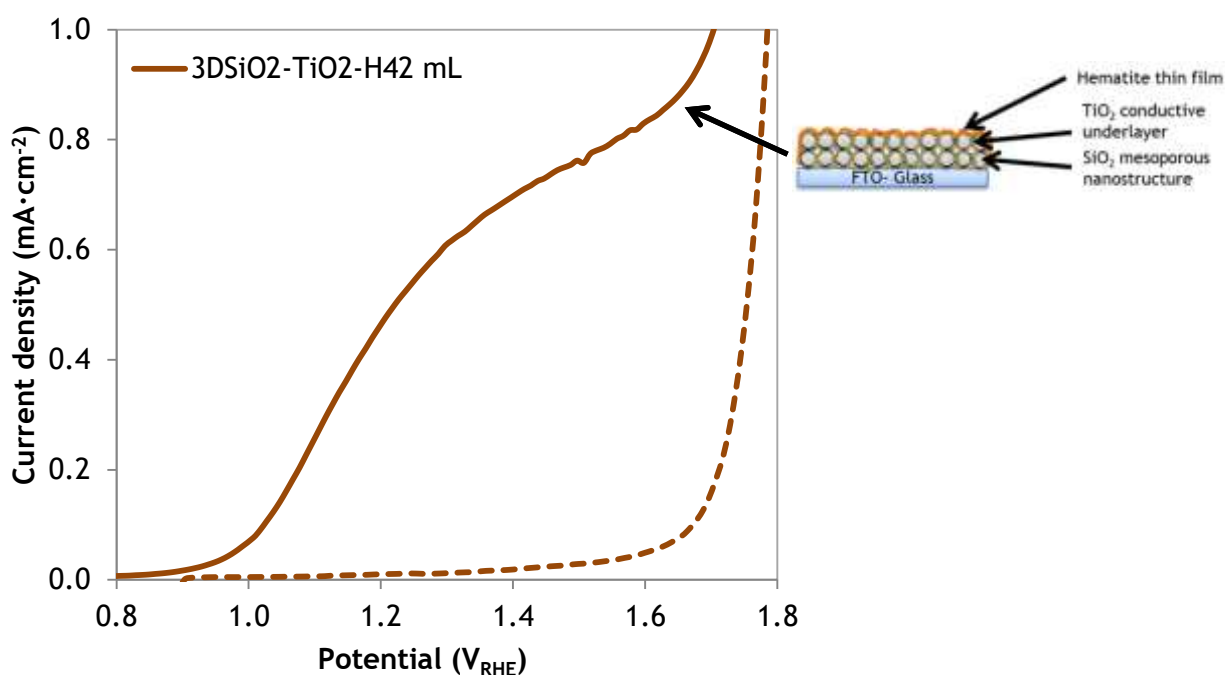


Figure 4-11: J-V characteristic curves for the samples with SiO_2 mesoporous film coated with a TiO_2 conductive layer for 42 mL $\text{Fe}(\text{AcAc})_3$ volume deposited, in the dark (dashed lines) and under simulated solar illumination conditions (solid lines).

From Figure 4-11, a current density of *ca.* $0.73 \text{ mA}\cdot\text{cm}^{-2}$ at $1.45 \text{ V}_{\text{RHE}}$ was obtained for hematite film deposited on top of the optimized SiO_2 mesoporous film coated with a TiO_2 conductive underlayer, coded as 3DSiO2-TiO2-H42. Despite the complex structure of the mesoporous SiO_2 template, the performance of this sample matches the thin film's (TiO_2 -H sample). This can be justified because the procedure followed for hematite films were optimized for depositions on top of TEOS pre-treated FTO glass[31], while in the present work the deposition was done over a mesoporous SiO_2 nanostructure. This means that, in the case of the present work, the electrons have to go through the interstices between the nanoparticles of SiO_2 , through the deposition TiO_2 layer, until reaching the conductive layer of the glass substrate and, finally, the electric contact to measure the current in function of the applied potential. Nevertheless, the performance as suffered no apparent loss indicating that the charge collection is properly ensured. Therefore, the deposition parameters used may not be suitable to be depositions on top of a nanostructure as the one developed. With this in mind, the next step aimed at optimizing the volume of precursor solution to be deposited. Volumes above (60 mL) and below (15 mL and 30 mL) of the volume initially tested were deposited and the performance hematite samples prepared were evaluated. Figure 4-12 shows the J - V characteristic curves obtained for each of these volumes.

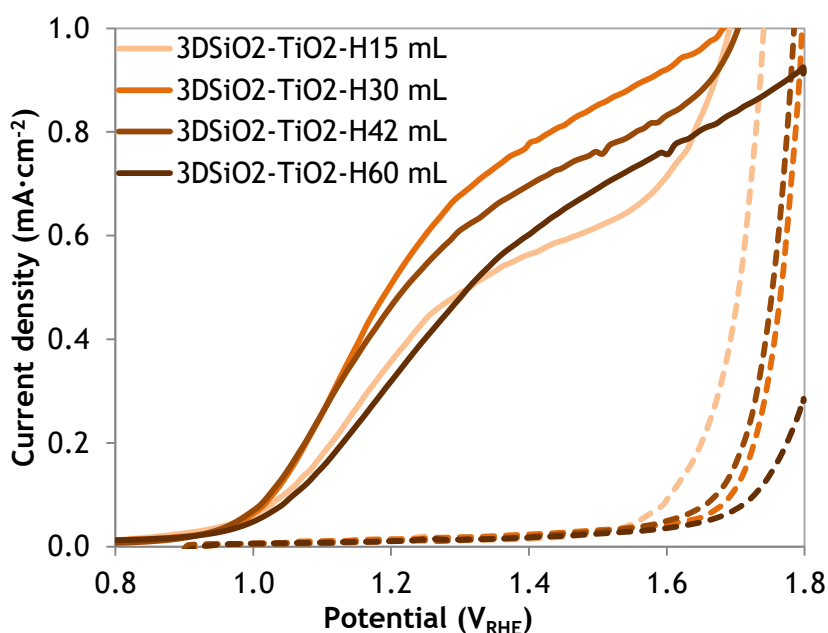


Figure 4-12: J - V characteristic curves for the hematite samples deposited on top of SiO_2 mesoporous film coated with a TiO_2 conductive layer (3DSiO2-TiO2-H) for different $\text{Fe}(\text{AcAc})_3$ volumes deposited (15 mL, 30 mL, 42 mL and 60 mL).

After obtaining the J - V curve characteristics, it was possible to plot the current densities obtained at $1.45 V_{RHE}$ as a function of the volume of $Fe(AcAc)_3$ solution deposited - Figure 4-13, which clearly peaks for a deposited volume of 30 mL, corresponding to the optimal condition for the SiO_2 template prepared. Therefore, this sample reached *ca.* $0.81 \text{ mA}\cdot\text{cm}^{-2}$ at $1.45 V_{RHE}$, which corresponds to an improvement of *ca.* 9.8 % compared to sample with 42 mL. As expected, the volume of deposited precursor solution had a significant influence on the photoelectrode performance. It is also important to note that the decrease in hematite film thickness also results in loss of optical absorption of light in the photoanode but decreases charge recombination. Future work should involve a careful optimization of the thickness of the template and hematite film to achieve the best equilibrium between light absorption, recombination and charge transfer.

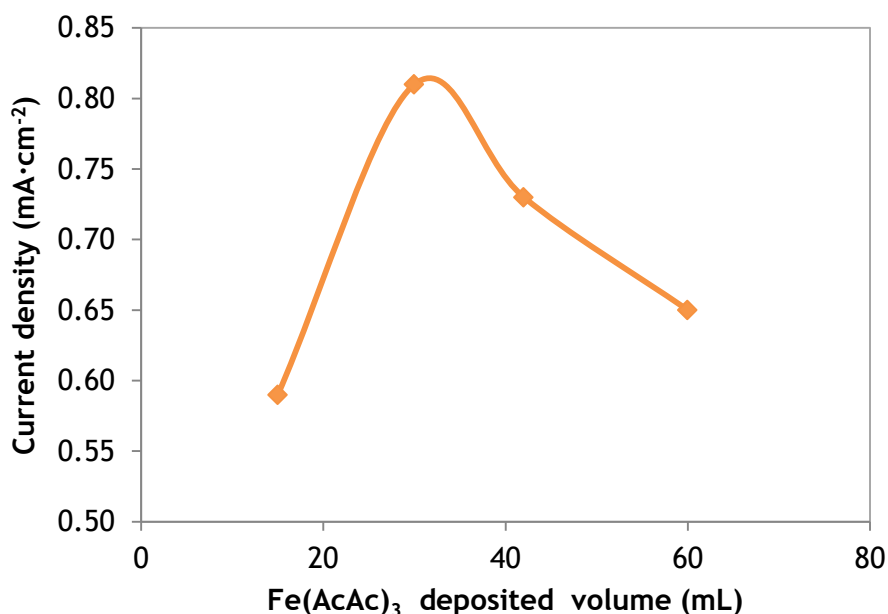


Figure 4-13: Current density values obtained at $1.45 V_{RHE}$ as a function of deposited volume for hematite samples deposited on top of SiO_2 mesoporous template coated with TiO_2 underlayer.

Figure 4-14A shows an SEM image of the surface sample, with enlargement of the hematite film growth shown in Figure 4-14B. EDS results presented in Figure 4-14C allowed to observe Sn, Si, Ti, and Fe elements in the sample, as expected.

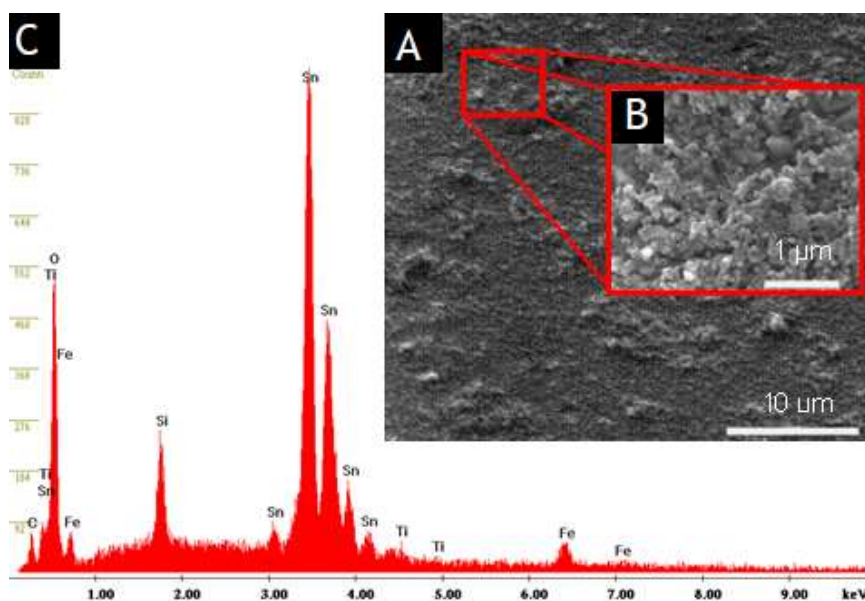


Figure 4-14: Optimal sample (A: SEM surface image; B: SEM image amplification with hematite film growth; C: EDS analysis).

The thickness of hematite film on top of the SiO_2 mesoporous template with a TiO_2 underlayer was also determined for samples deposited with a volume of 42 mL and 30 mL, being 39 nm and 31 nm, respectively. As expected, the use of a lower volume of solution leads to obtain a thinner thin, which justifies the observed improvement in the photocurrent results.

For the configuration under study with spray pyrolysis deposition, the performance can still be improved by surface treatments. The best way to do this is through the use of catalysts, whose role is to reduce the overpotential required in the photo-oxidation reactions, creating a cathodic shift in the external bias that is applied. One of the catalysts that, according to the literature, has shown success when applied in hematite photoelectrodes is FeNiOOH . [76] With this in mind, it was decided to study the effect of the application of this catalyst in the sample of 30 mL, hereafter called as $3\text{DSiO}_2\text{-TiO}_2\text{-H}$. Figure 4-15 summarizes the J - V characteristic curves of the main four types of hematite photoelectrodes under study: TEOS and hematite (TEOS-H), TiO_2 and hematite ($\text{TiO}_2\text{-H}$), mesoporous film of SiO_2 coated with TiO_2 and hematite ($3\text{DSiO}_2\text{-TiO}_2\text{-H}$), and mesoporous film of SiO_2 coated with TiO_2 and hematite activated with FeNiOOH as co-catalyst ($3\text{DSiO}_2\text{-TiO}_2\text{-H-FeNiOOH}$).

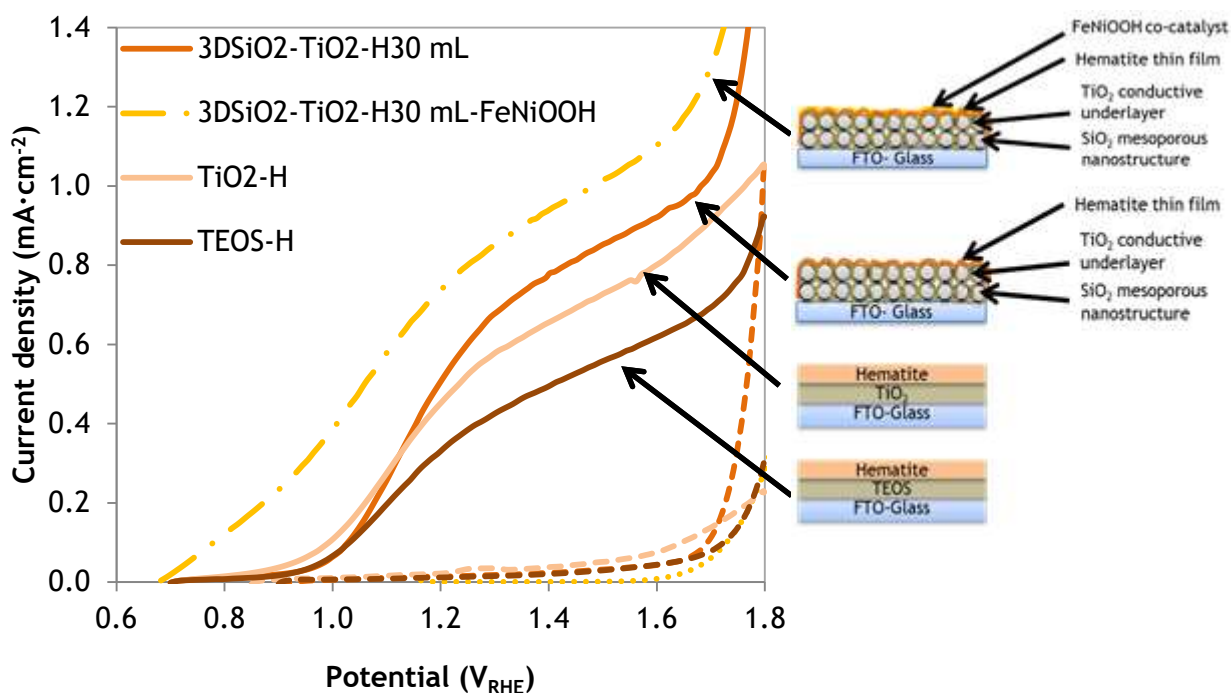


Figure 4-15: J-V characteristic curves for the samples with SiO_2 mesoporous film coated with a TiO_2 conductive layer for different $\text{Fe}(\text{AcAc})_3$ volumes deposited - 30 mL with catalyst (H30 mL-FeNiOOH) and 30 mL without catalyst (H30 mL).

The use of FeNiOOH as a co-catalyst allowed to achieve an improvement in the photoelectrode performance of ca. 17 %, showing a generated photocurrent value of ca. $0.98 \text{ mA}\cdot\text{cm}^{-2}$ at $1.45 V_{\text{RHE}}$. As expected, the onset potential was also shifted to lower potentials, i.e. from ca. $1.00 V_{\text{RHE}}$ to $0.70 V_{\text{RHE}}$.

However, comparing with the record values of the literature, the success of this result still falls short. Impregnation problems of the hematite film deposited by spray pyrolysis may be a problem, which could be overcome by using e.g. ALD. Another factor that could contribute to a better impregnation of hematite in the nanostructure could be the use of a SiO_2 film of even smaller thickness or using particles with even larger pores. It is important to take into account that the use of particles with larger pores implies the reduction of the surface area of the nanostructure, which should result in a decrease of the hematite photoelectrode performance, so it would be necessary to find a middle ground between these two factors.

4.2.5 EIS analysis

For obtaining more information about the performance of the prepared hematite photoelectrodes, EIS tests were performed. The tests were performed on the four types of samples under study: TEOS-H, TiO_2 -H, 3DSiO₂-TiO₂-H and 3DSiO₂-TiO₂-H-FeNiOOH. All EIS

measurements were performed using a three-electrode configuration (in the dark and under 1-sun illumination conditions) at the same potential range of the J - V curves (Figure 4-15).

Figure 4-16A shows representative graph with Nyquist curves obtained in the dark at a potential of 1.20 V_{RHE} . Under the mentioned conditions, only a semicircle in the impedance spectrum was detected in all analyzed photoelectrodes. Another aspect that could be observed was the increase of the semicircles, according to the trend: 3DSiO₂-TiO₂-H-FeNiOOH < 3DSiO₂-TiO₂-H < TiO₂-H < TEOS-H. This increase occurred at low frequencies, *i.e.*, high impedances. Figure 4-16B presents a scheme analogous of the electrical circuit used to fit the impedance data, called the Randles circuit. The scheme consists of a resistor in series (R_{Series}), constituted only by a resistor-capacitor element (RC), on which was the resistance to the semiconductor/electrolyte charge transfer (R_{CT}) in parallel with the capacitance, C_{Bulk} .

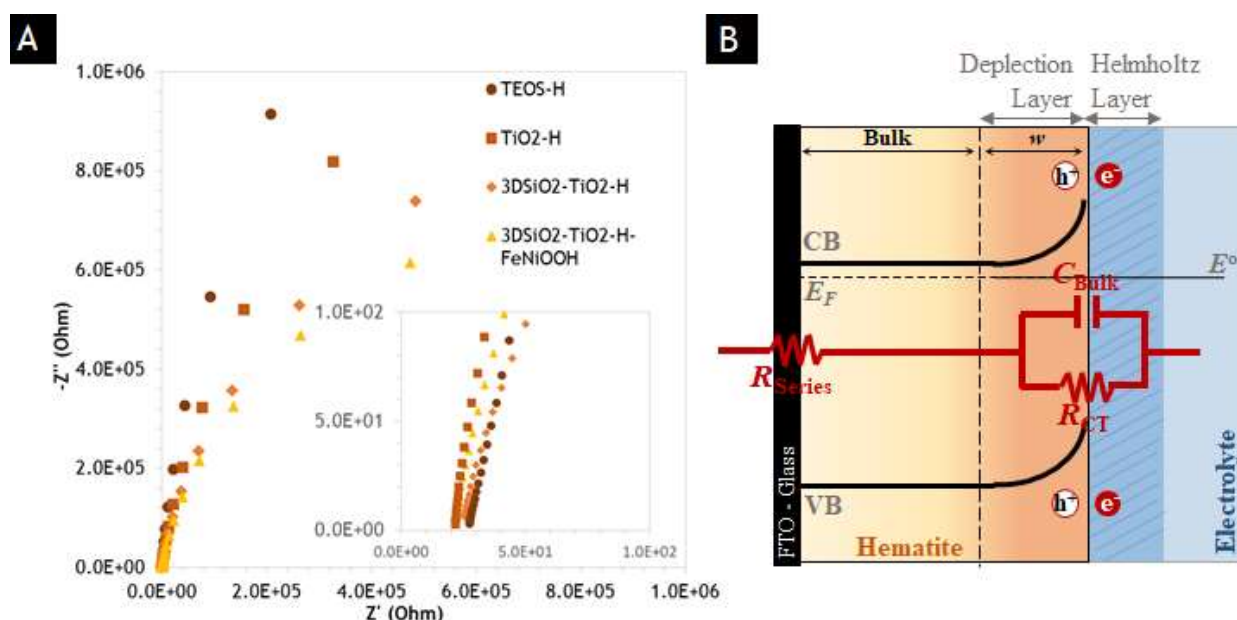


Figure 4-16: A: Nyquist plots obtained in the dark at 1.20 V_{RHE} for the prepared samples; and B: electrical circuit analogue used to fit the impedance data under dark conditions (extracted from [47]).

According to the literature[47, 77], flatband potential, E_{fb} , and donor density, N_D , can be estimated by Mott-Schottky analysis. These parameters can be only fitted in the high-frequency range of impedance spectra, in the order of kHz, by equation 4.1:

$$\frac{1}{C_{Bulk}^2} = \frac{2}{\epsilon_0 \epsilon_r q N_D A^2} \left((E - E_{fb}) - \frac{kT}{q} \right) \quad (4.1)$$

where ϵ_0 is the permittivity of the vacuum ($8.85 \times 10^{-12} \text{ C} \cdot \text{V}^{-1} \cdot \text{m}^{-1}$), ϵ_r is the dielectric constant of the semiconductor (considered 80 for photoanodes of non-doped hematite [78]) elementary charge, A is the active area of the photoelectrode, k is the Boltzmann constant, T

is the absolute temperature and E is the applied potential. Plotting the C_{Bulk}^{-2} as a function of the applied bias potential, it was possible to linearly fit the data between 0.80 and 1.20 V_{RHE} (see Figure 4-17). N_D value was determined from the slope of this line, while E_{fb} value was obtained by extrapolation the intersection of the straight line with the axis of the applied potential.

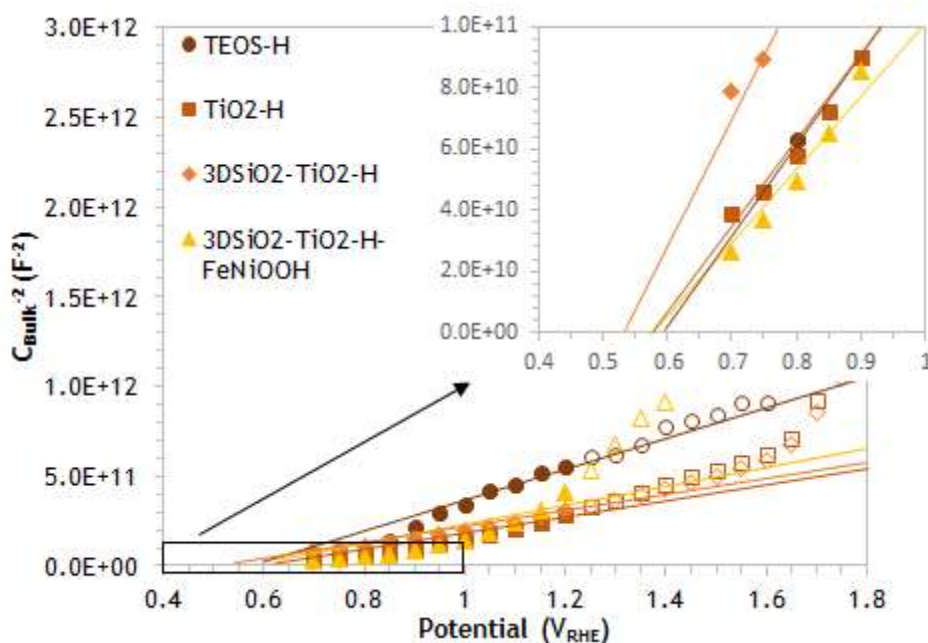


Figure 4-17: Mott-Schottky analysis of the hematite thin film deposited on top of: a TEOS underlayer (TEOS-H, ●), a TiO_2 underlayer (TiO2-H, ■), a nanostructured SiO_2 template and a TiO_2 underlayer (3DSiO2-TiO2-H, ◆), and a nanostructured SiO_2 template and a TiO_2 underlayer and followed by a FeNiOOH co-catalyst coating (3DSiO2-TiO2-H-FeNiOOH, ▲).

The E_{fb} and N_D values obtained for the photoelectrodes tested are shown in Table 4-4. According to the literature, E_{fb} values should range from 0.4 to 0.6 V_{RHE} and N_D in the order of 10^{17} cm^{-3} to 10^{21} cm^{-3} for non-doped and strongly doped hematite samples, respectively.[31] Taking this into account, the results obtained were in line with what was previously anticipated, *i.e.* it was possible to conclude that the TiO_2 underlayer acts as a doping agent, whereas the TEOS underlayer influences in a more significant way to the hematite film growth. In this sense, the TiO_2 underlayer allows an increase in the electrical conductivity, thus justifying the improvement of photoelectrode performance.[75] On the other hand, TEOS reduces the interfacial strain between the FTO and the hematite film, attenuating this effect.[75]

Table 4-4: Flatband potential (E_{fb}) and donor density concentration (N_D) values obtained from Mott-Schottky measurements in the dark for the photoelectrodes under study.

Samples	E_{fb}	N_D
	V_{RHE}	cm^{-3}
TEOS-H	0.59	6.50×10^{18}
TiO ₂ -H	0.56	2.13×10^{19}
3DSiO ₂ -TiO ₂ -H	0.55	1.32×10^{19}
3DSiO ₂ -TiO ₂ -H-FeNiOOH	0.56	2.69×10^{19}

Regarding the tests performed under light conditions at $1.20 V_{RHE}$, the results obtained are presented in the Nyquist curves of Figure 4-18, where two semicircles can be detected. One of them is smaller, in the high frequency range (100 Hz to 1 kHz), which is attributed to the charge transfer process in the bulk of the hematite photoelectrode, generally faster than the transfer processes occurring at the semiconductor/electrolyte interface that corresponds to the low frequencies arc. The low-frequency semicircle is smaller for the sample of 3DSiO₂-TiO₂-H-FeNiOOH, indicating a faster oxidation of surface water. For potentials higher than $1.25 V_{RHE}$ (more positive potentials), the low-frequency semicircle tends to disappear in all samples, indicating that the charge transfer from the surface of α -Fe₂O₃ or FeNiOOH co-catalyst to the electrolyte solution is not the limiting step of water oxidation.[29]

Comparing impedance tests in light and dark, it is verified that the total resistance decreases considerably under illumination conditions, which allows visualizing the interfacial processes, shown in a second semicircle in the Nyquist curves. An equivalent circuit proposed by Klahr *et al.*[29] was considered to fit the impedance data obtained under light conditions. For hematite samples without co-catalyst, the equivalent circuit used was composed of an R_{Series} element, and two RE elements: one for the bulk processes (C_{Bulk} in parallel with a resistance from the charge transport/recombination within the bulk semiconductor, R_{Bulk}) and the other to the surface phenomena, consisting of a charge transfer resistance from the surface states ($R_{CT,SS}$) to electrolyte in parallel with its correspondent capacitance (C_{SS}) - Figure 4-18B. This model allows to study the role of surface states (SS) that act as recombination centers and influence the hole transfer from hematite to electrolyte solution, which is the process mostly contributing to the large potential necessary to oxidize water. In the case of the FeNiOOH co-catalyzed hematite photoelectrode, an additional RC element may be added to represent the FeNiOOH ($R_{CT,cat}$) surface charge transfer resistance and its

capacitance (C_{cat}). This model was not able to fit well the experimental data and a more simple equivalent circuit was used (Figure 4-18C), as reported elsewhere.[47]

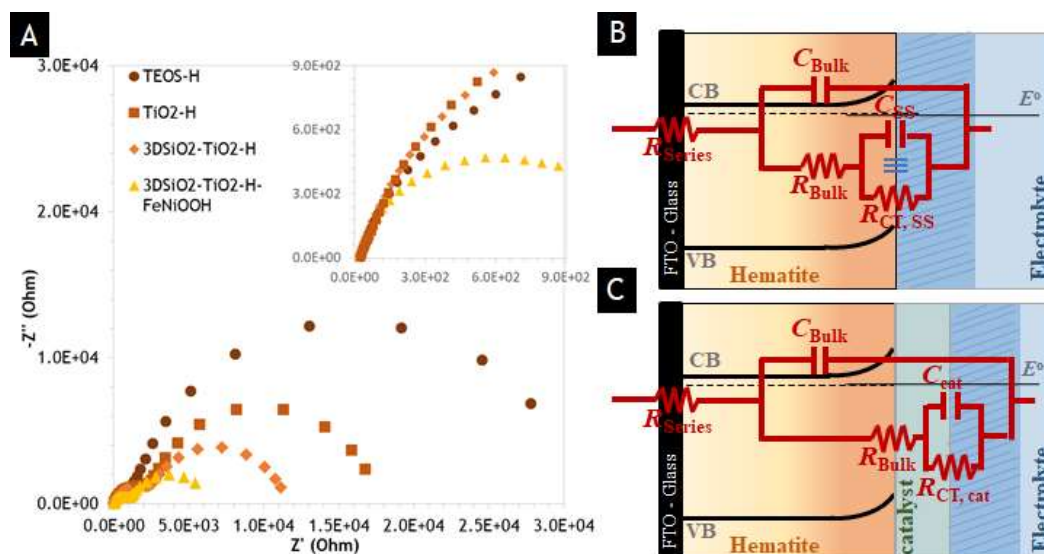


Figure 4-18: A: Nyquist plots obtained in the light at 1.20 V_{RHE} for the prepared samples; B and C: electrical circuit analogue used to fit the impedance data under light conditions (extracted from [47]).

Figure 4-19 shows the behavior of the impedance parameters as a function of the applied potential for hematite (C_{Bulk} , R_{Bulk} , C_{SS} and $R_{CT,SS}$) and hematite coated with FeNiOOH co-catalyst (C_{Bulk} , R_{Bulk} , C_{cat} and $R_{CT,cat}$) photoelectrodes. It was found that the series resistance, R_{Series} , was essentially constant and small for all applied potentials, which includes TCO resistance, resistance related to ionic conductivity in the electrolyte and external contact resistance (e.g. wires).

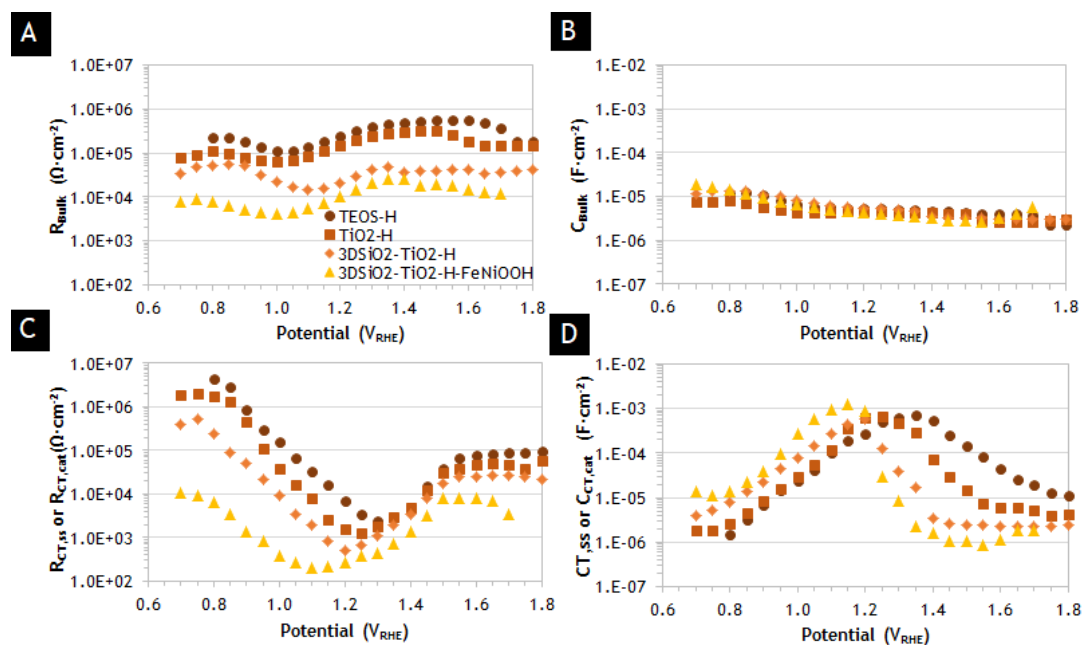


Figure 4-19: Impedance parameters obtained from fitting the EIS data under illumination for the hematite thin film deposited.

Figure 4-19A shows a similar trend for R_{Bulk} for all photoelectrodes. For potentials lower than $1.10 V_{\text{RHE}}$, the R_{Bulk} for the 3DSiO₂-TiO₂-H-FeNiOOH sample shows lower values than for hematite photoelectrodes without a co-catalyst, which suggests that the use of co-catalysts also influences electron-hole recombination in the bulk. On the other hand, for values higher than this potential, the resistance decreases, essentially due to the nanostructured SiO₂ film, since 3DSiO₂-TiO₂-H sample shows a R_{Bulk} one order of magnitude lower. The capacitance, C_{bulk} , is almost constant for the applied potentials, as can be seen in Figure 4-19B.

It is also possible to verify in Figure 4-19C that the charge transfer resistance, R_{CT} , tends to decrease until the photoelectrochemical oxidation potential of water ($1.23 V_{\text{RHE}}$) begins. In contrast, the $R_{\text{CT,cat}}$ value for the 3DSiO₂-TiO₂-H-FeNiOOH sample shows a minimum before $1.10 V_{\text{RHE}}$, which means that the photogenerated holes of hematite can be transferred more efficiently to the co-catalyst layer of FeNiOOH, in which oxidation of water occurs. For more positive potentials, $R_{\text{CT,cat}}$ values start to emerge similar to those of $R_{\text{CT,ss}}$, confirming that the charge transfer from the photoelectrode layer to the electrolyte is not the limiting rate to oxidize water when the applied potential is greater than $1.40 V_{\text{RHE}}$. At these potentials, the photocurrent density is controlled by the number of holes that reach hematite surface.[47] Figure 4-19D shows the behavior of the capacitances of the surface states associated with hematite, C_{ss} , and FeNiOOH co-catalyst, C_{cat} , with the applied potential; both peak near the water oxidation onset potential, which correlate with the observed minimum of $R_{\text{CT,ss}}$ or $R_{\text{CT,cat}}$, respectively. With the increasing filling of surface states, indicated by a peak in C_{ss} , the charge transfer is facilitated by translating in a reduced resistance. In addition, the TEOS-H sample exhibits the lowest C_{ss} values for potentials below $1.25 V_{\text{RHE}}$ and the highest values after this potential; this behavior clearly indicates that the hole transfer occurs predominantly through a surface state in hematite. Therefore, the strategies used in this study (TiO₂ underlayer, SiO₂ nanostructured template and FeNiOOH co-catalyst) prevent the accumulation of positive charge on the hematite surface and decrease the recombination of the trapped electrons with holes from the valence band.

The PEC water oxidation efficiency (η_{OER}) can be determined from the EIS analysis obtained under light conditions using the model proposed by Peter *et al.* [79], which considers the kinetics of water oxidation and the electron-hole recombination of hematite photoanodes.[80] This model suggests a pseudo-first order recombination rate relative to the hole concentration [81, 82] and the rate constant is denoted as k_{rec} . Therefore, as water oxidation proceeds through a sequence of single-hole oxidation steps, the charge transfer rate constant (k_{CT}) is assumed as the first order in the hole density and can be obtained directly at the maximum phase angle of the load transfer semicircle in the Nyquist plots, *i.e.*, the time constant of charge transfer $\tau_{\text{CT}} = R_{\text{CT}} \times C_{\text{ss,cat}}$. [83] In addition, the rate constants k_{CT}

are related to the resistance parameters measured by the EIS (R_{Bulk} and R_{CT}) by the equation 4.2:[84]

$$\frac{R_{Bulk}}{R_{CT}} = \frac{k_{CT}}{(nk_{bulk} + k_{rec})} = \gamma(E) \frac{k_{CT}}{k_{rec}} \quad (4.2)$$

where n is the electron density (taken to be constant at constant illumination intensity), k_{Bulk} is the bulk electron trapping rate constant and $\gamma(E)$ is the probability of electron-trap occupation at a given trap energy and applied potential (E). $\gamma(E)$ is given by the potentials and the trap depth (taking values between 0 and 1): [84]

$$\gamma(E) = \left[1 + \exp\left(\frac{E_F - E_T}{k_B T}\right) \cdot \exp\left(-\frac{qE}{k_B T}\right) \right]^{-1} \quad (4.3)$$

where E_F is the Fermi level at equilibrium and E_T is the energy of the electron trap. At zero potential bias, $\gamma(E)$ depends exclusively on the trap depth in the bandgap. Equation 4.2 can be simplified as $\gamma(E)$ converges to unity as the potential increases:[81]

$$\frac{R_{Bulk}}{R_{CT}} = \frac{k_{CT}}{k_{rec}} \quad (4.4)$$

The water oxidation efficiency (η_{OER}) is thus governed by the balance between k_{CT} and k_{rec} and can be calculated using these parameters:

$$\eta_{OER} = \frac{k_{CT}}{(k_{CT} + k_{rec})} \quad (4.4)$$

Figure 4-20 summarizes the obtained values of k_{CT} , k_{rec} and η_{OER} parameters as a function of the applied potential. The k_{CT} for the TEOS-H sample is in the range of 0.1 - 1 s⁻¹, whereas for the TiO₂-H is in the range of 1 - 10 s⁻¹ at potentials below 1.20 V_{RHE}, which is the typical range for efficient water oxidation, exhibiting lifetimes of holes in the order of 0.1 - 1 s.[33] From Figure 4-20A is also observed a significant k_{CT} increase for the 3DSiO₂-TiO₂-H-FeNiOOH sample mainly at low applied potentials (<1.00 V_{RHE}), showing that FeNiOOH is an efficient co-catalyst also facilitating OER kinetics. For potentials higher than 1.00 V_{RHE} the 3DSiO₂-TiO₂-H sample shows an increased k_{CT} , which may prove that SiO₂ nanostructured scaffold is contributing for an efficient hole transfer.

Electron-hole recombination rate constants, k_{rec} , between 100 and 0.001 s⁻¹ were obtained for the applied potentials under study - Figure 4-20B. At potentials below 1.00 V_{RHE} the k_{rec} values are higher than k_{CT} ; thus the much faster recombination compared to the charge transfer increases the overpotential and, consequently, affects the PEC performance of the hematite photoanodes, as reported elsewhere.[85, 86] Moreover, at these potentials the recombination decreases from TEOS-H>TiO₂-H>3DSiO₂-TiO₂-H>3DSiO₂-TiO₂-H-FeNiOOH, justifying that the use of a TiO₂ underlayer, a nanostructured host scaffold and the addition of a FeNiOOH co-catalyst reduce the surface recombination. The TiO₂ underlayer and the SiO₂

nanostructured template suppress the electron back-injection from FTO to hematite and blocks the hole back into hematite, whereas FeNiOOH can act as a hole storage layer for promoting an efficient oxidation of water to oxygen evolution.

Figure 4-20C plots the water oxidation efficiency as a function of the applied potentials; the shape of these curves is similar to the J - V curves shown in Figure 4-19. 3DSiO₂-TiO₂-H-FeNiOOH photoanode shows greater efficiencies, with values above 50 % and 90 % for potentials higher than 0.80 V_{RHE} and 1.00 V_{RHE}, respectively. The observed improvement is related to the interfacial hole transfer by the nanostructured host scaffold and the suppressed surface recombination by catalysis that results charge separation efficiency and directly influences the PEC performance.

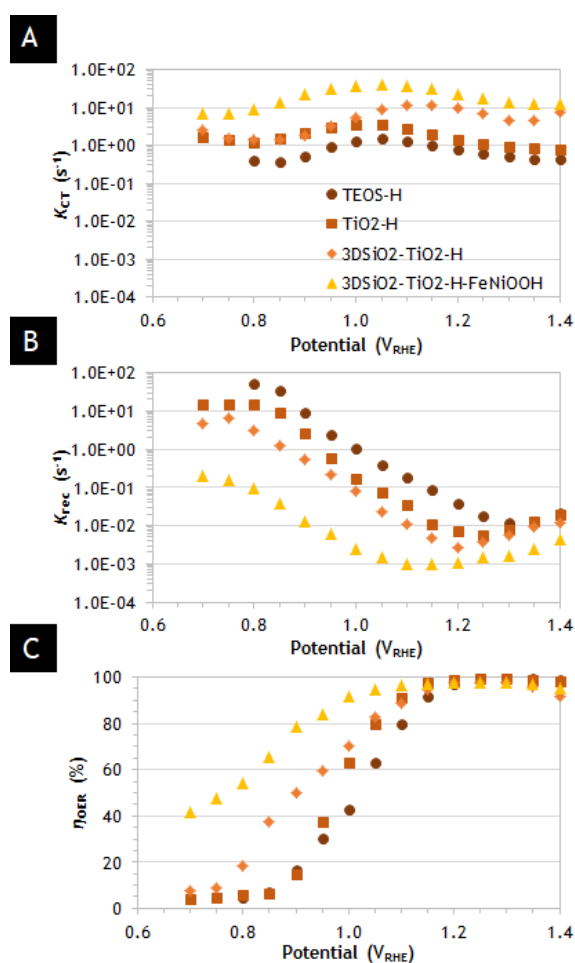


Figure 4-20: A: Charge transfer rate constants, k_{CT} ; B: recombination rate constants, k_{rec} ; and C: water oxidation efficiencies, η_{OER} , for the hematite thin film deposited.

5 Conclusion

The present work aimed at developing an optimized host-guest photoelectrode based on a SiO₂ mesoporous host template coated with a TiO₂ conductive layer and a hematite thin guest film. First, the SiO₂ mesoporous film was optimized, being studied two types of particles with different surface areas (87.8 and 141.6 m²·g⁻¹). The thickness and homogeneity of the prepared film was optimized through controlling the deposition parameters (time and speed) and the dilution of pastes, both evaporated and non-evaporated, with terpineol. In the preliminary tests phase it was possible to verify that as the time and the deposition rate increased, the evolution of the thickness of the mesoporous SiO₂ film followed a slightly decreasing trend. Also, the volume of terpineol was the parameter that most influenced the thicknesses decrease. Based on these observations, various dilutions with terpineol and various deposition times were tested, setting the maximum deposition speed of the equipment (6000 rpm), to optimize both pastes. After optimization, the selected mesoporous film had a thickness of *ca.* 193 nm for the paste with a surface area of 141.6 m²·g⁻¹. Despite greater depths for photons penetration with thicker films (400 - 500 nm) are essentially needed to overcome the hematite characteristic low coefficient of absorption, the lower film thickness was selected due to its uniformity, homogeneity and high surface area.

A TiO₂ thin conductive underlayer was tested and presented a photocurrent density of *ca.* 0.69 mA·cm⁻² at 1.45 V_{RHE}, which corresponds to a performance improvement of *ca.* 23 % compared with a TEOS pre-treatment. This behavior was justified because the TEOS underlayer only influences the hematite film growth, whereas TiO₂ acts as a doping source, facilitating the electric conductivity. For this reason, a conductive thin layer of TiO₂ seems to be a good solution to impregnate the optimized SiO₂ mesoporous template.

The final step consisted in depositing a hematite thin guest layer on top of the SiO₂ nanostructured host layer coated with TiO₂. Two techniques were used for this purpose, ALD and spray pyrolysis. Due to technical problems of the ALD equipment, the deposition of hematite was optimized by spray pyrolysis. The parameter influencing the most the performance of this host-guest approach was the volume of the precursor solution deposited, *i.e.* the thickness of the hematite film. With only 30 mL of precursor solution, a photocurrent density of *ca.* 0.81 mA·cm⁻² at 1.45 V_{RHE} was obtained, which is higher than the one obtained for a hematite thin film on top of a flat FTO glass coated with TiO₂. This result is explained by the existence of a larger deposition surface area which increased the absorption of light and charge transfer. This performance was further enhanced by the deposition of an Earth-abundant co-catalyst, FeNiOOH, that contributes to decrease the overpotential observed in the water oxidation reaction, also reducing the problems of recombination. The onset

potential was shifted to a lower potential of *ca.* 0.70 V_{RHE} and a final photocurrent of *ca.* 0.98 mA·cm⁻² at 1.45 V_{RHE} was obtained, which corresponds to an 85 % current increase compared to hematite thin films deposited onto TEOS pretreated FTO glasses. In fact, the synergy between the SiO₂ mesoporous template, the TiO₂ underlayer and the FeNiOOH co-catalyst improved the charge transfer kinetics and minimized the recombination phenomena in the bulk and surface of hematite, which resulted in an improved water oxidation efficiency.

6 Assessment of the work done

6.1 Objectives Achieved

The three main goals proposed in the present work were achieved: 1) a SiO₂ mesoporous template was deposited and optimized by spin coating, showing an improved surface area and a good homogeneity and thickness; 2) a TiO₂ thin layer was deposited by ALD and demonstrated to be a suitable underlayer for hematite thin films, acting as a Ti dopant and decreasing the back-electron recombination in the bulk; and 3) a hematite thin film was deposited by spray pyrolysis on top of the prepared SiO₂ nanostructured template coated with TiO₂. The optimized photoelectrode based on a SiO₂ nanostructured host layer and a hematite thin guest layer showed a better performance than a similar hematite flat thin film.

6.2 Limitations and Future Work

Although the main objectives of this dissertation have been achieved, there were some limitations during the work, namely the time spent on the preparation of the SiO₂ pastes (which occupied about 60 % of each week). Also, the optimization of mesoporous film deposited by spin coater, with longer deposition times and all the parameters tested, filled a good part of the day within this task. All this made the study of more pastes, *e.g.* with larger specific surface areas, unfeasible. In addition, it should be developed a model that allows to understand how TiO₂ and hematite films were being impregnated in the mesoporous matrix, for finding even better results.

Finally, the major efforts should focus on the deposition of hematite by ALD, which is considered the ideal technique to uniform and conformal films onto high aspect ratio nanostructures. An ALD maintenance by specialized experts is crucial to see if there is any problem that is conditioning the depositions of the hematite film (*e.g.* see if there was any leakage on the ozone line or whether if the precursor of hematite should be changed by virtue of the equipment conditions). If the problem is found and solved, the hematite deposition should be optimized following a design of experiments, which hopefully can culminate in better photoelectrochemical water splitting efficiencies using a host-guest hematite nanostructured photoelectrode.

6.3 Final Assessment

This dissertation gave me the opportunity to work in a very interesting field of research and develop new technological approaches for solar energy storage. During this period, I was able to have direct contact with techniques used in the photoelectrochemical research area,

acquiring a diverse knowledge in this field in such a short time, from deposition techniques that are also used in the industry, such as ALD and spray pyrolysis, to various characterization techniques, *e.g.* SEM/EDS, BET and electrochemical tests.

I truly believe in the future of solar energy and this dissertation gave me the first set of tools to keep pushing research to new frontiers and the motivation that now fuels my will to dedicate myself to this cause.

References

1. Afonso, C., *Energia e Ambiente*. 1 ed. 2008: Faculdade de Engenharia da Universidade do Porto.
2. Lewis, S.L., *The Paris Agreement has solved a troubling problem*. 2016. 532.
3. BP Statistical Review Team, *BP Statistical Review of World Energy June 2017*. 2017.
4. Mead, I., *International Energy Outlook 2017*. 2017, U.S. Energy Information Administration.
5. van de Krol, R. and M. Grätzel, *Photoelectrochemical Hydrogen Production*. Electronic Materials: Science & Technology. 2012.
6. Höök, M. and X. Tang, *Depletion of fossil fuels and anthropogenic climate change—A review*. Energy Policy, 2013. 52: p. 797-809.
7. Burghgraeve Sharon, et al., *CO2 emissions from fuel combustion (Highlights 2017)*. 2017, International Energy Agency. p. 162.
8. Euronews, *Climate Update: February*, in Euronews. 2018: Available online at: <http://www.euronews.com/2018/03/15/climate-update-february>.
9. Hughes, T.P., et al., *Global warming transforms coral reef assemblages*. Nature, 2018. 556(7702): p. 492-496.
10. Core Writing Team; Pachauri, R.K., Meyer, Leo, *Climate Change 2014 (Synthesis Report)*. 2014: Intergovernmental Panel on Climate Change.
11. Agency, I.E. *Renewables 2017*. Publications 2017.
12. Lewis, N.S., Crabtree, G, *Basic Research Needs for Solar Energy Utilization*. 2005, Office of Basic Energy Science: Washington, DC.
13. Riha, S.C., et al., *Atomic Layer Deposition of a Submonolayer Catalyst for the Enhanced Photoelectrochemical Performance of Water Oxidation with Hematite*. ACS Nano, 2013. 7(3): p. 2396-2405.
14. Harriman, A., *Prospects for conversion of solar energy into chemical fuels: the concept of a solar fuels industry*. Philos Trans A Math Phys Eng Sci, 2013. 371(1996): p. 20110415.
15. landolo, B., et al., *The rise of hematite: origin and strategies to reduce the high onset potential for the oxygen evolution reaction*. Journal of Materials Chemistry A, 2015. 3(33): p. 16896-16912.
16. Tuller, H.L., *Solar to fuels conversion technologies: a perspective*. Mater Renew Sustain Energy, 2017. 6(1): p. 3.
17. Rothschild, A. and H. Dotan, *Beating the Efficiency of Photovoltaics-Powered Electrolysis with Tandem Cell Photoelectrolysis*. ACS Energy Letters, 2016. 2(1): p. 45-51.
18. Pinaud, B.A., et al., *Technical and economic feasibility of centralized facilities for solar hydrogen production via photocatalysis and photoelectrochemistry*. Energy & Environmental Science, 2013. 6(7).
19. Shaner, M.R., et al., *A comparative techno-economic analysis of renewable hydrogen production using solar energy*. Energy & Environmental Science, 2016. 9(7): p. 2354-2371.

20. Tamirat, A.G., et al., *Using hematite for photoelectrochemical water splitting: a review of current progress and challenges*. *Nanoscale Horizons*, 2016. 1(4): p. 243-267.
21. Andrade, L., et al., *Transient phenomenological modeling of photoelectrochemical cells for water splitting - Application to undoped hematite electrodes*. *International Journal of Hydrogen Energy*, 2011. 36(1): p. 175-188.
22. Gratzel, M., *Photoelectrochemical cells*. *Nature*, 2001. 414(6861): p. 338-44.
23. van de Krol, R., Y. Liang, and J. Schoonman, *Solar hydrogen production with nanostructured metal oxides*. *Journal of Materials Chemistry*, 2008. 18(20): p. 2311-2320.
24. Ager, J.W., et al., *Experimental demonstrations of spontaneous, solar-driven photoelectrochemical water splitting*. *Energy & Environmental Science*, 2015. 8(10): p. 2811-2824.
25. Formal, F.L., *On the Morphology and Interfaces of Nanostructured Hematite Photoanodes for Solar-Driven Water Splitting*, in *Laboratoire de Photonique et Interfaces*. 2011, École Polytechnique Fédérale de Lausanne.
26. Murphy, A., et al., *Efficiency of solar water splitting using semiconductor electrodes*. *International Journal of Hydrogen Energy*, 2006. 31(14): p. 1999-2017.
27. Sivula, K., F. Le Formal, and M. Graetzel, *Solar Water Splitting: Progress Using Hematite (α -Fe₂O₃) Photoelectrodes*. Vol. 4. 2011. 432-49.
28. Eggleston, C.M., *Geochemistry. Toward new uses for hematite*. *Science*, 2008. 320(5873): p. 184-5.
29. Klahr, B., et al., *Water oxidation at hematite photoelectrodes: the role of surface states*. *J Am Chem Soc*, 2012. 134(9): p. 4294-302.
30. Young, K.M.H., et al., *Photocatalytic water oxidation with hematite electrodes*. *Catalysis Science & Technology*, 2013. 3(7).
31. Dias, P., et al., *Extremely stable bare hematite photoanode for solar water splitting*. *Nano Energy*, 2016. 23: p. 70-79.
32. Brillet, J., et al., *Highly efficient water splitting by a dual-absorber tandem cell*. *Nature Photonics*, 2012. 6(12): p. 824-828.
33. Le Formal, F., et al., *Back electron-hole recombination in hematite photoanodes for water splitting*. *J Am Chem Soc*, 2014. 136(6): p. 2564-74.
34. Pendlebury, S.R., et al., *Ultrafast charge carrier recombination and trapping in hematite photoanodes under applied bias*. *J Am Chem Soc*, 2014. 136(28): p. 9854-7.
35. Mayer, M.T., C. Du, and D. Wang, *Hematite/Si nanowire dual-absorber system for photoelectrochemical water splitting at low applied potentials*. *J Am Chem Soc*, 2012. 134(30): p. 12406-9.
36. Wang, K.X., et al., *Nearly Total Solar Absorption in Ultrathin Nanostructured Iron Oxide for Efficient Photoelectrochemical Water Splitting*. *ACS Photonics*, 2014. 1(3): p. 235-240.
37. Kim do, H., et al., *Toward High-Performance Hematite Nanotube Photoanodes: Charge-Transfer Engineering at Heterointerfaces*. *ACS Appl Mater Interfaces*, 2016. 8(36): p. 23793-800.
38. Zeng, S., et al., *Facile Route for the Fabrication of Porous Hematite Nanoflowers: Its Synthesis, Growth Mechanism, Application in the Lithium Ion Battery, and Magnetic and Photocatalytic Properties*. *The Journal of Physical Chemistry C*, 2008. 112(13): p. 4836-4843.

39. Bora, D.K., *Fabrication of silicon doped hematite photoelectrode with enhanced photocurrent density via solution processing of an in-situ TEOS modified precursor*. *Materials Science in Semiconductor Processing*, 2015. **31**: p. 728-738.
40. Lee, M.H., et al., *Nanostructured Ti-doped hematite (α -Fe₂O₃) photoanodes for efficient photoelectrochemical water oxidation*. *International Journal of Hydrogen Energy*, 2014. **39**(30): p. 17501-17507.
41. Li, M., et al., *Morphology and Doping Engineering of Sn-Doped Hematite Nanowire Photoanodes*. *Nano Lett*, 2017. **17**(4): p. 2490-2495.
42. Neufeld, O. and M.C. Toroker, *Platinum-Doped α -Fe₂O₃ for Enhanced Water Splitting Efficiency: A DFT+U Study*. *The Journal of Physical Chemistry C*, 2015. **119**(11): p. 5836-5847.
43. Qi, X., et al., *Electrochemical synthesis of p-type Zn-doped α -Fe₂O₃ nanotube arrays for photoelectrochemical water splitting*. *Chem Commun (Camb)*, 2013. **49**(51): p. 5742-4.
44. Zhong, D.K. and D.R. Gamelin, *Photoelectrochemical water oxidation by cobalt catalyst ("Co-Pi")/ α -Fe₂O₃ composite photoanodes: oxygen evolution and resolution of a kinetic bottleneck*. *J Am Chem Soc*, 2010. **132**(12): p. 4202-7.
45. Yen, C.-P., et al., *Characteristics of NixFe_{1-x}Oy Electrocatalyst on Hematite as Photoanode for Solar Hydrogen Production*. *Catalysts*, 2017. **7**(11).
46. Wang, Z., et al., *Synergetic Effect of Conjugated Ni(OH)₂/IrO₂ Cocatalyst on Titanium-Doped Hematite Photoanode for Solar Water Splitting*. *The Journal of Physical Chemistry C*, 2015. **119**(34): p. 19607-19612.
47. Dias, P., L. Andrade, and A. Mendes, *Hematite-based photoelectrode for solar water splitting with very high photovoltage*. *Nano Energy*, 2017. **38**: p. 218-231.
48. Yoon, K.-Y., et al., *A selectively decorated Ti-FeOOH co-catalyst for a highly efficient porous hematite-based water splitting system*. *Journal of Materials Chemistry A*, 2016. **4**(48): p. 18730-18736.
49. Jia, L., et al., *Sputtering Deposition of Ultra-thin α -Fe₂O₃ Films for Solar Water Splitting*. *Journal of Materials Science & Technology*, 2015. **31**(6): p. 655-659.
50. Kay, A., et al., *Heterogeneous Doping to Improve the Performance of Thin-Film Hematite Photoanodes for Solar Water Splitting*. *ACS Energy Letters*, 2016. **1**(4): p. 827-833.
51. Zandi, O. and T.W. Hamann, *Enhanced Water Splitting Efficiency Through Selective Surface State Removal*. *J Phys Chem Lett*, 2014. **5**(9): p. 1522-6.
52. Zandi, O., et al., *Enhanced Charge Separation and Collection in High-Performance Electrodeposited Hematite Films*. *Chemistry of Materials*, 2016. **28**(3): p. 765-771.
53. Duret, A. and M. Gratzel, *Visible light-induced water oxidation on mesoscopic α -Fe₂O₃ films made by ultrasonic spray pyrolysis*. *J Phys Chem B*, 2005. **109**(36): p. 17184-91.
54. Tilley, S.D., et al., *Light-induced water splitting with hematite: improved nanostructure and iridium oxide catalysis*. *Angew Chem Int Ed Engl*, 2010. **49**(36): p. 6405-8.
55. Jeon, T.H., et al., *Ultra-efficient and durable photoelectrochemical water oxidation using elaborately designed hematite nanorod arrays*. *Nano Energy*, 2017. **39**: p. 211-218.

56. Steier, L., et al., *Low-Temperature Atomic Layer Deposition of Crystalline and Photoactive Ultrathin Hematite Films for Solar Water Splitting*. ACS Nano, 2015. **9**(12): p. 11775-83.
57. Li, J., et al., *A three-dimensional hexagonal fluorine-doped tin oxide nanocone array: a superior light harvesting electrode for high performance photoelectrochemical water splitting*. Energy Environ. Sci., 2014. **7**(11): p. 3651-3658.
58. Souza, F.L., et al., *The influence of the film thickness of nanostructured alpha-Fe₂O₃ on water photooxidation*. Phys Chem Chem Phys, 2009. **11**(8): p. 1215-9.
59. Yu, Q., et al., *Hematite Films Decorated with Nanostructured Ferric Oxyhydroxide as Photoanodes for Efficient and Stable Photoelectrochemical Water Splitting*. Advanced Functional Materials, 2015. **25**(18): p. 2686-2692.
60. Kim, J.Y., et al., *Single-crystalline, wormlike hematite photoanodes for efficient solar water splitting*. Sci Rep, 2013. **3**: p. 2681.
61. Le Formal, F., et al., *Passivating surface states on water splitting hematite photoanodes with alumina overlayers*. Chem. Sci., 2011. **2**(4): p. 737-743.
62. Wang, G., et al., *Facile synthesis of highly photoactive alpha-Fe₂O₃-based films for water oxidation*. Nano Lett, 2011. **11**(8): p. 3503-9.
63. Vincent, T., et al., *Thermally oxidized iron oxide nanoarchitectures for hydrogen production by solar-induced water splitting*. International Journal of Hydrogen Energy, 2012. **37**(9): p. 8102-8109.
64. Li, L., et al., *Facile solution synthesis of alpha-FeF₃.3H₂O nanowires and their conversion to alpha-Fe₂O₃ nanowires for photoelectrochemical application*. Nano Lett, 2012. **12**(2): p. 724-31.
65. N, P. and K. M., *Atomic Layer Deposition of Nanostructured Materials*, K. Wiley-VCH Verlag&Co, Editor. 2012: Germany.
66. Steier, L., *Fabrication and Characterization of Functional ALD Metal Oxide Thin Films for Solar Applications*, in *Laboratoire de Photonique et Interfaces*. 2016, École Polytechnique Fédérale de Lausanne: Faculté Des Sciences De Base.
67. Ito, S., et al., *Fabrication of screen-printing pastes from TiO₂ powders for dye-sensitised solar cells*. Progress in Photovoltaics: Research and Applications, 2007. **15**(7): p. 603-612.
68. Ritala, M. and M. Leskelä, *Atomic layer deposition*, in *Handbook of Thin Films*. 2002. p. 103-159.
69. Leskelä, M. and M. Ritala, *Atomic layer deposition (ALD): from precursors to thin film structures*. Thin Solid Films, 2002. **409**(1): p. 138-146.
70. Perednis, D. and L.J. Gauckler, *Thin Film Deposition Using Spray Pyrolysis*. Journal of Electroceramics, 2005. **14**(2): p. 103-111.
71. Tsyganok, A., et al., *Different Roles of Fe_{1-x}Ni_xOOH Cocatalyst on Hematite (alpha-Fe₂O₃) Photoanodes with Different Dopants*. ACS Catalysis, 2018: p. 2754-2759.
72. Martinson, A.B.F., et al., *Atomic Layer Deposition of Fe₂O₃ Using Ferrocene and Ozone*. The Journal of Physical Chemistry C, 2011. **115**(10): p. 4333-4339.
73. Li, X., N.C. Fan, and H.J. Fan, *A Micro-pulse Process of Atomic Layer Deposition of Iron Oxide Using Ferrocene and Ozone Precursors and Ti-Doping*. Chemical Vapor Deposition, 2013. **19**(4-6): p. 104-110.
74. Yuan, Q., et al., *Mechanical and thermal properties of high-density polyethylene toughened with glass beads*. Journal of Applied Polymer Science, 2003. **89**(8): p. 2102-2107.

75. Wang, J., et al., *Enhanced Bulk and Interfacial Charge Transfer Dynamics for Efficient Photoelectrochemical Water Splitting: The Case of Hematite Nanorod Arrays*. ACS Appl Mater Interfaces, 2016. **8**(35): p. 23143-50.
76. Tsyganok, A., et al., *Different Roles of Fe_{1-x}Ni_xOOH Cocatalyst on Hematite (α -Fe₂O₃) Photoanodes with Different Dopants*. ACS Catalysis, 2018. **8**(4): p. 2754-2759.
77. Lopes, T., et al., *Hematite photoelectrodes for water splitting: evaluation of the role of film thickness by impedance spectroscopy*. Phys Chem Chem Phys, 2014. **16**(31): p. 16515-23.
78. Cesar, I., et al., *Influence of Feature Size, Film Thickness, and Silicon Doping on the Performance of Nanostructured Hematite Photoanodes for Solar Water Splitting*. The Journal of Physical Chemistry C, 2008. **113**(2): p. 772-782.
79. Upul Wijayantha, K.G., S. Saremi-Yarahmadi, and L.M. Peter, *Kinetics of oxygen evolution at α -Fe₂O₃ photoanodes: a study by photoelectrochemical impedance spectroscopy*. Phys Chem Chem Phys, 2011. **13**(12): p. 5264-70.
80. Thorne, J.E., et al., *Understanding the origin of photoelectrode performance enhancement by probing surface kinetics*. Chemical Science, 2016. **7**(5): p. 3347-3354.
81. Li, W., et al., *Comparison of heterogenized molecular and heterogeneous oxide catalysts for photoelectrochemical water oxidation*. Energy & Environmental Science, 2016. **9**(5): p. 1794-1802.
82. Pendlebury, S.R., et al., *Correlating long-lived photogenerated hole populations with photocurrent densities in hematite water oxidation photoanodes*. Energy Environ. Sci., 2012. **5**(4): p. 6304-6312.
83. Carroll, G.M., D.K. Zhong, and D.R. Gamelin, *Mechanistic insights into solar water oxidation by cobalt-phosphate-modified α -Fe₂O₃ photoanodes*. Energy & Environmental Science, 2015. **8**(2): p. 577-584.
84. Bertoluzzi, L. and J. Bisquert, *Equivalent Circuit of Electrons and Holes in Thin Semiconductor Films for Photoelectrochemical Water Splitting Applications*. J Phys Chem Lett, 2012. **3**(17): p. 2517-22.
85. Klahr, B., et al., *Photoelectrochemical and impedance spectroscopic investigation of water oxidation with "Co-Pi"-coated hematite electrodes*. J Am Chem Soc, 2012. **134**(40): p. 16693-700.
86. Le Formal, F., K. Sivula, and M. Grätzel, *The Transient Photocurrent and Photovoltage Behavior of a Hematite Photoanode under Working Conditions and the Influence of Surface Treatments*. The Journal of Physical Chemistry C, 2012. **116**(51): p. 26707-26720.

Appendix A - Brunauer-Emmet-Teller (BET) method (basic principles of A_s (BET) calculation)

Adsorption is a process characterized by the accumulation of atoms, molecules or ions at an interface. The adsorption may be physical (physisorption) or chemical (chemisorption). Physisorption is a phenomenon characterized by the establishment of weak intermolecular bonds between the adsorbate and the adsorbent. It is a phenomenon that occurs whenever the surface of a gas contacts that of a solid.[A1] The Brunauer-Emmett-Teller (BET) method is based on a process of physisorption between an adsorbate (usually nitrogen is the most used) and the adsorbent (material subject to measurement of specific surface area). Physisorption is initiated with a monolayer adsorption, in which all the adsorbed molecules are in contact with the surface layer of the adsorbent, and thereafter in a multilayer adsorption, in which the adsorption space accommodates more than one layer of molecules. The BET process takes place in two stages: one of physical adsorption and the other of desorption. At the end, it is possible to collect data that allows obtaining the isothermal curves (see Figure A-1). These curves represent the volume of gas adsorbed as a function of the partial pressure of nitrogen injected into the sample, p/p_0 . The system makes successive measurements until p approaches the reference pressure, p_0 . From there, the desorption process begins to take place.

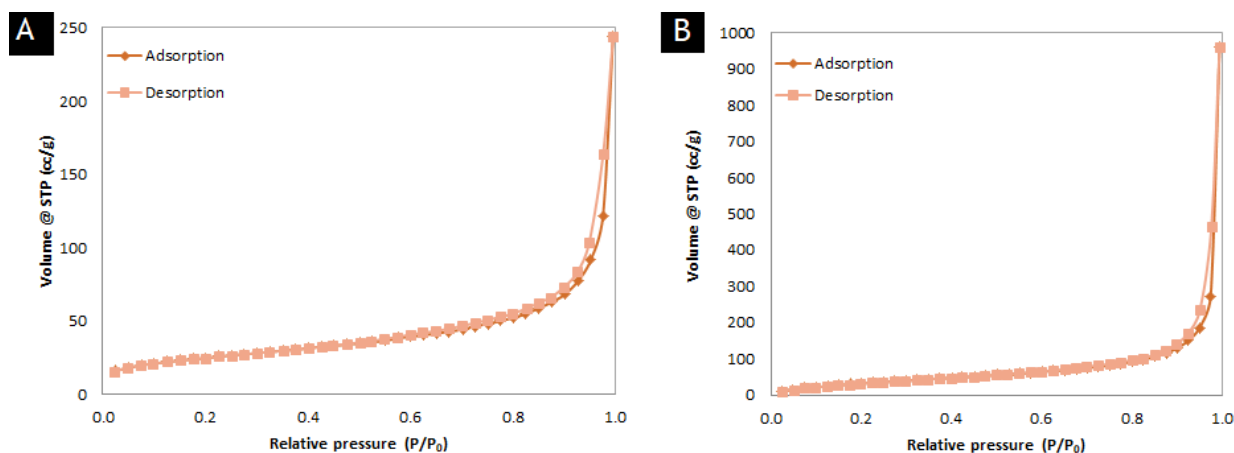


Figure A-1: Physisorption curves (A: particles A; B: particles B).

To determine the surface area, the physisorption isotherm must be linearized and transformed into a BET plot, from which the BET monolayer capacity value, n_m . In a second phase, the BET area, A_s (BET), is calculated from n_m by adopting an appropriate value of the molecular cross-sectional area, σ . To construct the BET graph, it is customary to apply the BET equation in the linear form, according to equation A.1:[A1]

$$\frac{p/p^0}{n_{N_2,abs}(1-p/p^0)} = \frac{1}{n_m C} + \frac{C-1}{n_m C} (p/p^0) \quad (\text{A.1})$$

where $n_{N_2,abs}$ is the specific amount adsorbed at the relative pressure p/p^0 , n_m is the specific capacity of the monolayer and the parameter C is related to the monolayer adsorption energy, which provides a useful indication of the shape of the isotherm in the BET range. In the case of mesoporous particles such as those used, this value is usually between 100 and 200. The parameter n_m can be determined by the BET graph, *i.e.* $(p/p^0)/n_{N_2,abs}(1-p/p^0)$ in function of p/p^0 , from which it is possible to determine the slope of the adjustment line and the ordinate at the origin. With the constant C given by the apparatus, it is possible to determine n_m . Therefore, the determination of the specific surface area of the sample is given by equation A.2:

$$A_S(\text{BET}) = \frac{n_m \times L \times \sigma_m}{m} \quad (\text{A.2})$$

where $A_S(\text{BET})$ is the BET specific area of the adsorbent (of mass m), L is Avogadro's number and σ_m molecular cross-sectional area), occupied by the adsorbate molecule in the complete monolayer.

A1. Thommes, M., et al., *Physisorption of gases, with special reference to the evaluation of surface area and pore size distribution (IUPAC Technical Report)*. Pure and Applied Chemistry, 2015. **87**(9-10)

Appendix B - Atomic Layer Deposition operation

As previously mentioned, the ALD depositions were made using a Beneq TFS 200 system. The system consists of two steel containers (one for each precursor), a reaction chamber and a vacuum chamber, with its respective vacuum pump (Alcatel Adixen 2033C2), a system of circulation of the carrier gas and steel heat exchangers. The carrier gas used is nitrogen and circulates in two lines. Depositions occur with nitrogen at a constant flow rate, which is adjusted either by the vacuum chamber mass flow controller (MFC-Chamber) or by the reactor mass flow controller (MFC-Reactor). It is through these two controllers that the chamber and reactor pressures are determined and controlled. MFC-Reactor has the function of defining the nitrogen flow and the pressures in the precursors containers. In a deposition, the pressure in the chamber must always be greater than in the reactor, in order to avoid leakage of the precursors into the chamber. The reactor is connected to the vacuum pump. This connection is monitored by two pneumatic valves: DV-P1 (used for large flow rates) and DV-P2 (used for flow control). The precursors are temperature controlled and each has their feed line, which arises after the MFC-Reactor. The power lines have controlled flow through pneumatic valves and are each connected to the reactor.

Whenever a deposition occurs, the pulsating pneumatic valves (DV-PH1 if it is the first precursor or DV-PL1 if it is the second precursor) are opened and the precursor is pulsed into the reactor. At this stage, the precursors must have a vapor pressure greater than the working pressure in the reactor in order to flow there. When this does not happen, carrier gas is used and the pneumatic valves DV-BHA1 and DV-BH1 (if the first precursor) or DV-BL1 (if it is the second precursor) are activated. Then, the precursor is pulsed and the valve DV-PL1 (if it is the first precursor) or DV-PH1 (if it is the second precursor) is activated. Figure A-1 shows the operating scheme of the ALD installation.

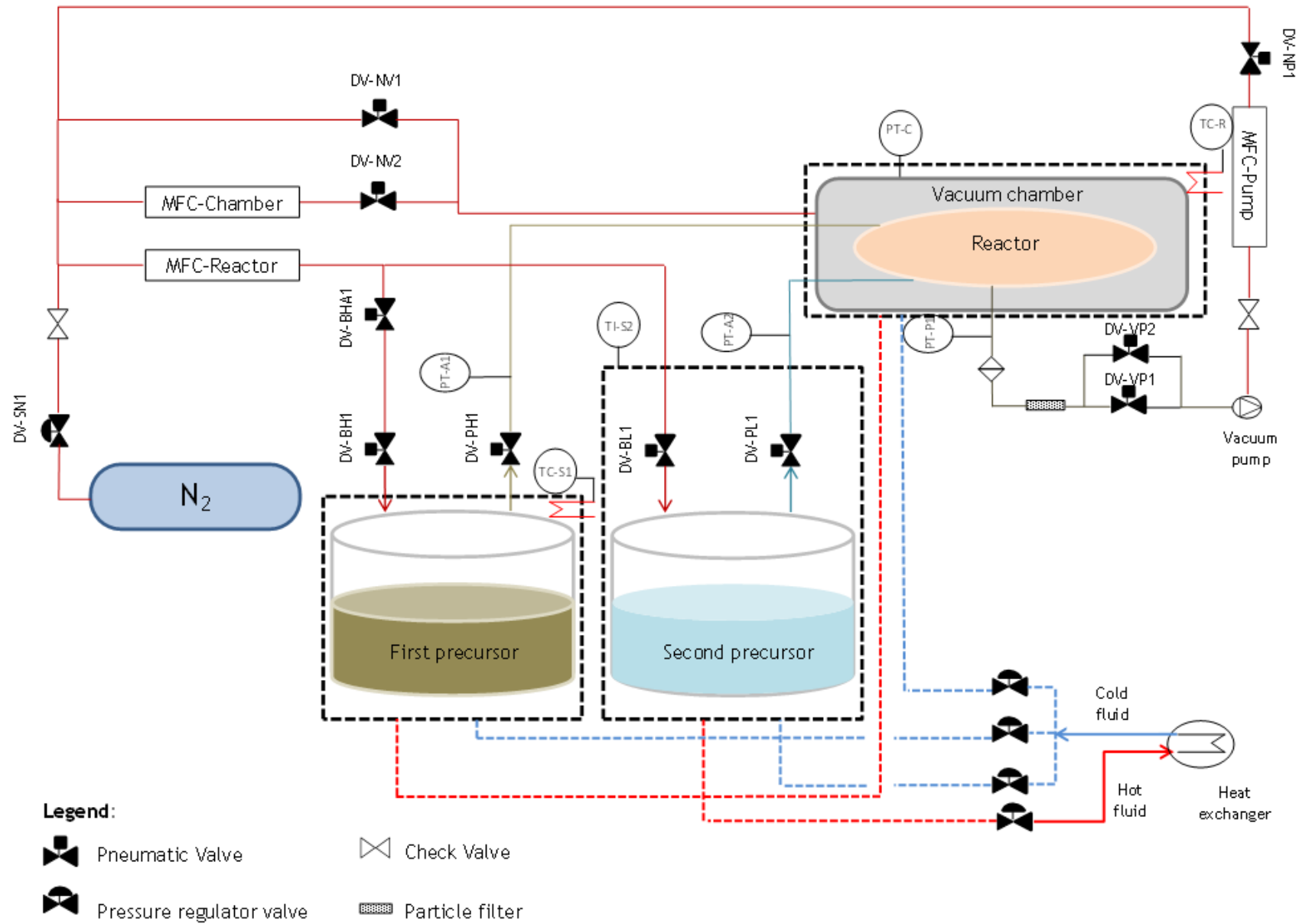


Figure B-1: ALD installation and operation (schematic picture).

To better understand the scheme presented, it is important to clarify the meaning of some acronyms presented. Table B-1 gives a descriptive presentation of each one.

Table B-1: Acronym devices description from ALD scheme.

Acronym	Description
DV-SN1	N ₂ inlet main valve
DV-NP1	Vacuum pump gas ballast valve
DV-NV1	Vacuum chamber flow valve for process
DV-NV2	Vacuum chamber fast flow valve for venting
DV-BH1	Bubbler valve for hot source 1 (first precursor)
DV-BHA1	Carrier/purge gas valve for hot source 1 (first precursor)
DV-PL1	Pulsing valve for liquid source
DV-BL1	Bubbler tube valve for liquid source
DV-PH1	Pulsing valve for hot source (first precursor)
DV-VP1	Vacuum pump main valve
DV-VP2	Vacuum pump soft start valve
PT-A1	Pressure transducer for hot source N ₂ tube monitoring
PT-A2	Pressure transducer for liquid source feeding tube monitoring
PT-C	Pressure transducer for vacuum chamber intermediate volume monitoring
PT-P1	Pressure transducer for pump line (reactor) pressure monitoring
TC-S1	Sensor for hot source 1 (first precursor) container temperature control and monitoring
TC-R	Sensor for reaction chamber temperature control and monitoring
TI-S2	Sensor for liquid source 2 (second precursor) container temperature control

B.1 TiO₂ deposition (operating conditions)

Table B-2 presents the ALD operating conditions for TiO₂ deposition over the glass substrates.

Table B-2: ALD process conditions for TiO₂ deposition.

Process compartment	Description	Value
Vacuum chamber/Reactor	Temperature	225 °C
	Chamber pressure	7 mbar
	Reactor Pressure	4.5 mbar
	Chamber flowrate	250 cm ³ ·s ⁻¹
	Reactor flowrate	300 cm ³ ·s ⁻¹
TIP (first precursor)	Temperature	50 °C
	Pulse time	33 s
	Purge time	4 min
Distilled water (second precursor)	Temperature	20 °C
	Pulse time	22 s
	Purge time	2 min

Usually, each deposition takes about 21 h, in which 2 h correspond to the heating time of the reactor plate and the remaining 19 h to the deposition process itself.

B.2 Hematite deposition (operating conditions)

Hematite depositions by ALD were done in several steps, in which pulse times and temperatures were varied. Each deposition was composed of 500 cycles. Table A-3 shows the various tests that were performed.

Table B-3: ALD process conditions for hematite deposition.

Process compartment	Description	First test values	Second test values	Third test values	Fourth test values
Vacuum chamber/Reactor	Temperature	250 °C	250 °C	250 °C	250 °C
	Chamber pressure	7 mbar	7 mbar	7 mbar	7 mbar
	Reactor Pressure	4.5 mbar	4.5 mbar	4.5 mbar	4.5 mbar
	Chamber flowrate	250 $\text{cm}^3 \cdot \text{s}^{-1}$	250 $\text{cm}^3 \cdot \text{s}^{-1}$	250 $\text{cm}^3 \cdot \text{s}^{-1}$	250 $\text{cm}^3 \cdot \text{s}^{-1}$
	Reactor flowrate	600 $\text{cm}^3 \cdot \text{s}^{-1}$	600 $\text{cm}^3 \cdot \text{s}^{-1}$	600 $\text{cm}^3 \cdot \text{s}^{-1}$	600 $\text{cm}^3 \cdot \text{s}^{-1}$
Ferrocene (first precursor)	Temperature	100 °C	100 °C	120 °C	100 °C
	Pulse time	1.5 s	5 s	0.5 (micropulse)	3 s
	Purge time	7 s	7 s	7 s	7 s
Ozone (second precursor)	Pulse time	2 s	5 s	2 s	4 s
	Purge time	7 s	7 s	7 s	7 s

Appendix C - Hematite film thickness calculation

Thickness measurements of the hematite films were achieved by measuring the reflectance and transmittance of the samples on a UV-Vis absorption spectrophotometer. The concepts of absorbance, reflectance and transmittance are related to each other. In order to clarify its meaning, suppose a beam of light passes through a sample, as shown in Figure C-1.

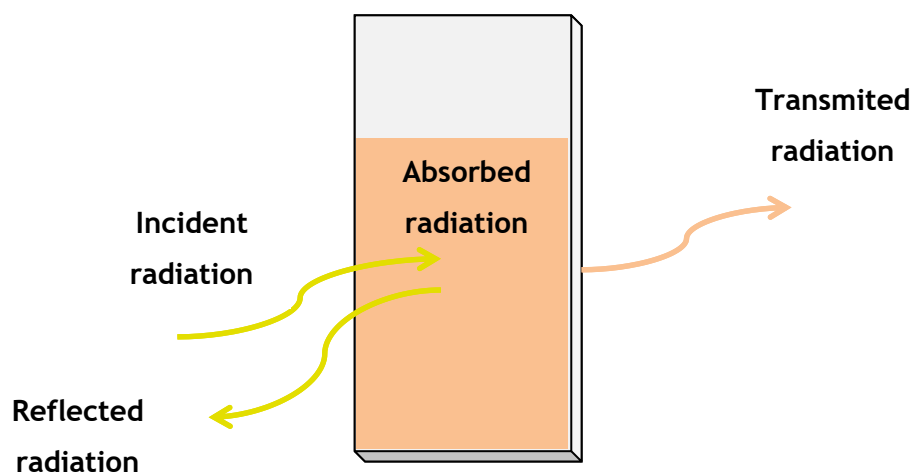


Figure C-1: Behavior of radiation incident on a hematite photoelectrode.

The radiation from the light beam that is able to pass through the sample is called transmittance. And the radiation that reaches the sample but is reflected corresponds to its reflectance. In this case, it is easy to conclude that the radiation that is absorbed corresponds to the absorbance of the sample. The thickness of a hematite film is related to the absorbance by the following equation:[C1]

$$l = \frac{\ln(1 - Abs(sample))}{-\alpha} \quad (C.1)$$

where l is the film thickness, A is the absorbance and α is the absorption coefficient of hematite (44 nm^{-1}). The absorbance of the sample is determined by the equation C.2:

$$Abs(sample)(\%) = 100 - reflectance(\%) - transmittance(\%) \quad (C.2)$$

Since the template is not fully transparent, it is necessary to correct the absorbance values as follows:

$$Abs(sample\ corrected)(\%) = Abs(sample)(\%) - Abs(glass\ substrate)(\%) \quad (C.3)$$

The transmittance and reflectance data collection was done by the equipment in a range of wavelengths between 300 and 700 nm. However, hematite is a material that presents an absorption peak around 400 nm of the visible spectrum. In order to apply

equation C.1, the absorbance value of the sample, calculated by equation C.3, at 400 nm, was used to obtain all the data for calculating the hematite film thickness.

C1. Vilanova, A.M.N., *Preparation and optimization of hematite photoanodes for hydrogen production from photoelectrochemical cells*, in *Chemical Engineering Department*. 2014, University of Porto: Porto.